INSTITUT FÜR WASSERCHEMIE UND CHEMISCHE BALNEOLOGIE
LEHRSTUHL FÜR ANALYTISCHE CHEMIE
DER
TECHNISCHEN UNIVERSITÄT MÜNCHEN

Characterization of a combined optoacoustic / ultrasound system (OPUS) for tomographic absorption measurements

Dipl.-Phys. Univ. Karin Eilert-Zell

Vollständiger Abdruck der von der Fakultät für Chemie der Technischen Universität München zur Erlangung des akademischen Grades eines

Doktors der Naturwissenschaften (Dr. rer. nat.)

genehmigten Dissertation.

Vorsitzender:		Univ.-Prof. Dr. M. Schuster
Prüfer der Dissertation:	1.	Univ.-Prof. Dr. R. Nießner
	2.	Univ.-Prof. V. Ntziachristos, Ph.D.

Die Dissertation wurde am 16.08.2012 bei der Technischen Universität München eingereicht und durch die Fakultät für Chemie am 26.11.2012 angenommen.

Essential components of the presented dissertation have already been published in scientific journals and conference proceedings:

C. Haisch, K. Zell, J.I. Sperl, S. Ketzer, M.W. Vogel, P. Menzenbach, R. Niessner, *OPUS - Optoacoustic imaging combined with conventional ultrasound for breast cancer detection*, 2007, SPIE Proceedings, ECBO Munich, Vol 6631

J.I. Sperl, K. Zell, P. Menzenbach, C. Haisch, S. Ketzer, M. Marquart, H. Koenig, and M.W. Vogel, *Photoacoustic Image Reconstruction - A Quantitative Analysis*, 2007, SPIE Proceedings, ECBO Munich, Vol 6631

K. Zell, J.I. Sperl, M.W. Vogel, R. Niessner, C. Haisch, *Acoustical properties of selected tissue phantom materials for ultrasound imaging*, Physics in Medicine and Biology (2007), 52(20), N475-84.

K .Zell, M.W. Vogel, P. Menzenbach, R. Niessner, C. Haisch, *First practical results with the optoacoustic/ultrasound system OPUS*, 2008, SPIE Proceedings, BiOS, Vol 6856

C. Haisch, K. Eilert-Zell, M. Vogel, P. Menzenbach and R. Niessner, *Combined optoacoustic/ultrasound system for tomographic absorption measurements: possibilities and limitations*, Analytical Bioanalytical Chemistry, 397:1503-1510, 2010

Acknowledgments

My greatful thanks to my supervisor Prof. Dr. Reinhard Niessner who gave me the chance to work on this interesting subject and waited patiently for my final writings.

Spacial thanks to my tutor Prof. Dr. Christoph Haisch for the long discussions and the help in all phases of this dissertation research.

Sincere thanks are given to all who contributed to the success of this work:
Dr. Wolfgang Bayer, Julia Blechinger, Victor Bretzler, Guido Göritz,
Dr. Clemens Helmbrecht, Isabella Kallisch, Stephan Ketzer,
Dr. Carsten Kykal, Dr. Fritz Ley, Robert Mayer, Peter Menzenbach,
Claudia Meyer-Pundsack, Christian Schiller, Jonathan Sperl,
Dr. Herbert Stepp, Dr. Mika Vogel, and Sebastian Wiesemann.

Thanks to my colleges for the great time. To my friends many thanks for pushing me forward and being there.

To my husband John-Christian Eilert a heartfelt thank for the long discussions, his patients and his great support. My thanks to my parents who supported me all the years and to my son for his patients and his happiness.

The financial support of the Bayerische Staatsministerium für Wirtschaft, Verkehr und Technologie within the framework of the BayMed program and of the Max-Buchner-Forschungsstiftung (grant ID 2709) is gratefully acknowledged.

Abstract

In this work, the OPUS (Optocoustic Plus UltraSound) system, a combination of a wavelength-tunable pulsed optical parametrical oscillator (OPO) laser system and a commercial ultrasound (US) scanner, is presented. The system has been designed as an add-on to the commercial ultrasound system to enable breast cancer detection using the benefits of both imaging modalities simultaneously. Optoacoustic (OA) or, synonymously, photoacoustic (PA) is a spectroscopical technique to explore optical absorption in semitransparent solids and liquids. Absorbed energy of laser radiation is converted into acoustic pressure waves. Spatially and temporally detected measurements of the pressure wave at the sample surface allow imaging of 2D or even 3D distribution of the optical absorption. The OPUS system is provided for medical application in particular for breast imaging. One focus lies on quantitative analysis determining blood oxygen saturation. The performance of the OPUS system has been investigated in phantom studies. The development and characterization of the phantoms and absorber materials are part of the presented work as well.

Zusammenfassung

In dieser Arbeit wird das OPUS (Optoacoustic Plus UltraSound)-System präsentiert, das aus einer Kombination eines Wellenlängen-abstimmbaren optischen parametrischen Oszillator (OPO)-Lasersystems und eines kommerziellen Ultraschallscanners besteht. Das System wurde als Add-on zu einem kommerziellen Ultraschallgerät (US) entwickelt, um die Vorteile beider bildgebenden Verfahren gleichzeitig, etwa für Brustkrebsuntersuchung, nutzen zu können. Optoakustik (OA), auch Photoakustik (PA) genannt, ist eine spektroskopische Methode zur Untersuchung von optischen Absorptionen in halbtransparenten Festkörpern und Flüssigkeiten. Die absorbierte Laserstrahlung wird in eine akustische Druckwelle umgewandelt. Räumlich und zeitlich aufgelöste Messungen der Druckwelle an der Probenoberfläche erlauben eine 2D- oder sogar 3D-Darstellung der Verteilung der optischen Absorptionen. Das OPUS-System ist für die medizinische Anwendung insbesondere zur Brusttomographie vorgesehen. Ein Augenmerk liegt dabei auf der quantitativen Analytik zur Bestimmung der Sauerstoffkonzentration in Blut. Die Leistungsmerkmale des OPUS-Systems wurden durch Messungen an Phantomen bestimmt. Die Entwicklung und Charakterisierung der Phantom- und Absorbermaterialien sind ebenfalls Teil der vorliegenden Arbeit.

Contents

I. Introduction **3**

1. Breast cancer: Methods of detection 3
2. Photoacoustics - A history 5
3. Task 6

II. Background **9**

1. Photoacoustic spectroscopy 9
   - 1.1. Photoacoustic signal generation 9
   - 1.2. Detection 10
   - 1.3. Light propagation 12
   - 1.4. Sound propagation 12
   - 1.5. Depth resolution 14
   - 1.6. Classification of absorbing media 16
   - 1.7. Theory of signal generation 17
   - 1.8. Photoacoustic tomography 19
2. Photoacoustic systems - An overview 19
3. Quantitative photoacoustic 23

III. Phantoms for photoacoustic spectroscopy and tomography **29**

1. Materials and methods 30
   - 1.1. Phantom preparation 30
   - 1.2. Absorbers 32
2. Acoustic characterization 33
   - 2.1. Acoustic property measurements 33
   - 2.2. Results of the acoustic characterization 36
3. Optical characterization 39
   - 3.1. Spectroscopical measurements 39
   - 3.2. Results of the optical characterization 44

4. Discussion 58
5. Conclusion 60

IV. OPUS System **61**
1. System overview and performance 61
1.1. Detection system and triggering 62
1.2. Light source 63
1.3. Optoacoustic unit 66
2. Image reconstruction and evaluation 68
2.1. Image reconstruction algorithms 68
2.2. Image evaluation 78
2.3. Results of the evaluation 81
3. First Results with the OPUS system and a PA sensor stick 87
3.1. Pre-test 87
3.2. Imaging of a human vein 89
3.3. Angular dependence 89
4. Quantitative analysis 91
4.1. Sheep blood 93
4.2. Dye mixtures 94
4.3. ICG 96
4.4. Black ink 98
5. Discussion 100
6. Conclusion 102

V. Summary **105**

A. Abbreviations **i**

B. Symbols **iii**

I. Introduction

1. Breast cancer: Methods of detection

In industrial countries, one woman in eight has or will develop breast cancer in her lifetime [1]. Breast cancer is the second leading cause of death by cancer for women after lung cancer. Early detection is vitally crucial. When tumors are detected early, the five-year survival rate exceeds 95 % and tens of thousands of lives per year may be saved.

Early breast cancer typically shows no symptoms as long as the tumor is small and best treatable. Two common examination methods to find tumors are the clinical breast examination (CBE) and the breast self-examination (BSE) [2]. For women that are at average-risk and asymptomatic, it is recommended that a breast examination should be part of a regular health examination. The examiner will gently feel the breasts, giving attention to their shape and texture, and to the location of any lumps [2]. Furthermore, the area under both arms will be examined. For the breast self-examination, a woman should receive instructions by a healthcare professional experienced in clinical breast examination.

Next to these tactile methods, breast imaging methods play an important role, especially within screening and diagnosis of symptomatic women. Imaging methods for breast cancer detection should fulfill the following requirements: They should have high specificity and sensitivity, they should not take up large amounts of time, money or manpower, and they should be non-invasive and safe [3].

The commonly used method is the X-ray mammography, a low-dose X-ray procedure allowing the visualization of the internal structure of the breast. With respect to sensitivity, 5% - 15% of breast cancers are not detected mammographically [4]. The primarily limitation of X-ray mammography is the imaging of radiographically dense breast [5]. Approximately 25% of women have dense breast tissue [6] resulting in problems to use mammography as general screening method. In most

cases additional tests like biopsies are required to distinguish between benign and malignant lesions. Furthermore, one of the risks of X-ray mammography is the carcinogenic potential of the ionizing radiation [7, 8]. For these reasons, there is a continuous search for other imaging methods that suit for breast cancer screening.

Within this search, ultrasound imaging emerged as an useful method that avoids the carcinogenic hazards of ionizing radiation. In ultrasonography, a sound wave, usually produced by a piezo-electrical crystal, is coupled into the medium, where it becomes backreflected from parts of the medium with a different impedance, which is a measure for the resistance against the wave propagation. The backreflected wave is measured. The propagation time of the wave and the backreflected provides the information about the location of the reflecting object. The application of ultrasound in breast imaging was first mentioned by Wild [9] in 1951. Wild also gave an explanation of the principle of the ultrasonograph and reported that ultrasonic waves showed no harmful effects in his experiments. More detailed descriptions about the physical basics and engineering principles of ultrasound can be found in [10] and [11]. The main role of ultrasound for breast imaging (B-mode scanning) is the differentiation between cysts and solid masses [12], leading to a reduction in the number of biopsies. In addition, ultrasound can also be applied to dense breast tissue. The limitations of ultrasound in screening for breast cancer include the inability to depict microcalcifications, difficulties in imaging fatty breasts, the inability in differentiating benign from malignant solid masses, and an unreliable depict of solid masses smaller than 1 cm [13]. Sonographic equipment for breast imaging has continued to improve; but rather than replacing mammography, the role of sonography has evolved to that of an indispensable adjunct to mammography [14].

Another promising method in breast imaging is the magnetic resonance imaging (MRI). This technique utilizes the interaction between the magnetism of atomic nuclei and radio waves to depict the structure of biological tissues primarily based on their hydrogen content. An introduction to the physical principles of MRI is given e.g. by Leach [15]. The biological effects of magnetic fields and radiofrequency radiation applied in MRI have been reviewed by Bernhardt [16]. The important parameters in MRI to distinguish between different tissues are the T_1 and T_2 relaxation times. Some first relaxation time measurements of tumors showed the possibility of differentiating between benign and malignant lesions [17]. Based on

this, several studies have been carried out to evaluate the possibility of in vivo characterization of breast lesions. One of this studies demonstrated that MRI detects carcinomas as frequently as mammography and additionally allows to discriminate between benign and malignant tissue that was suspicious for carcinoma on mammography [18], but causes high cost for scanning. Although further developments, as for example the design of breast coils that replaced the whole-body imaging coils, makes this method an efficient tool, MRI has not found its final role in breast imaging, but shows promise as potential adjunct to mammography [18, 19, 20].

Further methods used for breast imaging described in literature are computer-tomography (CT) and positron-emission-tomography (PET) [21, 19], microwave imaging [22], and near-infrared optical mammography [23, 24, 25, 26]. Since these imaging techniques are not used for routine screening, a detailed description is abandoned, but can be found in the cited literature.

In this long search for new imaging techniques supporting or even replacing mammography, the old physical principles of photoacoustic (PA) find their new application in breast imaging. First prototypes of photoacoustic mammoscopes are under development [27, 28, 29] or even in trial phase [30]. One of these PA mammoscopes, the OPUS system is the subject of this work.

2. Photoacoustics - A history

The photoacoustic effect was first mentioned in 1880 by *Alexander Graham Bell* [31, 32, 33]. Together with his friend and colleague *S. Tainter*, he discovered that modulated solar radiation, which was focused onto a segment of selenium, produces a sound signal. Thus, a few years after the construction of his telephone, he developed a "photophone" based on the new findings. Through a mirror placed on a membrane he modulated sunlight with his voice. The modulated light was on his part reconverted into a sound wave at the receiver side by the photoacoustic effect [34]. He observed and studied the photoacoustic effect on gases, solids and colored water. Next to Bell, the photoacoustic effect was also observed by

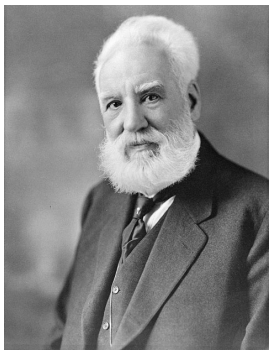

Figure I.1.: Portrait of Alexander Graham Bell c. 1910

the scientists *J. Tyndall* [35] and *W.C. Röntgen* [36] in 1881. Since the excitation sources during that time were not efficient enough for applications, the interest on the photoacoustic effect was fading.

Several decades later, photoacoustics experienced its revival with the development of the laser, a stronger excitation source opening the gates for new applications in this field. In the 70s and 80s of the 20th century, the photoacoustic effect was used for analytical problems. In the first experiments, chopped light was used to produce sound waves in the audible range which were detected by a microphone [37, 38, 39]. With the use of piezoelectric detectors, the sound waves in the ultrasound range could also be detected. Additionally, optoacoustic detectors made from piezoelectric detectors exhibited fast response time and sufficient sensitivity to perform on-line studies of thermal deactivation processes [40], which made them interesting for many analytical applications. Next to the analysis of gases [41], the method was used to examine biological materials [42]. The detection of photoacoustic signals is most commonly performed by piezoceramics or polyvinylidene fluoride (PVDF) films [43]. Another sensor type used for photoacoustic measurements is the optical interferometer [44, 45, 46]. Photoacoustic signals produced in gases are detected by microphones as shown for example in [47, 48].

3. Task

This work is about the OPUS project, which has been financially supported by the Bavarian State Ministry for the Economy, Infrastructure, Transportation and Technology within the framework of the BayMed program. The OPUS project is a cooperative project between the Institute of Hydrochemistry (Technical University Munich, Munich), InnoLas (Krailling) and GE - Global Research (Garching b. München). The name OPUS stands for OPtoacoustic plus UltraSound. Goal of the project is the development of a photoacoustic system as an add-on to a commercial ultrasound system for breast cancer detection. GE as distributor of commercial ultrasound systems has been responsible for the modification of the ultrasound system, the trigger system between ultrasound system and laser, and the development of reconstruction algorithms [49]. The scope of the laser distributor InnoLas has been to develop a laser satisfying the requirements regarding repetition rate needed for this application and with regard to pulse-to-pulse stability, which is important

for medical applications [50, 51]. The Institute of Hydrochemistry had the responsibility to develop a sensor probe for first tests [52], to design the optoacoustic coupling between laser and ultrasound scanner, to built and test phantoms for this special purpose, and finally to test and evaluate the system.

The aim was to optically and mechanically couple the laser and the ultrasound system to enable photoacoustic measurements in addition to ultrasound scanning. Another part was the development of phantoms that possess optical as well as acoustic properties of breast tissue that should be mimicked. The main aim was to test and evaluate the performance of the optoacoustic system with the phantoms and to find an adequate procedure to quantitatively analyze the data. Since with the system it is aimed to distinguish between different levels of oxygen saturation in blood, a proper quantitative analysis is needed.

Chapter II provides a short review of the theoretical background and an overview about the current state of research of comparable PA systems.

The phantom materials and their preparation are described in chapter III. The phantoms have been acoustically (section 2) and optically characterized (section 3).

The OPUS system is presented in chapter IV. The chapter comprises the description and performance of the system as well as the realization of the opto-mechanical coupling of the laser and the ultrasound scanner (section 1). Furthermore, it includes the reconstruction algorithms and their evaluation (section 2), first results with the system of the different generations (section 3) and some quantitative results (section 4).

II. Background

In photoacoustic imaging, optical inhomogeneities of a sample are visualized based on their absorption characteristics. The processes involved in this imaging modality are the photoacoustic effect for the initiation of the acoustic wave, the acoustic wave propagation, the detection of the sound wave, and finally the reconstruction to receive a map of the optical inhomogeneities of the sample from the measured signals. These processes are mostly discussed in this chapter. Furthermore, some photoacoustic systems are exemplarily presented. Since the photoacoustic signal amplitude depends on the absorption coefficient, quantitative information about the local absorption can be revealed. The possibilities for quantitative analysis are subsequently discussed in this chapter.

1. Photoacoustic spectroscopy

Photoacoustic spectroscopy belongs to the category of absorption spectroscopical methods. In photoacoustic spectroscopy the absorption of a certain structure is measured by detecting sound waves induced by absorbed laser light.

1.1. Photoacoustic signal generation

The photoacoustic effect describes the conversion of an electromagnetic wave into a pressure wave. Pulsed lasers or amplitude modulated *continuous wave* lasers (cw-laser) are typically used as excitation sources. Since for this work only pulsed lasers were used, the following description of the mechanism of pressure wave generation is restricted to this method. The single steps of the photoacoustic signal generation are pictured in figure II.1.

Radiating a sample with a short laser pulse in the range of nanoseconds, the energy is locally absorbed in the medium depending on the local absorption coefficient

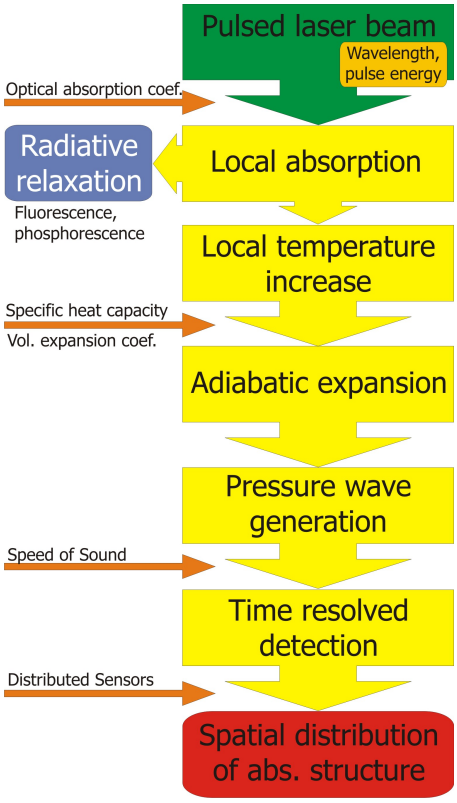

Figure II.1.: Flowchart of the photoacoustic signal generation and detection.

$\mu_a(r)$. This local absorption coefficient is wavelength dependent. The deposited energy can be transferred via the radiative relaxation processes fluorescence and phosphorescence or by radiationless relaxation. Radiationless relaxation processes cause local heating of the medium. The thermal absorption depends thereby on the specific heat at constant pressure C_p. The local heating lead to a volume expansion characterized by the volume expansion coefficient β. The volume expansion cause an increase in pressure. This pressure increase moves at the speed of sound c_0 through the sample and can be detected time- and spatially-resolved at the surface. If the speed of sound of the medium is known, the origin of the pressure wave can be traced back by the time duration between pulse generation and detection.

1.2. Detection

Detecting photoacoustic pressure waves gives information about optical inhomogeneities. In pulsed photoacoustic spectroscopy, there are two detection geometries,

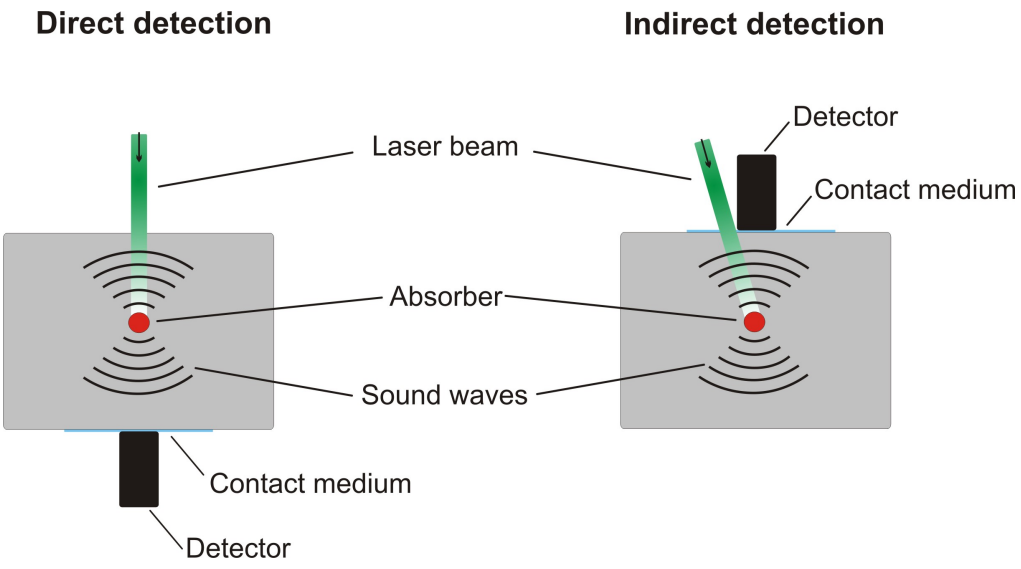

Figure II.2.: Schematic of direct and indirect detection.

the direct and indirect detection which are depicted in figure II.2. In the presented case of a point source, the induced pressure waves propagate into all directions.

Direct detection

For the direct detection, the detector is positioned at the opposite side of the light source. The pressure waves propagate parallel to the laser beam. The detector will register two pulses. The first pulse is the pressure wave that travels straight forward in the direction of the detector. The second is a reflection of the pressure wave on the surface of the sample.

Indirect detection

The indirect detection takes place at the same side as the radiation. In general, a transparent detector or a transparent medium between detector and sample enables the irradiation of the sample underneath the detector. The acoustic signal that will be detected is only the single pressure wave propagating straight to the detector. The indirect detection is used for samples that are only accessible from one side as it is the case in most medical applications.

In both detection geometries as presented in figure II.2, the detector is placed in a distance to the sound source which is not in the acoustical near-field thus

diffraction effects are not neglectable. Since for the OPUS system a detector array was used instead of a single detector, the diffraction effects were considered in the reconstruction.

1.3. Light propagation

The photoacoustic pressure wave gives information about the locally absorbed energy depending on the energy distribution within the sample. The energy distribution is conditioned by the light propagation. The light propagation depends on the optical properties of the sample as well as on the initial energy distribution.

In non-scattering samples, the direction of the light beam stays unchanged. The light propagation can be calculated according to the laws of the geometrical optics [53]. Only absorption and diffraction are of importance.

In scattering samples, the light propagation is additionally influenced by the scattering coefficient and the anisotropy factor. The photoacoustic signal amplitude becomes therewith indirectly influenced by the scattering. The light propagation in scattering samples is more difficult to describe. Different models and methods are used to simulated light propagation to obtain analytical information from the pressure signals; for example the Monte-Carlo-Method [54].

1.4. Sound propagation

The distribution of the optical inhomogeneities can be achieved from the detected sound wave by knowledge of sound propagation behavior.

Sound wave

A sound wave is a mechanical, spatio-temporal oscillation of an expanded matter. This means, that the particles, which build the matter, deflected from their rest position, oscillate around the rest position. The disorder of the rest position moves with the velocity $c = \Delta x/\Delta t$ through the matter. This velocity is called the speed of sound and is a matter constant. Sound waves are longitudinal waves [11].

In photoacoustic measurements, the detector measures the time dependent pressure perturbance $p(\vec{r}, t)$. For constant speed of sound, there is a relation between the

origin of the pressure wave and the time interval, that the wave needs to arrive at the detector. This is described by the retardation

$$p\left(\vec{r},t\right)=p\left(\vec{r},t-\frac{|\vec{r}|}{c_0}\right). \tag{II.1}$$

The retardation allows to trace back the origin of the detected sound wave.

Acoustic impedance

Another measure influencing the sound propagation is the acoustic impedance Z, which is a matter constant. It is a quantity for the resistance that a wave experiences propagating through the matter. Therefore, it is also called the wave resistance [11]. The acoustic impedance is related to the matter constants speed of sound c_0 and density ρ_0 by

$$Z=\rho_0\cdot c_0. \tag{II.2}$$

It plays a role for sound waves passing the boundary between two media (medium 1 and medium 2). Depending on the difference between the impedances, parts of the sound wave become reflected and parts are transmitted. The reflected part of the sound energy can be calculated knowing the impedances. Analogue to optics, reflected and transmitted parts can be calculated with the Fresnel's equations for the perpendicular incidence

$$T_a=\frac{E_a^T}{E_a}=\left(\frac{2Z_2}{Z_2+Z_1}\right) \qquad \text{and} \tag{II.3}$$

$$R_a=\frac{E_a^R}{E_a}=\left(\frac{Z_2-Z_1}{Z_2+Z_1}\right) \tag{II.4}$$

with transmission coefficient T_a and reflection coefficient R_a. If medium 2 has a greater acoustic impedance than medium 1, the sound wave becomes reflected and

the reflection coefficient is positive. The reflection coefficient is negative for the reverse case and the phase of the reflected wave will be inverted [55]. If the sound wave has to propagate through several boundary layers j, the resulting coefficients for reflection and transmission are obtained by multiplying the coefficients of the single boundary layers, that is

$$T_a^{res} = \prod_j T_a^j \qquad \text{and} \qquad R_a^{res} = \prod_j R_a^j. \tag{II.5}$$

The sound energies are proportional to the squares of the sound intensities. For an ideal acoustic transparent matter without losses of sound intensity, the relation between the reflected and transmitted parts is given by

$$(T_a)^2 + (R_a)^2 = 1. \tag{II.6}$$

For the direct detection, the reflected sound wave depends on the difference of the acoustic impedance between the sample and the surrounding matter. It can change its phase and interfere with the non-reflected wave. For the indirect detection, the signal is not influenced by the reflected wave, but the signal amplitude is dependent on the difference in the acoustic impedance.

In both cases, the impedance of the surrounding matter Z_m or the contact medium Z_{tr} between sample and detector has to be adjusted. Meaning that a material has to be chosen with an acoustic impedance similar to that of the sample $Z_{m,tr} \approx Z_0$. This is important to minimize the loss of information.

1.5. Depth resolution

The frequency spectrum of the laser-excited sound waves is the Fourier transform of the spatial distribution of the acoustic sources [55]. This means, that the depth dependent absorption coefficient $\mu_a(z)$ defines the modulation of the photoacoustic signal. The depth resolution δz can be extracted from the detected, time-resolved δt pressure signals by

$$\delta z = c_0 \cdot \delta t. \tag{II.7}$$

Some specific conditions have to be fulfilled until equation II.7 becomes valid. The most important processes are characterized by their running times, the acoustic relaxation time t_a and the thermal relaxation time t_χ.

Acoustic relaxation

The acoustic relaxation time is dependent on the absorption coefficient μ_a. The pressure relaxes during the time it takes for the acoustic pulse to transit the heated region and is expressed as [55]

$$t_a \propto (\mu_a c_0)^{-1}, \tag{II.8}$$

where μ_a^{-1} is the mean penetration depth. This means, the relaxation time is short for small penetration depths. If the laser pulse τ_L is short compared to the acoustic relaxation time t_a

$$\tau_L \ll t_a, \tag{II.9}$$

the shape of the acoustic wave excited follows the spatial distribution of the heat sources [55].

Thermal relaxation

The thermal relaxation time is depends on the square of the absorption coefficient μ_a and takes place very slowly [55]. It gives the time duration, that the deposit thermal energy needs to leave the probe element by diffusion. Its characteristic time scale is

$$t_\chi \propto \left(\mu_a^2 \chi\right)^{-1} \gg t_a, \tag{II.10}$$

where χ is the thermal diffusivity of the medium [55]. As mentioned in paragraph 1.1, in photoacoustics the deposited energy is adiabatically transformed into an acoustic wave. Hence, the condition for the adiabatic volume expansion is fulfilled and the thermal diffusion can be neglected.

1.6. Classification of absorbing media

Media that are examined in their absorption structure can be classified with respect to their optical distinctions.

Homogeneous media

Homogeneous media have identical optical properties in every part of the sample volume. That means, they can be described by a constant absorption coefficient

$$\mu_a = const. \tag{II.11}$$

Homogeneous media are used for the derivation of the photoacoustic signal.

Macro inhomogeneous media

In macro inhomogeneous media, the absorption coefficient is space dependent

$$\mu_a = \mu_a(\vec{r}). \tag{II.12}$$

Most samples used in the experiments in this work are macro-inhomogeneous.

Micro inhomogeneous media

Micro inhomogeneous media content light absorbing centers or particles, with a mean distance of a few micrometer between the particles. The absorption coefficient $\mu_a(\vec{r})$ varies on the microscopic scale. The absorption coefficient is composed of the macroscopic absorption behavior of the media $\mu_a^{macro}(\vec{r})$ and the microscopic distribution of the particles $\mu_a^{micro}(\vec{r})$. The particles have thereby a uniform absorption coefficient

$$\mu_a^p = const. \tag{II.13}$$

In micro inhomogeneous media, scattering plays also a role, since, the particles work not only as absorption but also as scattering centers.

1.7. Theory of signal generation

In this section, the photoacoustic amplitude is formally affiliated. Assuming pulsed laser light for the illumination with a single pulse energy of E_0 and a homogeneous absorbing medium, the energy absorbed (E_a) by the medium through a depth z is given by [56]:

$$E_a = E_0 \left(1 - e^{-\mu_a z}\right). \tag{II.14}$$

For $\mu_a z << 1$, the absorbed energy can be linearly approximated by a TAYLOR-series expansion. Hence, equation II.14 can be oversimplified as [56]:

$$E_a \approx E_0 \mu_a z. \tag{II.15}$$

Assuming that radiationless relaxation predominates in the medium, the thermal energy E_{th} is given by [56]

$$E_{th} = E_a = E_0 \mu_a z. \tag{II.16}$$

With knowledge of the specific heat at constant pressure C_p, the change in temperature ΔT of the illuminated volume V with density ρ (neglecting thermal conduction) is given by [56]:

$$\Delta T = \frac{E_{th}}{C_p \rho V} = \frac{E_a}{C_p \rho V}. \tag{II.17}$$

The temperature change leads to a volume expansion ΔV outgoing from the equilibrium condition V_0 which is described by the volumetric expansion coefficient β. It can be derived from the definition of the volumetric expansion coefficient [57]:

$$\Delta V = V_0 \beta \Delta T. \tag{II.18}$$

For adequate short laser pulses, the volume expansion can be considered as adiabatic. This expansion induces a pressure wave that travels through the medium with the material-specific speed of sound c_0. That pressure change can be described by [58]:

$$\Delta p = c_0^2 \rho \beta \Delta T, \tag{II.19}$$

where ρ is the density of the medium. Stating the volume V as the product of the illuminated surface F_S and the illuminated depth in the medium, and inserting equation II.17, lead to the following equation for the pressure change:

$$\Delta p = \frac{1}{F_S z} \frac{\beta c_0^2}{C_p} E_{th}. \tag{II.20}$$

With the linear approximation for E_{th} (equation II.16) the expression of the pressure change simplifies itself to:

$$\Delta p = \frac{1}{F_S} \frac{\beta c_0^2}{C_p} E_0 \mu_a. \tag{II.21}$$

For fixed geometry of laser illumination and laser properties, the illuminated surface and thereby its reciprocal as well can be taken as constant [56]. Hence, equation II.21 is reduced to:

$$\Delta p \propto \frac{\beta c_0^2}{C_p} E_0 \mu_a. \tag{II.22}$$

The amplitude of the laser induced pressure wave for a fixed illumination geometry is finally dependent on the excitation energy E_0, the volumetric expansion coefficient β, the specific heat at constant pressure C_p, the material-specific speed of sound c_0, and the absorption coefficient μ_a. To quantify absorption coefficients by photoacoustic pressure amplitudes the first four variables have to be kept constant and must be known. For known absorbers with unknown material-specific condition of the surrounding medium another approach must be chosen. Examples are presented in section 3 in this chapter.

1.8. Photoacoustic tomography

In the previous sections, photoacoustic spectroscopy was discussed for the 1-dimensional case of a distribution of absorption inhomogeneities $\mu_a(z)$.The distribution of absorption inhomogeneities $\mu_a(\vec{r})$ can also be examined in 2D or 3D, which is called photoacoustic tomography.

One possibility to obtain the distribution of absorption inhomogeneities in a volume, is to make several depth scans, the so-called A-scans (1D). For these measurements, the detector should be straightened to receive only the sound waves that are from one direction. The detector is moved along an axis (x-axis) over the surface from measurement to measurement. When the depth scans generated this way are pieced together, they result in a 2D cross section or alternatively a slice image through the volume. Moving the detector over the full top surface of the volume and taking depth scans at each coordinate of this plane, the depth scans result in a 3D image.

Another possibility is the usage of a detector array, where the single detectors are arranged in a row along the x-axis on top of the surface. A depth scan of the array produces a cross section. Taking cross sections with the array along the y-axis, the images stringed together result in a 3D image as well.

The reconstruction in the 2- or 3-dimensional space can get arbitrarily complicated, since processes as diffraction, impedance steps or the interference of the sound waves of different origins play a role. Additionally, it is influenced by the directivity of the detector and the light distribution. There exist several approaches for the reconstruction. Some of them are discussed in chapter IV, section 2.

With the possibility to receive tomographic information of a volume, photoacoustic is interesting for medical application such as the visualization of lesions.

2. Photoacoustic systems - An overview

In this section, a few photoacoustic systems are depicted, including systems using commercial ultrasound scanner, systems for breast scanning, systems for mice imaging, and a system with a Fabry Perot polymer film as sound detector.

Combined US and OA system described by J.J. Niederhauser

A combined ultrasound and optoacoustic system for real-time high-contrast vascular imaging for *in vivo* use is presented by J.J. Niederhauser *et al.* [59]. The laser source of the system is a Q-switched alexandrite laser (Storz Medical) with 7.5 Hz repetition rate and a pulsewidth of 60 ns at 760 nm working wavelength. The light is led fiberoptically to the ultrasound transducer, where it is guided by a prism and two mirrors around the transducer to illuminate the tissue with an energy density of 5 mJ/cm^2. The detection unit consists of a linear array ultrasound transducer LA/7.5/128/ULS (Vernon S.A., France), with a center frequency of 7.5 MHz and a bandwidth of 76 %, and a digital phased array ultrasound system (DiPhAS) designed by Fraunhofer Institute for Biomedical Engineering (St. Ingbert, Germany). The ultrasound system is designed to acquire data of all transducer elements parallel at a 30-MHz sampling rate and to transfer the data in real-time to a processor. Since the frame rate is limited by the laser repetition rate, a frame rate of 7.5 Hz is achieved. The system has a lateral resolution restricted by the element pitch to 0.4 mm and a depth resolution of about 0.3 mm at a transducer bandwidth of 5.5 MHz. *In vivo* studies showed the capability of the system to photoacoustically image vessels in human finger, leg and arm with high contrast.

Philips system

The Philips system is a photoacoustic scanning system that is based as the OPUS system on a commercial ultrasound system and is used for imaging nude mice. The following facts are based on the sources [60, 61]. The photoacoustic system is build around the commercial Philips-ATL HDI-5000 ultrasound scanner. A data acquisition board is added to acquire raw radiofrequency data per transducer channel. Although all standard HDI-5000 compatible transducers are usable with the system, it was tested with the CL15-7 compact hockey-stick probe, which is a broadband linear array with a center frequency around 8 MHz. As light source serves a Nd:YAG-pumped OPO laser system (laser: Q-switched Brilliant B, Quantel; OPO: VIBRANT I, Opotek Inc.) with a repetition rate of 10 Hz and a wavelength range of 650 - 950 nm. The light is led over a fiber bundle to the surface. The system works in backward mode. The acquisition board enables dual PA-US mode with a frame rate of 4 frames per minute. While the ultrasound images generated in regu-

lar B-mode are undergoing a delay-and-sum beamforming algorithm in the scanner, the photoacoustic images are beamformed by a Fourier approach externally at a PC. The systems resolutions are specified to be 240 μm axially and 360 μm laterally based on FWHM definition.

PAM Photoacoustic Mammoscope

The Photoacoustic Mammoscope (PAM), based on a parallel plate geometry, was developed at the University of Twente. The breast is thereby gently pressed between a glass plate and a flat high-density ultrasound detector matrix with 590 elements. A Q-switched Nd:YAG laser (Quantel Brilliant-B) operating at 1064 nm with a pulse duration of 5 ns and a repetition rate of 10 Hz is illuminating the breast through the glass plate. The detector consists of a 110 μm thick polyvinylidene fluoride (PVDF) sheet of approximately 90 mm in diameter with thin gold electrodes arranged in a circular grid. The light is led over a liquid light guide to the glass plate and is moved across the plate to obtain all regions of interest. For a volume of interest of approximately 37 mm $\times$ 31 mm, the scanning time is rated to 20 min with 128 averaged signals per element. The scanner is able to detect inhomogeneities of 2 mm diameter down to 32 mm depths with a resolution of 3.5 mm. First clinical trials showed promising results in recognizing regions of tumor vascularization. One observed disadvantage is the difficulty for the patients to lie still for the long periods of measurement [29, 62, 30].

LOIS

The laser optoacoustic imaging system (LOIS) is a photoacoustic tomograph built to image breast cancer and was designed by the group around A. Oraevsky. Former generations of the LOIS has been reported in [63, 64, 65, 66, 67]. The present system, currently used in clinical trials, named LOIS-64/16 in [27] and LOIS-B in [28], will be depicted in the following.

The LOIS-64/12 has two laser sources to enable multiple wavelength measurements. One is a Nd:YAG laser (Brilliant B, Big Sky Laser/Quantel) at a working wavelength of 1064 nm with a pulse duration of 6 ns and a repetition rate of 10 Hz. The other is an alexandrite laser (601-X, Light Age Inc.) with a pulse duration of 75 ns and a 10 Hz repetition rate at 757 nm. The laser light is led to the patient where

it illuminates the surface of the breast with an energy density of about 20 mJ/cm^2. The photoacoustic signals are detected by an acoustic probe consisting of an arc of 64 PVDF transducers and a linear array of 16 PVDF transducers on the back of the probe. The system has a lateral as well as a vertical resolution of 0.5 mm [27].

Photoacoustic scanner with a Fabry Perot polymer film sensor

The photoacoustic scanner based on the detection with a Fabry Perot polymer film sensor was developed by the photoacoustic imaging group at the University College London. In earlier versions of the system, it was described for an operating wavelength of 1064 nm [68, 69].

As excitation source a fiber coupled tunable (410-2100 nm) OPO laser system is used with 8ns pulse duration. The sensor consists of a wedged transparent polymer backing stub and a multilayer sensing structure, which is a sandwich of a Parylene polymer film spacer between two dichroic dielectric mirrors, that are highly transmissive for wavelengths between 590 nm and 1200 nm. The system is designed to work in the backward-mode. The sensor is placed in acoustic contact with the tissue and the excitation laser illuminates the tissue through the sensor. The surface of the sensor is raster scanned by a 1550-nm focused cw laser beam. The photoacoustic waves become measured by detecting the reflected intensity modulation of the cw laser light with a photodiode. The raster scanning of the surface is comparable to a 2D ultrasound array. 3D images are obtained by reconstructing the signal map by a k-space backpropagation algorithm. The bandwidth, and therewith the resolution, are dependent on the thickness of the Fabry Perot polymer film. With a film thickness of 22 μm (-3 dB bandwidth of 39 MHz), a scan laser beam spot of 64 μm, a scan step size of 20 μm, and a detection aperture of 40 mm, lateral and vertical resolution of approximately 40 μm and 20 μm were achieved. The system is capable of high resolution 3D imaging of small vessels close to the surface. [70, 71, 46, 72]

In vivo studies showed the capability of the scanner to 3D image human tumors grown subcutaneously in mice with high resolution [73].

PA tomograph for quantitative imaging of rat brains

The group around Lihong Wang at the Washington University in St. Louis has described several small animal imaging systems [74, 75, 76, 77] as well as a system for biological tissue imaging with an intensity-modulated continuous-wave laser [78]. The system, that was chosen to be described in this section, is used for noninvasive imaging of hemoglobin concentration and oxygenation in rat brain and is presented in detail in [79].

Its light source is a tunable dye laser (ND6000, Continuum) pumped by a Nd:YAG laser (Brilliant B, Bigsky) with a pulse duration of 6.5 ns and a repetition rate of 10 Hz. The rat head becomes illuminated on the top with an energy density of < 3 mJ/cm^2. The photoacoustic waves are detected by an unfocused ultrasound transducer (XMS-310, Panametrics) with a central frequency of 10.4 MHz, which is circulating around the head with a scanning radius of ~ 3 cm and a scanning step size of 1.5 deg. During the measurements, the imaged part of the rats head as well as the transducer are positioned in a water tank for acoustic coupling purposes. In the center of the scanning circle a lateral resolution of ~ 60 μm is achievable. With stable energy, the smallest detectable changes in hemoglobin concentration and oxygenation are in the range of 0.4 %. [79]

3. Quantitative photoacoustic

Rosencwaig has already shown in 1973 [42] that photoacoustic imaging is able to obtain more than a qualitative, spatial distribution of a certain absorber. Photoacoustic imaging is capable to reveal quantitative information about the absorbing substance.

Three steps lead from the raw photoacoustic data to the local chromophore distribution. First step is the reconstruction of the signal map from the raw data array. The conversion from the signal map into the absorption coefficient map is the second step. Since the locally absorbed energy depends on the energy distribution, an adequate model for the light propagation within the volume of interest is crucial. Furthermore, the knowledge of the acoustic properties in the volume of interest is helpful as they influence the pressure wave propagation. Although in general, the complete volume is assumed to be acoustically homogeneous, this

assumption only true to a certain degree and for certain tissue areas. The last step is the quantification of the chromophore concentration, where the focus lies in the discrimination between background noise and analyte signal. [80]

Image reconstruction

The image reconstruction of photoacoustic raw data sets is an extensively discussed subject in literature. It is essential for the signal detection with 1D or 2D linear as well as curve shaped sensor arrays. Since the quantitative information is extracted from the reconstructed image and corresponds to a distinct region of absorption, a proper reconstruction is crucial. Furthermore, the speed of reconstruction which partly depends on the chosen reconstruction algorithm, plays a role for the capability for real-time reconstruction. The most commonly used and discussed reconstruction approaches are iterative algorithms [81], back-projection algorithms including the Delay-and-Sum algorithm [82, 83, 62] and Fourier based algorithms [84, 85, 86]. The basics of the most common approaches are presented by Xu and Wang in [87]. The Delay-and-Sum, a circular back-projection, a Fourier-transform based as well as a Hough-transform algorithm are discussed and compared to each other later in chapter IV, section 2.

Conversion from signal to absorption coefficient

The main focus in photoacoustic tomography is put on the chromophore hemoglobin regarding its concentration and oxidation state in whole blood. The absorption spectra for oxy- and deoxyhemoglobin as well as the absorption spectra for melanin (chromophore in the skin) at different concentrations are presented in figure II.3. The absorption spectrum of hemoglobin depends on the oxygenation state.

The reconstructed data set shall visualize the distribution of the absorption coefficient. But in fact, it is a map of the locally absorbed light amount convoluted with the pressure attenuation of the medium between the location of the light absorption and the detector, which can vary due to acoustic inhomogeneities [80]. Hence, for the conversion from signal to absorption coefficient the signal map has to be corrected firstly for the local light distribution and secondly for the acoustic inhomogeneity distribution. While the local light distribution may vary significantly due to strong absorption and scattering in tissue, biological tissue is according to

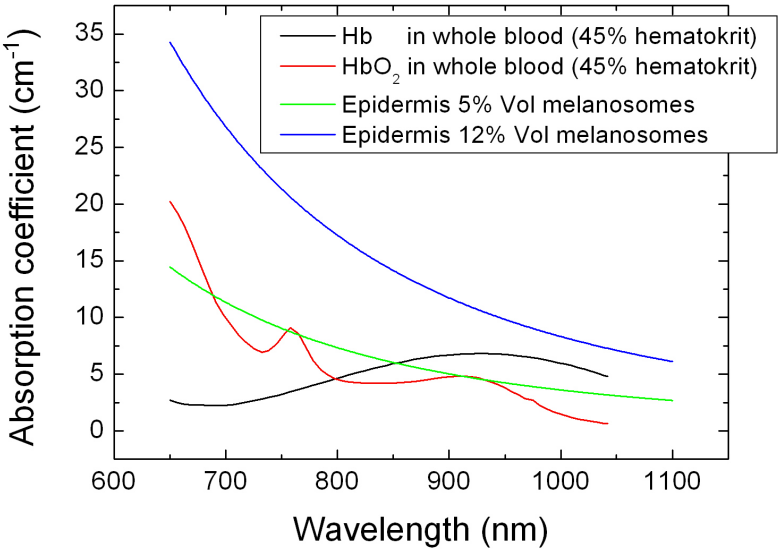

Figure II.3.: Absorption spectra of oxygenated and deoxygenated hemoglobin as well as of the epidermis (melanine) (Data source: http://omlc.ogi.edu/spectra/index.html, downloaded 19.November 2007).

[88] ultrasonically non-dispersive, hence, ultrasound generation and further propagation of the attenuating sound waves can be treated as linear.

For 1D photoacoustic signals (A-scans), a mathematical way to gain quantitative information from the signal was described by Karabutov *et al.* [55], who characterized the signal slope as proportional to the absorption coefficient. This way of quantification was later also used by Esenaliev *et al.* [89] for monitoring blood oxygenation in the brain by 1D photoacoustic signals. They found a correlation between the oxygenation and the absolute photoacoustic signal amplitude as well as the signal slope. In contrast to the amplitude, the slope of the normalized signal showed itself insensitive to optical and acoustic transmission of tissues between the sensor and the blood. Brecht *et al.* [90] stated that the amplitude cannot be used to monitor blood oxygenation *in vivo* with the necessary exactness without corrections. But they found the integral of the normalized signal to be robust for monitoring the blood oxygenation in large vessels in real time. Although these approaches work for the 1D case, their application in 2D or 3D image evaluation is not known. Maslov *et al.* [91] showed that it is possible to measure the hemoglobin oxygen saturation using the peak amplitude of the photoacoustic image. They

considered the peak amplitude as the only parameter that can be separated for the analysis of micro-vascular imaging *in vivo*. According to Sivaramakrishan *et al.* [88], a quantification based on this method is only feasible under the condition that the central frequency of the transducer, which limits the spatial resolution, has to be shorter than the penetration depth of light in the imaged structure. That means, if the origin of the acoustic wave can be resolved, only the signals of the relevant region are taken into account. Therewith, the signals of the surrounding area cannot falsify the results. This condition was tested for small vessels close to the surface. They showed that in a wavelength range of 570 - 600 nm with central frequencies of the transducer above 25 MHz accuracy of ~ 4 % can be achieved in *in vitro* measurements.

Another approach is that of multiple wavelength measurements. Relative quantification is less sensitive to inhomogeneous light distribution. The common task in quantitative photoacoustic imaging, the determination of blood oxygenation, can be performed by two-wavelength measurements. Usually one wavelength is chosen at an isosbestic point of oxyhemoglobin and deoxyhemoglobin. Their ratio can then be calculated from the known molar absorption coefficients at the two wavelengths. Additionally, the total hemoglobin concentration can be obtained by this method. The determination of blood oxygen saturation as well as of the hemoglobin concentration using the two-wavelength approach was demonstrated by Wang *et al.* [79] imaging rat brains. Although this method is less sensitive to inhomogeneous light distribution, they state that, for studying the metabolism in the brain, the affecting optical parameters such as wavelength dependent absorption and scattering of the skin, skull and surrounding tissue, have to be further investigated. Zemp *et al.* [92] developed a mathematical model to improve the accuracy of the quantitative analysis by operating at more than two wavelengths. They formed a system of linear equations, that reflects the relation between the measured signals at different wavelengths and the known molar extinction coefficients for the two analytes at these wavelengths. Furthermore, they discussed the limitation of this approach. The absorption coefficient shows no significant change for wavelengths that are spectrally close. Besides, the reconstructed image does not necessarily reflect the quantitative absorber distribution for three reasons. First: the imaging system is sensitive to only a radial band of frequencies. Second, the reconstructed image is in a sense a projection of photoacoustic signals into the imaging plane and the extent and weighting of signals of different depths, meaning that they depend

on the depth resolution of the imaging system. The third reason is, for strong absorption, where all incident light is absorbed, the photoacoustic signal becomes proportional to the incident laser energy, and thereby, independent on the molar extinction spectra. Hence, this approach can only be performed when the depth resolution is less than the optical attenuation. This matches with the conditions concerning the spatial resolution of the imaging system which is dependent on its frequency response postulated in [88].

Another promising approach was presented by the research group of P. Beard. They developed a forward model for quantitative photoacoustic imaging, that reaches from the light distribution over the signal generation to the acoustic wave propagation. The absorption distribution can be solved by the inversion of the model and by iteratively adjusting the input data until the calculated and measured signal map match. Cox *et al.* [93] investigated the iterative process and the associated problems. They described that in addition to the optical absorption of the tissue the local fluence has to be iteratively adapted to obtain an absorption map with reasonable precision. Although light distribution is usually simulated by Monte Carlo models [94], Cox *et al.* [93] chose a finite element model, since in their opinion, the Monte Carlo method has two major disadvantages with respect to their applicability in routine photoacoustic image evaluation. It is computationally intense and second, the geometry of absorption and scattering inhomogeneities must be encoded directly [95]. The diffusion approximation would be usable to model light distribution accurately, but since it assumes a near-isotropic light source, it is not able to simulate the highly anisotropic fluence close to the surface of the tissue [93]. To overcome this limitation, the δ-Eddington approximation can be applied, which draws nearer to the predominant forward scattering of biological tissue [96], and therefore, improves the accuracy close to the surface [93]. Based on this improved light transport model, Cox *et al.* [95] theoretically describes the iterative adaption of a calculated absorption map to the measured photoacoustic signal map. They start with an initial value of zero for the absorption coefficient calculating the local fluence. The new absorption coefficient estimate is then calculated from the measured absorbed energy distribution and the calculated local fluence. With the new absorption a new local fluence will be evaluated. The fluence as well as the absorption are iteratively estimated in this way until the calculated absorbed energy distribution is close to the measured one resulting in a final absorption distribution map. The whole procedure is applied assuming that the scattering

coefficient is known. The authors concluded that, although the absorption map can be determined with a known scattering coefficient, the absorbed energy map requires calibration to be used in the described recursive algorithm, which can be achieved by calibrating the ultrasound sensor. On the other hand, they suggest to overcome this problem by calibrating the whole system with phantoms of known optical properties and compare the results with theoretical maps.

In a next step, Beard and his coworkers extended their model from single-wavelength to multiple-wavelength application. Using optical coefficients with known wavelength dependency they obtained accuracies of total hemoglobin concentration below 10 % and of oxygen saturation below 7 %, measured on a phantom and comparing the data to those measured with a CO oxymeter [97, 98]. Since the developed model works for single-point multiwavelength measurements, the model has to be modulated for 2D or even 3D application in photoacoustic imaging. They further investigated a k-space propagation model to improve the accuracy and computational efficiency in 2D photoacoustic imaging as presented in [99].

All approaches mentioned in this section assume homogeneous acoustic properties, which does not reflect the real behavior of tissue. Since photoacoustic signals do not allow the reconstruction of acoustic inhomogeneities, other imaging modalities have to be used for corrections. Such a combination of photoacoustic imaging together with ultrasound imaging was demonstrated by Manohar *et al.* [100]. Even though the optical properties vary strongly, the strength of the influence of the acoustic properties in photoacoustic imaging has to be further investigated.

Quantification of the local chromophore concentration

The last step in quantification of the local chromophore concentration based on the absorption coefficient map is barely discussed in literature. However, some aspects of the evaluation have to be considered: How many and which pixels carry the quantitative information; and, is it more precisely averaging the values for the region of interest or taking the most intense pixel? Since there is no common solution published in literature, an approach based on the assumption of a Gaussian distributed background noise was used for the system presented in this work. Under this assumption, the limit of detection was defined to be 3σ (three time the standard deviation of the Gaussian distribution). A detailed description of this evaluation is given in chapter IV, section 2.

III. Phantoms for photoacoustic spectroscopy and tomography

In medical imaging a phantom is a simulation of a human or animal body part that possesses the relevant physical properties.

Phantoms are widely used in medical imaging for testing or calibrating devices. In optoacoustic imaging the phantoms have to possess both optical as well as acoustic properties of the simulated tissue. In the last decades a large variation of tissue simulating phantoms for optical, optoacoustical and ultrasound imaging have been described. One group of materials described in literature consists of milk [101], gelatine [102, 103, 104], a fat emulsion, intralipid [105, 106, 107, 108, 109], agar [110] and agar-intralipid mixtures [111, 112]. In some intralipid phantoms, India ink was used as absorber [111, 112], for others non-scattering dyes [113]. Unfortunately, those materials are more or less liquid and cannot be used without other materials, with different optical properties, to separate sections with differing absorbing and scattering behavior within the phantom. Another aspect is that these materials do not have a long durability. Some materials, that can be reproducibly shaped into 3D solids and be kept stable over a few months, are polyacrylamide gel (PAA) [114, 115, 116], polyvinyl alcohol gel (PVA)[117, 118, 29, 119], resin [120, 121, 122], wax [123], and polyvinyl chloride-plastisol (PVCP) [124].

1. Materials and methods

1.1. Phantom preparation

Agar

The preparation of agar into 3D solid shapes is straightforward and fast. There is no risk for health during handling and preparation. It is stable for several weeks, when it is stored under water at about 4 °C.

The agarose gel is produced of a 2 % solution of Danish agar powder (Carl Roth GmbH & Co., Karlsruhe, Germany) in distilled water. The solution is heated on a heating and magnetic stirrer (160 °C) under continuous stirring until it becomes transparent and viscous. Subsequently, it is cast into the desired form, where it is cooled down to room temperature and solidifies.

Silicone

Silicone can easily be shaped into arbitrary 3D solids. It is stable for months and even years and insensitive to rough handling. It is non-toxic during preparation and application.

For the preparation of base material silicone, a two-compound silicone was used (Elastosil RT 601, Wacker-Chemie GmbH, Munich, Germany). Component A contains the platinum catalyst and component B (hardener) the cross-linker to build the silicone framework. Both components are mixed at a 9:1 (A:B) ratio of masses. The curing time depends on temperature, the higher the temperature, the shorter the curing time. Hence, to avoid fast curing, the silicone is filled into a pre-cooled mold. Small air bubbles, which occur in the silicone polymer during preparation, are eliminated by applying a reduced pressure to the silicone until it is free of visible bubbles. This procedure takes about 1 h.

Polyvinyl alcohol gel

Polyvinyl alcohol gel (PVA) is time-consuming in preparation due to the necessary granule dissolution and freezing cycles. It can easily be molded into solid forms. Kept under water close to freezing point, it can be stored for several months.

Granulated PVA, with a $99.0 - 99.8$ mol% degree of hydrolysis and an averaged

molecular weight of M_W = 145,000 (Fluka, Buchs SG, Switzerland), is used to prepare an aqueous solution.

Non-scattering PVA phantom

The non-scattering phantoms are prepared according to 'method II' of the publication by Kharine *et al.* [117] and [125]. 15 % PVA granulate are dissolved in dimethylsulfoxide (DMSO, Carl Roth GmbH & Co., Karlsruhe, Germany) and distilled water at a 80 : 20 ratio by weight . The solution is continously stirred while heating in an oil bath at a temperature of 140 °C for a duration of 2 h. Subsequently, the solution is filled into the mold. When cooled down for several hours at room temperature, the PVA is put into the freezer at −18 °C for 24 h. By freezing the PVA takes its solid form. The DMSO causes the crystallization of the PVA imparting the phantom the clear appearance. After freezing and following thawing the PVA is put into a bath of distilled water so that the DMSO can diffuse out of the phantom. For this procedure, the water is changed frequently. The preparation with DMSO has the advantage that the PVA phantom has a higher tensile strength especially at the 80 : 20 mass ratio compared to a phantom prepared by PVA only dissolved in water [125].

Scattering PVA phantom

According to 'method I' of the publication by Kharine *et al.* [117], a 20 % solution of PVA in distilled water is prepared. The solution is heated to 100 °C in an oil bath under continuous stirring. Filled into the form and cooled down, it is frozen at −18 °C for 12 h and afterwards thawed for 12 h. During freezing the PVA polymerizes and becomes solid and turbid. Kharine [117] and Devi [118] described that the turbidity and therewith the scattering coefficient increases with the number of freezing-thawing cycles. This characteristics is used to simulate scattering of tissue.

Polyacrylamide gel

Polyacrylamide (PAA) can be formed into arbitrary shapes, but it takes additional production steps to achieve a smooth and plain surface. During preparation, precaution is required, as PAA is performed by polymerization of the monomer acrylamide, which is known to be carcinogenic and neurotoxic. Polyacrylamide is

suspected to depolymerize to acrylamide under environmental conditions, such as heat and UV light (UV: ultraviolet) and it is discussed that PAA may contain a small amount of the monomer acrylamide after production [126]. In general, great care has to be taken during preparation and handling of PAA.

A 10 % PAA gel is prepared from a 40 % solution of acrylamide:bisacrylamide (29 : 1, *Rotiphorese* Gel 40, Carl Roth GmbH & Co., Karlsruhe, Germany). For 10 ml of gel composition, 2.5 ml of the *Rotiphorese* Gel is mixed with 4.8 ml distilled water and 2.5 ml of a 1.5 M Tris/HCl buffer solution (pH 8.8). 4 μl *N, N, N', N'*-tetramethylethylendiamine (TEMED, 99 % p.A. for electrophoresis, Carl Roth GmbH & Co., Karlsruhe, Germany) and 100 μl 10 % ammonium peroxodisulfate (APS, Carl Roth GmbH & Co., Karlsruhe, Germany) are added to the mixture and stirred. The mixture is poured into a mold to cure at room temperature for about 45 min.

1.2. Absorbers

Silicone dyes

The silicone dyes Elastosil Farbpaste RAL 9010 white, RAL 3000 dark red, and RAL 2004 orange (Wacker-Chemie GmbH, Munich, Germany) are used to achieve the desired optical properties for silicone. Before the color pastes are added the silicone components A and B are mixed. For each dye, a concentration series is made starting with a stock solution of 60 mg/g concentration. Based on a first 1:100 dilution, there are dilution steps of 8:10, 6:10, 4:10 and 2:10. The final concentrations are shown in table III.1.

Table III.1.: Concentrations of color pastes and scatterer in silicone.

Concentrations (mg g^{-1})
0.6
0.48
0.36
0.24
0.12

Dyes

The dyes given below are all soluble in distilled water and are used together with agar and PVA phantoms.

- Indocyanine green (ICG), Product Number: 21980-100MG-F, Sigma-Aldrich, Steinheim, Germany
- Pelikan Tusche A Drawing Ink 17 Black (Ink), Pelikan, Hannover, Germany
- Remazol Rot RB (RR, Remarol Red RB), DyStar Textilfarben GmbH & Co., Frankfurt, Germany
- Remazol Türkisblau G (RT, Remazol Turquois), DyStar Textilfarben GmbH & Co., Frankfurt, Germany

2. Acoustic characterization

2.1. Acoustic property measurements

Acoustic velocity and attenuation coefficient

The acoustic properties of the different phantom base materials were determined by using the insertion technique [127]. This technique is a relative measurement method, which employs water as a reference to study the transmission of longitudinal ultrasonic waves through solid media. The experimental geometry is represented schematically in figure III.1. It mainly consists of an ultrasound source and a hydrophone as a detector. Figure III.2 depicts a typical signal of an ultrasound pulse transmitted through water without the sample, i.e., a reference signal, exemplarily correlated to a signal transmitted through silicone. Both signals were recorded using a 5-MHz transducer as signal source.

The unknown acoustic velocities in the samples are deduced from the temporal shift (Δt) between the pulse transit time with and without samples. The sound velocity (c_s) can be calculated as

$$c_s = \left(\frac{1}{c_w} - \frac{\Delta t}{\Delta x} \right)^{-1}, \tag{III.1}$$

knowing the speed of sound in water (c_w) and the thickness of the sample (Δx).

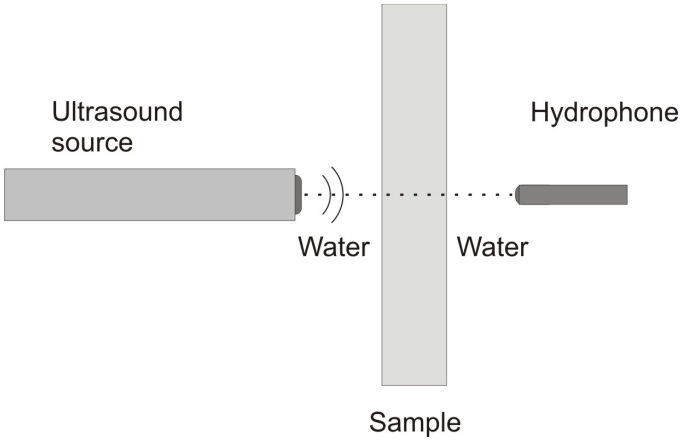

Figure III.1.: Experimental setup for the speed of sound (c_s) and acoustic attenuation (α_s) measurements.

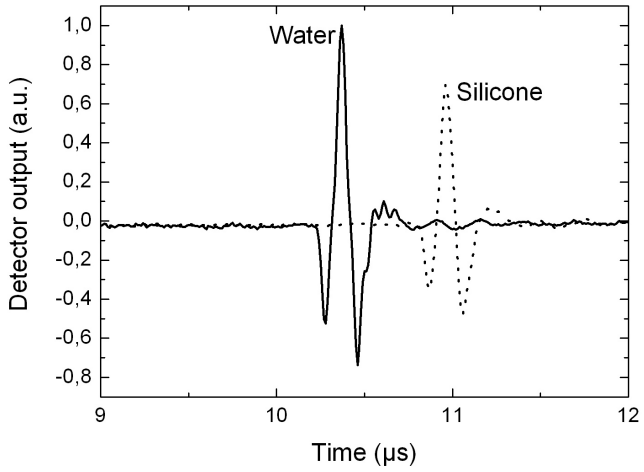

Figure III.2.: Typical ultrasound pulse shape in water without sample and behind a 2-mm silicone sample produced by a 5-MHz transducer

The attenuation coefficients (α_s) are measured by using the same experimental configuration and calculated according the following equation:

$$\alpha_s = \alpha_w - \frac{1}{\Delta x}\left[lnA_s - lnA_w - 2ln\left(1-R\right)\right], \tag{III.2}$$

where A_i is the amplitude of the received ultrasound pulse with the indices w and s representing water and the sample, respectively. The sample thickness is given by Δx, while R is the acoustical reflection coefficient at the water/sample

interface. For the transition of an acoustic wave from medium 1 to medium 2 with the impedances $z_{i=1,2}$, R follows the equation III.3:

$$R = \frac{z_2 - z_1}{z_2 + z_1}. \tag{III.3}$$

The impedances $z_{i=1,2}$ are those of water and the sample in the presented case. The impedance is given by

$$z = \rho_s c_s, \tag{III.4}$$

with ρ_s representing the density and c_s representing the acoustic velocity. Accordingly, R correlates with the acoustic velocity (c) and density (ρ) as well.

Table III.2.: Thickness of the silicone, agar, PVA, and PAA samples.

	Δx_1 (mm)	Δx_2 (mm)	Δx_3 (mm)
Silicone	2.0	4.0	6.0
Agar 2%	5.5	9.5	16.1
PVA	6.1	12.1	18.4
PAA	2.8	5.6	12.1

The acoustic properties were determined for the phantom materials silicone, agar 2% solution, PVA, and PAA. All materials were formed as rectangular blocks (80×80 mm^2) of three different thicknesses each. The dimensions are listed in table III.2. The measurements were performed in a water tank at room temperatur (25 °C). The detector was positioned at a distance of 74 mm to the source, while the sample, between them, was placed 20 mm behind the source. Two transducers (Subminiature Immersion probe H 5 M and H 10 M, GE Inspection Technologies, Ahrensburg, Germany) served as ultrasound sources with central frequencies of 5 MHz and 10 MHz respectively and outer diameters of 5 mm. The detector

was a PVDF needle hydrophone (MH28-5, FORCE Technology, Brondby, Denmark)(PVDF, polyvinylidenfluoride). A pulse generator (33250A, Agilent Technologies, Santa Clara, USA) was used for the excitation of the ultrasound pulses (five cycles) by a pulsed voltage of ±5 V. The pressure waves detected by the hydrophone were monitored with a digital storage oszilloscope (54641D, Agilent Technologies). To store the recorded data, they were transferred to a personal computer via the GPIB interface.

The results for each material were obtained by averaging 20 measurements per sample and by calculating the mean of the results of the three thicknesses with respect to a thickness of 1 cm. Errors were calculated based on the error propagation of the errors from the 20 averaged measurements, the three averaged thicknesses and that of the thickness measurements itself.

Density and impedance

The density values of the phantom materials were measured by the mass of three cubes with defined volumes for each material. According to equation III.4, the acoustic impedances can be calculated knowing the densities and the acoustic velocities of the phantom materials.

2.2. Results of the acoustic characterization

The acoustic attenuations were achieved using equation III.2 and 8.686 as the conversion factor from cm^{-1} to dB cm^{-1} [124]. To determine the absolute value for each sample, the attenuation coefficient of water, $\alpha_w = 2.5 \times 10^{-4} f^2$ [128, 129] was used, where the attenuation coefficient is given in cm^{-1} and the frequency f in MHz. For water, the acoustic attenuation coefficient increases proportionally to the squared frequency. The measured data for the different samples are presented in figure III.3 a) - d). In the frequency range from 4 to 14 MHz, the frequency-dependent attenuation coefficients are $\alpha = 6.06 f^{0.49}$ dB cm^{-1} MHz^{-1} for silicone, $\alpha = 0.15 f^{1.15}$ dB cm^{-1} MHz^{-1} for PAA and $\alpha = 0.16 f^{0.65}$ dB cm^{-1} MHz^{-1} for agar. Over the frequency range, no reasonable fitting according to the frequency power law was possible for PVA. The resulting errors were mainly caused by the fluctuations of the results of the measurements at three different thicknesses that were normalized to unit length.

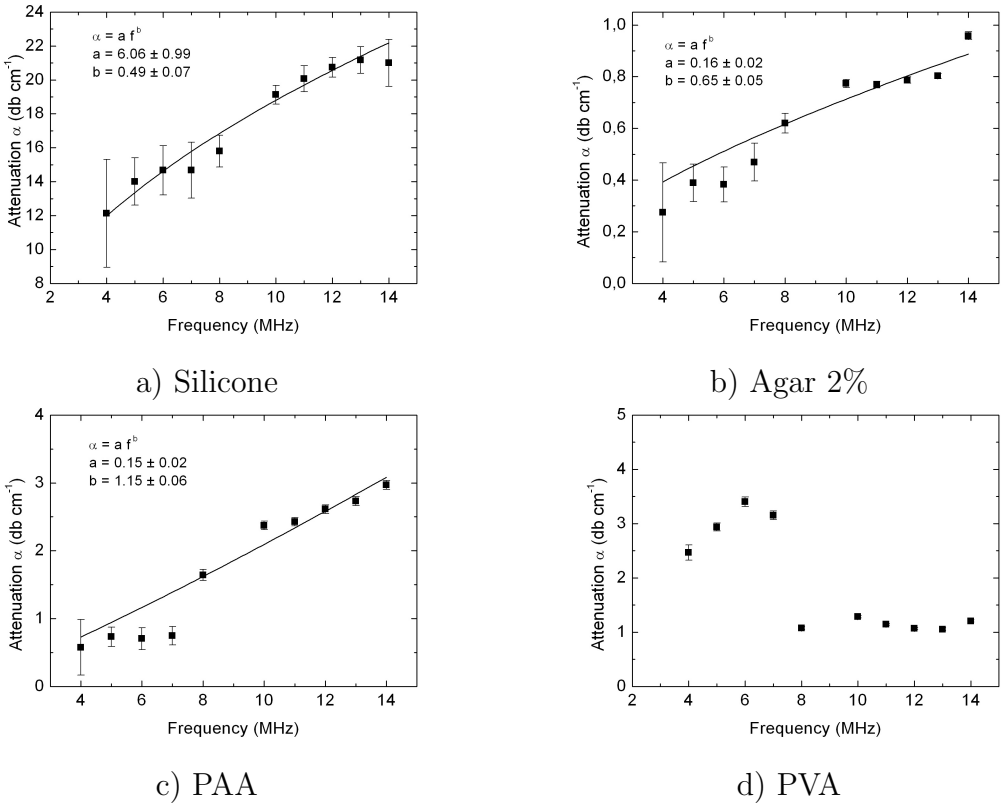

Figure III.3.: Acoustic attenuation coefficients as a function of frequency in a range from 4 MHz to 14 MHz of a) silicone, b) agar 2%, c) PAA and d) PVA.

The acoustic velocities were calculated according to equation III.1, assuming a speed of sound in water of 1482.3 m s^{-1} [130]. Knowing the acoustic velocity and the measured density, the impedance was calculated. Sound velocities and acoustic impedances show, within experimental uncertainties, a vastly linear and constant frequency dependence. In table III.3, the acoustic velocities, the impedances and densities as well as some results of the acoustic attenuation experiments are summarized and compared to literature data of phantom materials and human tissue. Only those results, measured in the frequency ranges similar to the cited literature data were selected.

Agar possesses acoustic velocity, impedance, and density similar to human tissue. The acoustic attenuation coefficient at the measured frequency is lower than that of breast tissue and skin. The results for the acoustic velocity are confirmed by the results of Browne *et al.* [131]. The acoustic velocity and impedance of silicone are lower than those of human tissue, but it has a density similar to human tissue.

Its acoustical attenuation lies between the values of breast tissue and that of skin within the frequency range investigated. The acoustic velocity, impedance, and density found for PVA are comparable to those of human tissue and similar to those found in literature [117]. Only the acoustic attenuation determined in the experiments is lower than that of breast tissue. Our measured acoustical properties and a density value for PAA are similar to those of human breast tissue and skin. However, the acoustic attenuation of PAA is too low to simulate these types of human tissues. These findings are in good agreement with the results of Prokop *et al* [132].

Table III.3.: Sound velocities, densities, impedances, and acoustic attenuation coefficients of silicone, agar, PVA, PAA in comparison to the values of human tissues and literature values.

Material	Velocity, c_S (10^3 m s^{-1})	Density, ρ (10^3 kg m^{-3})	Impedance, z (10^6 kg m^{-2} s^{-1})	Acoustic attenuation coefficient, α (dB cm^{-1})	Frequency (MHz)	References
Human						
breast tissue	$1.43 - 1.57$	$0.99 - 1.06$	$1.42 - 1.66^b$	$9.5 - 12.6$	7	[130]
Human skin	1.54^a	$1.11 - 1.19$	$1.71 - 1.83^b$	9.2 ± 2.2	5	[130]
Silicone	1.03 ± 0.06^c	1.07 ± 0.03	1.10 ± 0.05^c	14.0 ± 1.4	5	experiment
	-	-	-	14.7 ± 1.6	7	
PVA	1.57 ± 0.02^c	1.10 ± 0.05	1.74 ± 0.08^c	2.9 ± 0.1	5	experiment
	-	-	-	3.2 ± 0.1	7	
	1.58 ± 0.03	1.07 ± 0.05	1.71 ± 0.06	2.1	5	[117]
PAA (10%)	1.58 ± 0.05^c	1.09 ± 0.09	1.73 ± 0.08^c	0.7 ± 0.1	5	experiment
	-	-	-	0.7 ± 0.1	7	
	-	1.02 ± 0.01	-	0.4 ± 0.1	5	[132]
Agar (2%)	1.50 ± 0.03^c	1.04 ± 0.11	1.57 ± 0.08^c	0.4 ± 0.1	5	experiment
	-	-	-	0.5 ± 0.1	7	
	1.54	-	-	-	-	[131]

[a] Fetal, 7 mo.
[b] Calculated from columns 1 and 2.
[c] Measured at 7 MHz.

3. Optical characterization

The optical properties relevant for this work are the scattering coefficient μ_s and absorption coefficient μ_a. These properties are not direct accessible, but there are different ways for determination.

3.1. Spectroscopical measurements

Integrating sphere measurements

One method to obtain optical properties, described in literature, is a non-iterative indirect method based on a combination of diffuse transmission (T_d) and reflection (R_d) measurements and the Kubelka-Munk coefficients (S_{KM} and A_{KM}) [133]. The correlation is given in mathematical form by the following equations:

$$S_{KM} = \frac{1}{yt} ln \left[\frac{1 - R_d \left(x - y \right)}{T_d} \right] \tag{III.5}$$

$$A_{KM} = \left(x - 1 \right) S_{KM} \tag{III.6}$$

$$x = \frac{1 + R_d^2 - T_d^2}{2R_d} \quad ; \quad y = + \sqrt{x^2 - 1} \ . \tag{III.7}$$

The dependence of the Kubelka-Munk coefficients on the absorption coefficient and the reduced scattering coefficient $\mu_s^{'}$ is given by [134] as

$$A_{KM} = 2\mu_a \tag{III.8}$$

$$S_{KM} = \frac{1}{4} \left\{ 3\mu_s^{'} - \mu_a \right\} \ . \tag{III.9}$$

The scattering and reduced scattering coefficient are related over the anisotropy factor g by

$$\mu_s^{'} = \mu_s \left(1 - g\right) \quad . \tag{III.10}$$

Combining the equations III.5 to III.9, the final absorption and reduced scattering coefficients can be calculated by the following equations

$$\mu_a = \frac{1}{2} \left(x - 1\right) S_{KM} \tag{III.11}$$

$$\mu_s^{'} = \frac{1}{6} \left(7 + x\right) S_{KM} \quad . \tag{III.12}$$

The scattering coefficient cannot be determined directly by these measurements. A correlation between the scattering coefficient and the collimated transmission T_c is given by Beer's law

$$\mu_t = \mu_a + \mu_s = -\frac{lnT_c}{t} \quad , \tag{III.13}$$

where μ_t is the attenuation coefficient. With knowledge of μ_a and T_c , μ_s can be calculated. In case that only diffuse T_d and total T_t transmission are measurable, T_c can be derived by

$$T_c = T_t - T_d \quad . \tag{III.14}$$

In addition, knowing $\mu_s^{'}$ and μ_s, the anisotropy factor can be calculated according to equation III.10.

This method was used only for the characterization of the silicone dyes. To measure the absorption and scattering coefficients, the diffuse reflectance and transmittance and the total transmittance of the samples were measured using an integrating

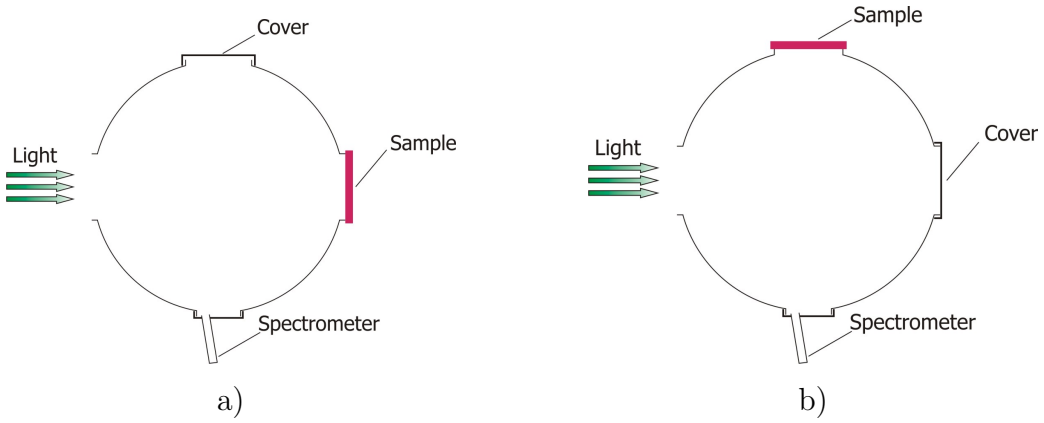

Figure III.4.: a) Diffuse reflection measurement; b) reference measurement for diffuse reflection.

sphere. The samples were illuminated by collimated light. The 2 mm thick slides were placed behind the sphere for the reflection measurement (see figure III.4a))

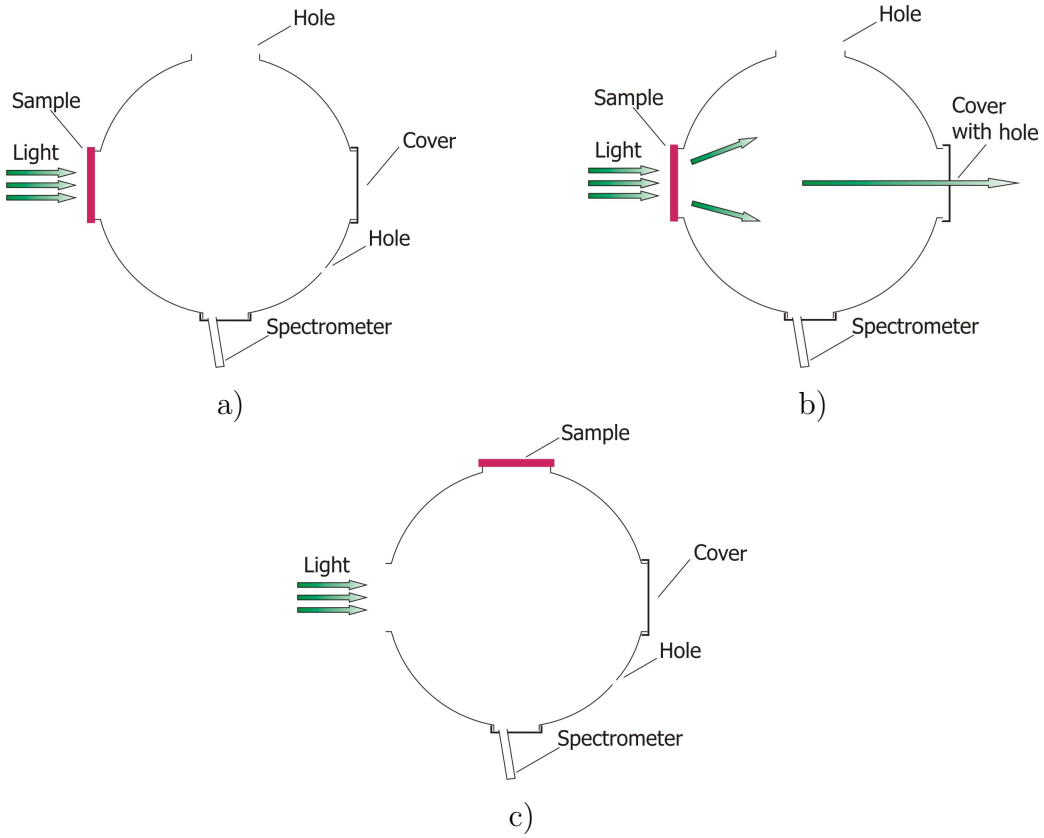

Figure III.5.: a) Total transmission measurement; b) diffuse transmission measurement; c) reference measurement for transmission measurements.

and in front of the sphere for the transmission measurements (see figure III.5a) and b)). In these measurements, only the light intensity I is measurable. Hence, reference measurements were taken to obtain I_0 and therewith the reflectance or transmittance by placing the samples beside the sphere as shown in figures III.4b) and III.5c). In both, the measurement and the corresponding reference measurement, an even amount of openings and similar surface conditions in the interior of the sphere were chosen to generate comparable conditions. Due to the experimental setup one reference measurement is required for the reflectance measurement and only one for both transmission measurements. A reference measurement was taken for every sample. The detector was placed to face one of the interior surfaces of the sphere to keep the detection conditions stable.

A white light lamp (KARL STORZ GmbH & Co. KG , Tuttlingen, Germany) served as light source for the collimated illumination. For the detection of the diffuse light in the sphere a fiber optic spectrometer was used (S2000, Ocean Optics Inc., Dunedin, Florida, USA). An average over 30 spectra was taken for each measurement.

UV-Vis spectrometer measurements

Another way to determine optical properties is the UV-Vis spectroscopy. With the spectrometer (Beckman DU 600) the extinction was measured, which is given as [135]

$$E = log\frac{I}{I_0} = \epsilon \cdot c \cdot d \tag{III.15}$$

where ϵ is the decadal molar extinction coefficient, c the concentration and d the sample thickness. The extinction coefficient μ_t can be obtained by multiplying ϵ with 2.202. According to equation III.13, μ_t is the sum of absorption and scattering coefficient. Hence, the absorption and scattering coefficients can only be separated if the sample is purely scattering or absorbing.

Photoacoustic measurements

One method to directly access the absorption coefficient is photoacoustic spectroscopy.

A scheme of the experimental setup is depicted in figure III.6. The photoacoustic sensor has been described in detail in [136]. The sample is put on top of a prism. A fiber is connected at the side of the prism with a convex lens in front to collimate the laser light. The collimated laser beam is guided to the upper surface of the prism to illuminate the probe. The induced ultrasound waves are detected piezo electrically in backward mode at the reverse side of the prism. The piezo foil converts the pressure wave into a voltage signal which becomes amplified by a voltage amplifier and is led via BNC to an oscilloscope and a computer for recording.

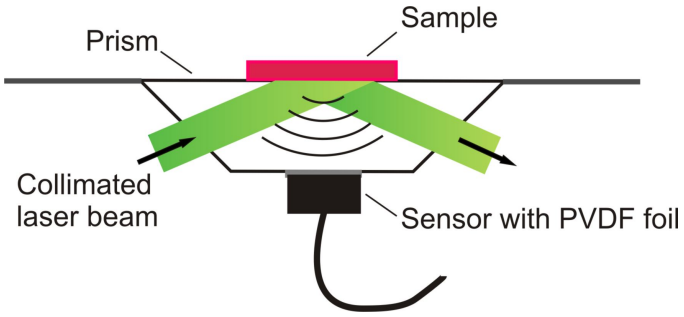

Figure III.6.: Schematic of the photoacoustic measurements on top of a prism.

To determine an unknown absorption coefficient, the photoacoustic signals of a concentration series of a sample with known absorption coefficients have to be measured. Since the photoacoustic signal depends on the energy of the laser beam, the energy has to be monitored and the signal amplitudes have to be divided through their corresponding energy. With the results of concentration series, a calibration curve can be determined by plotting the energy-corrected photoacoustic signals against the known absorption coefficients. The absorption coefficient of the unknown sample is now obtained by using the calibration curve and the measured and energy corrected photoacoustic signal of this sample.

3.2. Results of the optical characterization

To test the capability of the OPUS system for quantitative analytical measurements, phantoms with well defined absorption characteristics are required. In the following section, the results of the optical characterization of the dyes used for Phantoms are presented.

Indocyanine Green

Indocyanine green (ICG) is a fluorescence dye. Hence, the absorbed energy transforms only partially into a pressure wave, while the rest of the energy leads to photon emission in form of fluorescence light. The fluorescence absorption and emission spectra of a 1-mg-L^{-1} solution of ICG, taken by the luminescence spectrometer LS50 (Perkin Elmer, Beaconsfield, Buckinghamshire, GB), are shown in figure III.7.

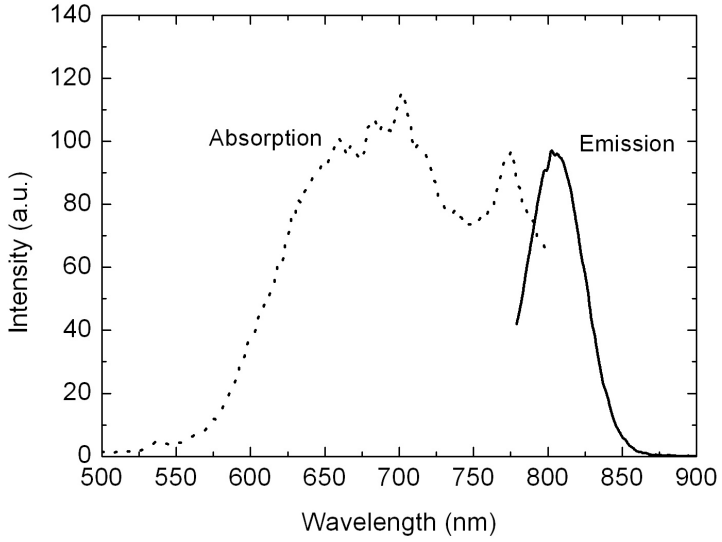

Figure III.7.: Fluorscence absorption and emission spectra of a 1-mg-L^{-1} ICG solution.

To characterize ICG by UV-Vis spectroscopy, a stock solution with a concentration of 100 mg L^{-1} was prepared. Based on this stock solution, a concentration series with concentrations between 0.1 mg L^{-1} and 10 mg L^{-1} was prepared and measured contemporary. The UV-Vis spectra are depicted in figure III.8 a). The spectra show two maxima, one at 715 nm and another at 780 nm. The calibration curve at 780 nm is given in figure III.8 b).

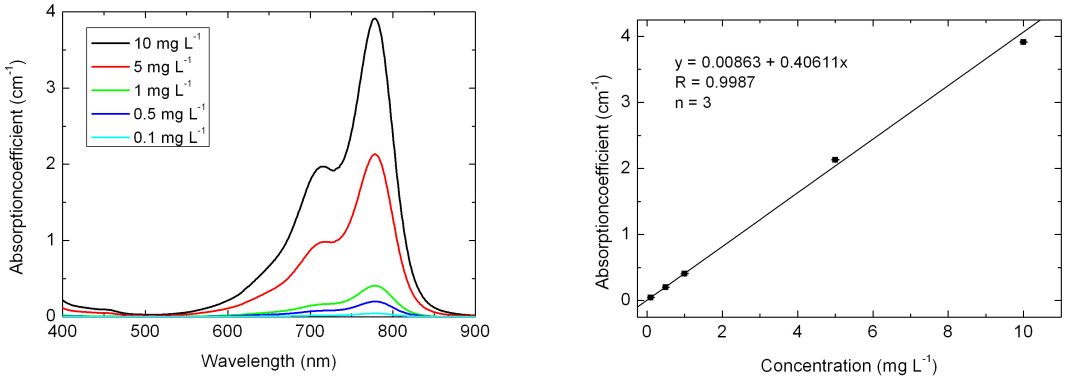

a) b)

Figure III.8.: a) UV-Vis spectra of a freshly produced ICG solution at different concentrations between 0.1 mg L^{-1} and 10 mg L^{-1}; b) calibration curve at 780 nm.

The stock solution was stored in the dark for seven days. After this period, a new concentration series with concentrations between 8 mg L^{-1} and 50 mg L^{-1} was prepared and measured. The spectra for this series and the corresponding calibration curve evaluated at 780 nm are shown in figure III.9 a) and b). A lower slope can be observed, although the stock solution was stored in the dark.

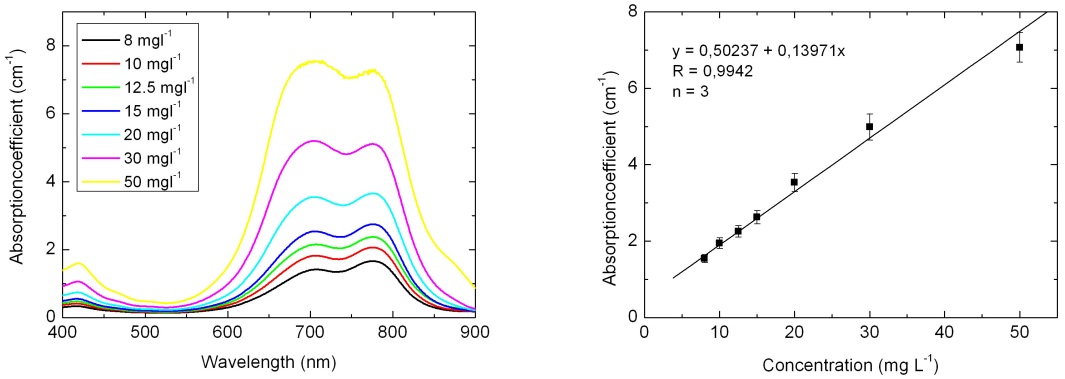

a) b)

Figure III.9.: a) UV-Vis spectra of a seven days old ICG solution at different concentrations between 8 mg L^{-1} and 50 mg L^{-1}; b) calibration curve at 780 nm.

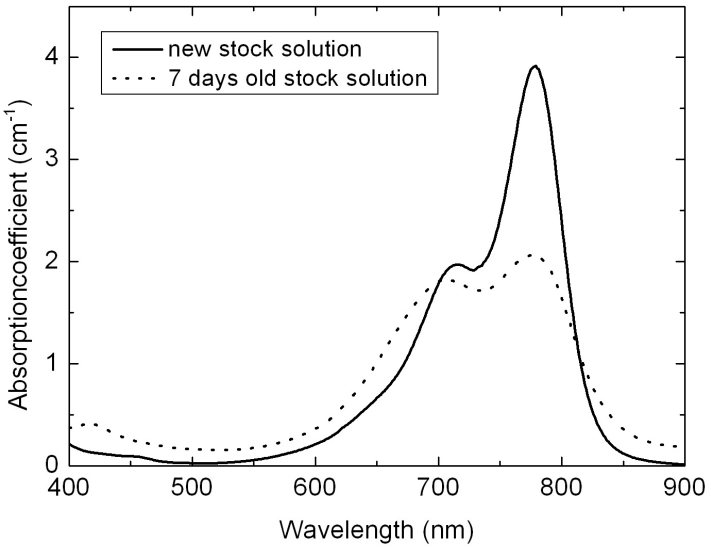

Figure III.10.: UV-Vis spectra of two ICG solutions (10 mg L^{-1}). One prepared from a new stock solution, the other prepared seven days later from the same stock solution.

The 10-mg-L^{-1} solutions of the two concentration series are contrasted with each other in figure III.10. A 7,6%-reduction in the absorption coefficient at 715 nm and a reduction of 47.2% at 780 nm are observable for the solution prepared from the seven days old stock solution. The changes in the absorption coefficient is the result of aging processes.

Black Ink

The black ink was characterized by UV-Vis measurements. For this purpose, a concentration series was prepared with concentrations between 0.05 ml L^{-1} and 0.25 ml L^{-1} with 0.05-step width. Since ink is a colloidal suspension and the colloids cause scattering, only the extinction coefficient can be determined by UV-Vis spectroscopy. The spectra are illustrated in figure III.11. The ink absorbs over the whole measuring range from 400 nm to 900 nm.

Plotting the extinction coefficient against the concentration at 760 nm results in a calibration curve that can be seen in figure III.12.

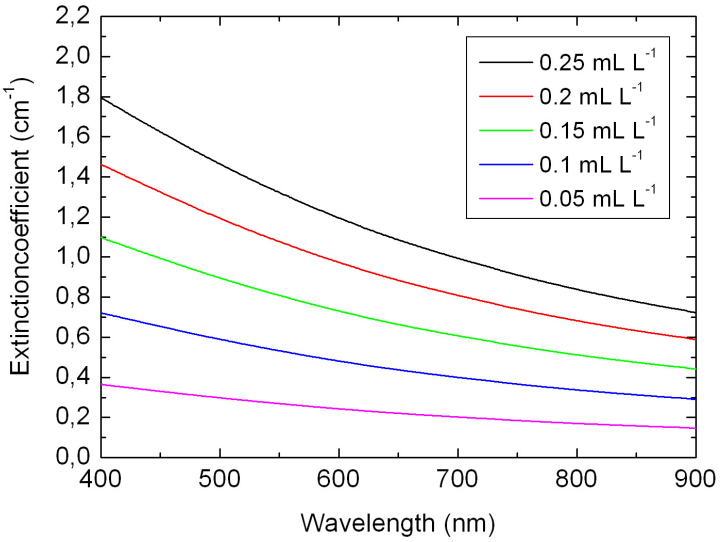

Figure III.11.: UV-Vis spectra of black ink solutions at different concentrations.

One undesired side effect of the colloidal consistence of the ink is the sedimentation of the colloids on the bottom of the container. Hence, prior to the measurement, the solution has to be shaken well or treated by ultrasonification.

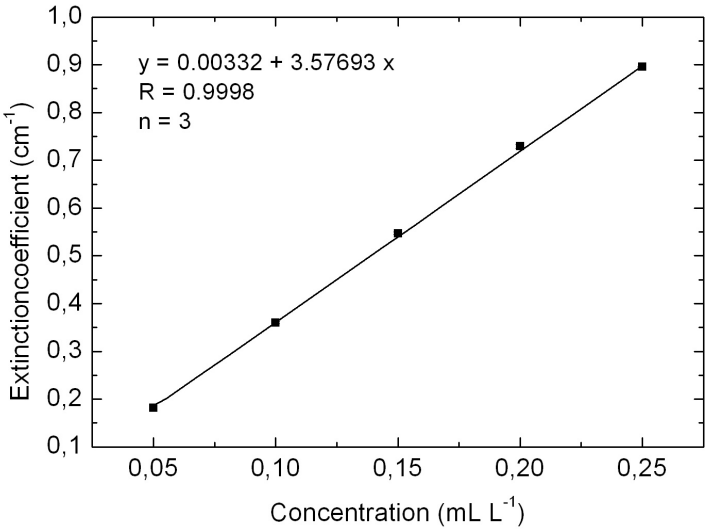

Figure III.12.: Calibration curve of black ink at 760 nm.

Remazol Turquois

A spectrum of a 10-mg-L^{-1} Remazol Turquois solution, taken by UV-Vis spectrometer, is shown in figure III.13. The dye has two maxima, a larger one at 667 nm and a smaller one at 628 nm.

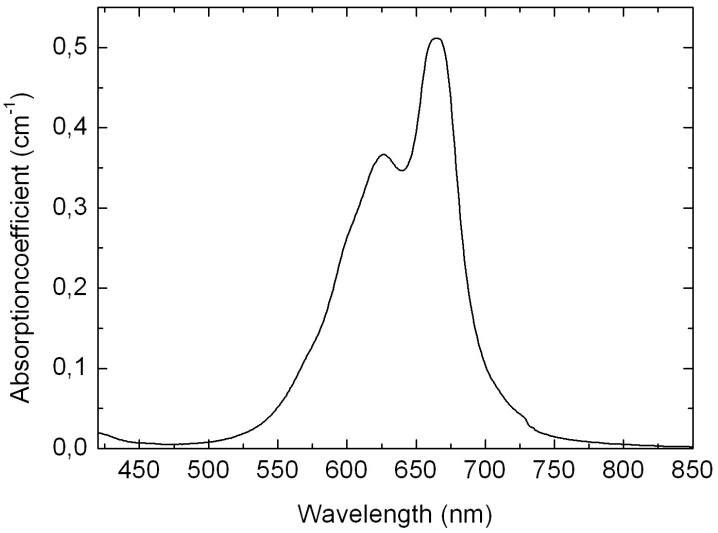

Figure III.13.: UV-Vis spectrum of a 10-mg-L^{-1} Remazol Turquois solution.

Remazol Red

The UV-Vis spectrum of a 7.5-mg-L^{-1} solution of Remazol Red is shown in figure III.14. Remazol Red has an absorption maximum at 521 nm. It is, as ICG and Remazol Turquois, a non colloidal dye, thus, the plotted values are the real absorption coefficient.

Since the real absorption coefficients of Remazol Red can be determined by UV-Vis spectroscopy and its absorption maximum lies near the working wavelength of the frequency doubled Nd:YAG laser (532 nm) of the photoacoustic setup (see section 3.1), Remazol Red is used as a reference dye for the PA measurements. A typical photoacoustic signal of Remazol Red is depicted in figure III.15. The signal was taken for a 1-mg-L^{-1} solution with a laser energy of 0.68 mJ. The photoacoustic signal at position 1 (0 μs) is caused by radiation which becomes reflected at the

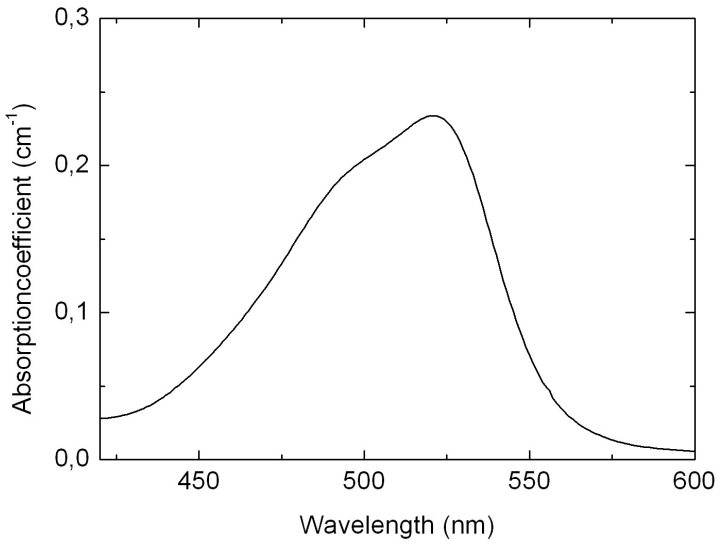

Figure III.14.: UV-Vis spectrum of a 7.5-mg-L^{-1} Remazol Red solution.

sensor surface and partially illuminates the lower electrode layer of the detector. Peak 2 is the photoacoustic signal of the Remazol Red solution on top of the prism. To use Remazol Red as reference for further photoacoustic measurements, a calibration curve was taken for the UV-Vis measurements as well as for the photoacoustic

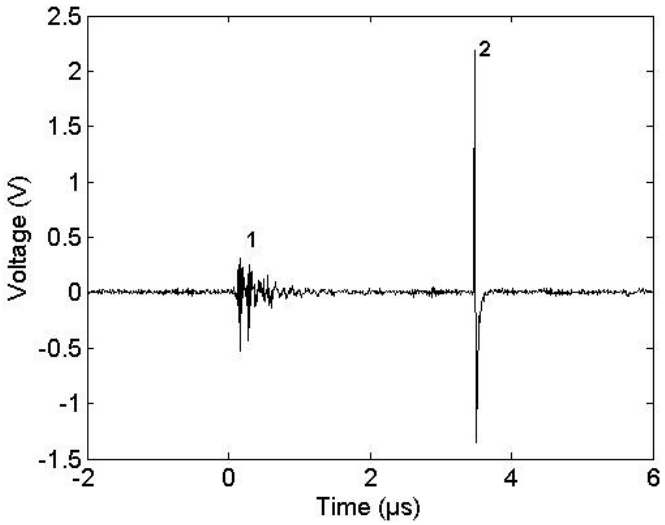

Figure III.15.: Photoacoustic signal of a 1-mg-L^{-1} solution of Remazol Red (Laser energy 0.677 mJ).

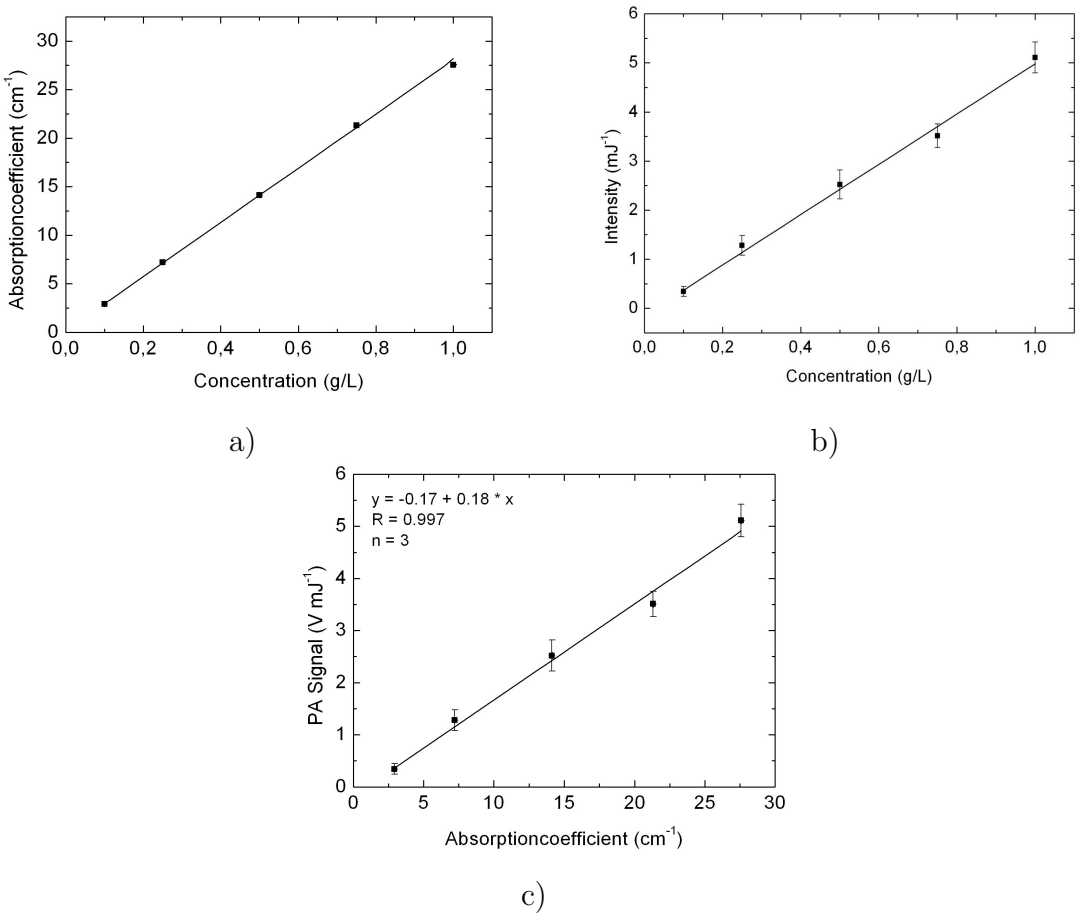

Figure III.16.: Calibration curves for Remazol Red at 532 nm measured with a) UV-Vis and b) photoacoustic spectroscopy. c) Photoacoustic versus UV-Vis measurements of Remazol Red at 532 nm.

measurements. Due to laser energy fluctuations, the photoacoustic signal must be normalized to the energy. The calibration measurements were performed for concentrations between 0.1 g L^{-1} and 1 g L^{-1}. The resulting calibration curves are illustrated in figure III.16 a) and b). In figure III.16 c) the photoacoustic signals measured in V mJ^{-1} are plotted against corresponding absorption coefficients which leads to a linear correlation given by the equation as shown in the graphic. This equation is the basis to calculate the absorption coefficients of partially scattering samples by measuring their PA signal and the corresponding energy.

Silicone Dyes

Results of the integrating sphere measurements

The silicone dyes white (RAL 9010), red (RAL 3000), and orange (RAL 2004) were first characterized via the integrating sphere measurements. To obtain the absolute values for absorption and scattering of the dyes and scatter paste, a blank value had to be measured. Figure III.17a) shows a typical result for total transmission and reflection for clear silicone. As expected, there is only low reflection of about 3 - 4 % and high transmission in a range from 90 % to 95 % over the measured wavelength range. This means that the 2 mm thick silicone alone absorbs 1 - 7 % of the incoming light.

Typical transmission and reflection spectra of the white and red silicone dye (each at a concentration of 0.48 mg g^{-1}), with that of clear silicone already subtracted, are presented for a selected concentration in figures III.17b) and c). The white sample has a higher reflectivity than silicone, which means, that the sample has a strong scattering behavior. The reflection and transmission are nearly constant over the measured wavelength range. The sum of the reflection and transmission results in a constant absorption over the whole wavelength range of 8 %. The spectra of the red dye show a transmission minimum between 480 nm and 575 nm, while the reflection is constant and low. This wavelength range can be identified as the range of highest absorption. For larger wavelengths, the transmission as well as the reflection is increasing leading to the suggestion, that the red dye is additionaly scattering.

In figure III.18, the absorption and scattering coefficient for the red dye at a concentration of 0.48 mg g^{-1} are compared with each other. As discussed before, the dye shows an obvious scattering behavior with a maximum at around 610 nm, where the absorption is minimal. The scattering is caused by pigments within the dye appearing as small particles with a few hundred nanometers and aggregates of these particles in the size of some tenth of micrometers. These particles and aggregates could be observed with an inverse fluorescence microscope (Olympus IX 70). The absorption has maxima at 500 nm and 550 nm. Comparing the absorption coefficient over the wavelength range for different concentrations (see figure III.19), it can be seen, that at lower concentrations, there is no distinction possible between the two maxima. Furthermore, the absorption decreases stronger for larger wavelengths at higher dye concentration.

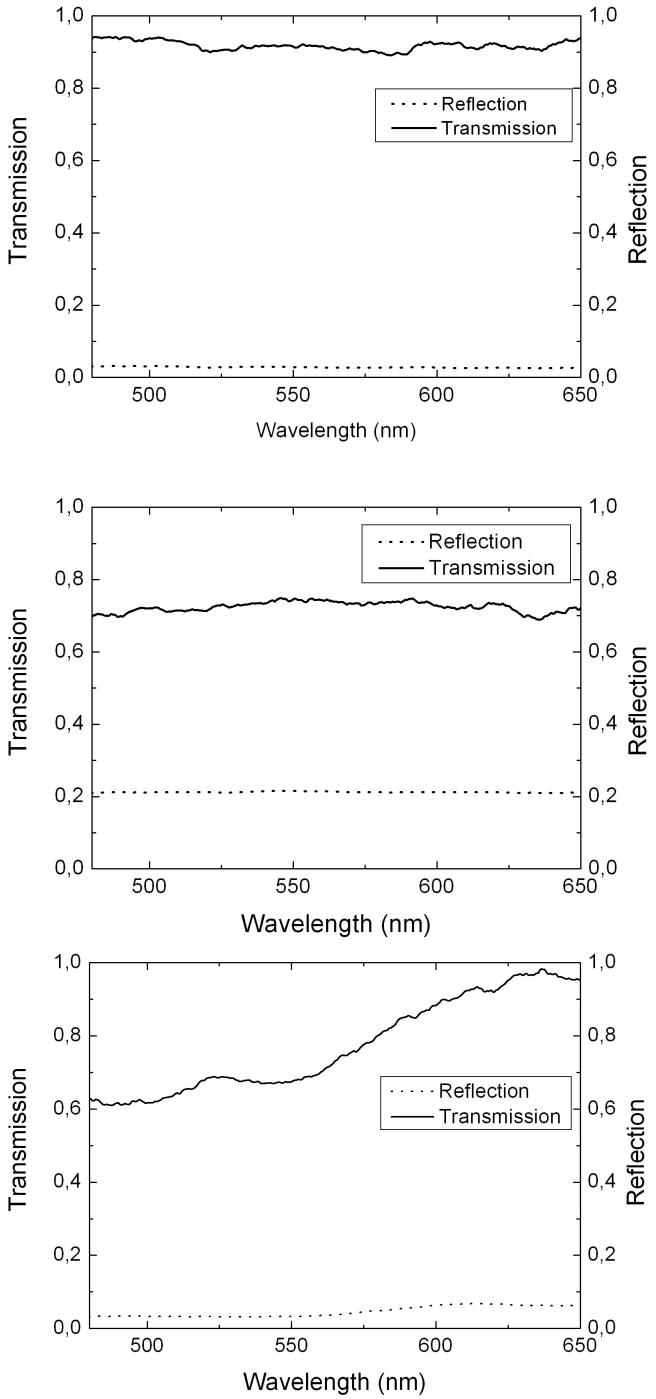

Figure III.17.: Transmission and reflection spectra of clear silicone (top), white (0.48 mg/g) (middle), and red 1(0.48 mg/g) (bottom).

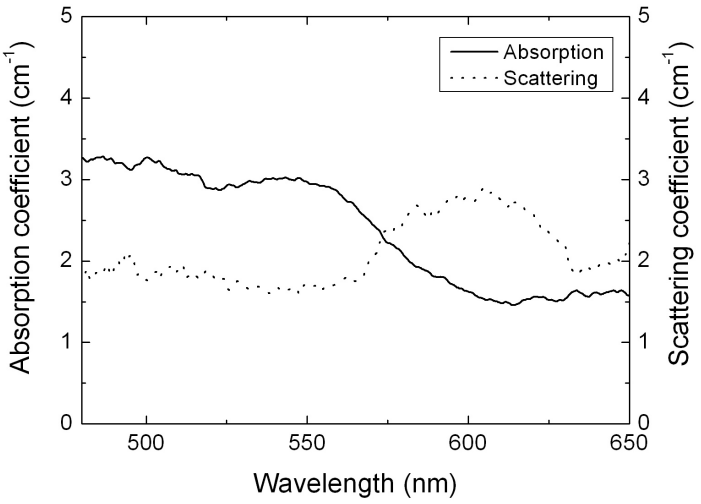

Figure III.18.: Absorption and scattering coefficient versus wavelength for the red dye (0.48 mg/g).

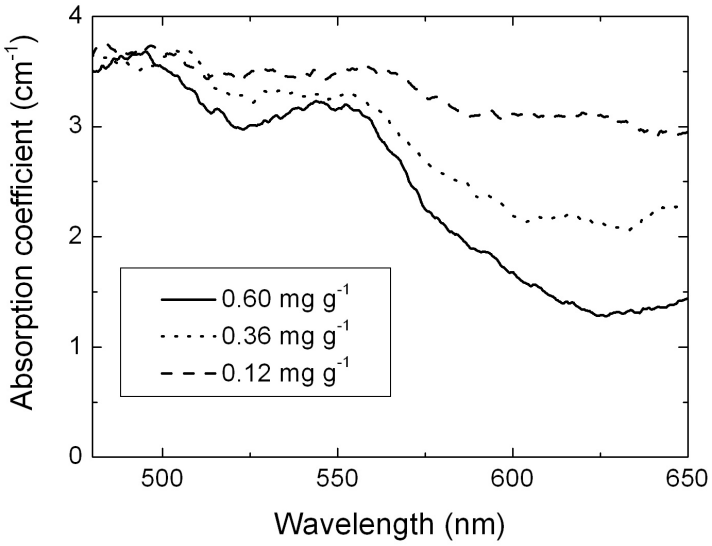

Figure III.19.: Wavelength dependent absorption coefficient for the red dye at three different concentrations.

The scattering and absorption coefficients for two concentration series of the red dye (red 1 and red 2) were plotted against the concentrations for the two wavelengths 550 nm and 620 nm. Both series were prepared at once, but stored differently. The series red 2 was illuminated for one week by sun light. The results are illustrated in figure III.20. At 550 nm, which is the absorption maximum, the absorption coefficient varies only slightly with concentration, while the scattering coefficient is

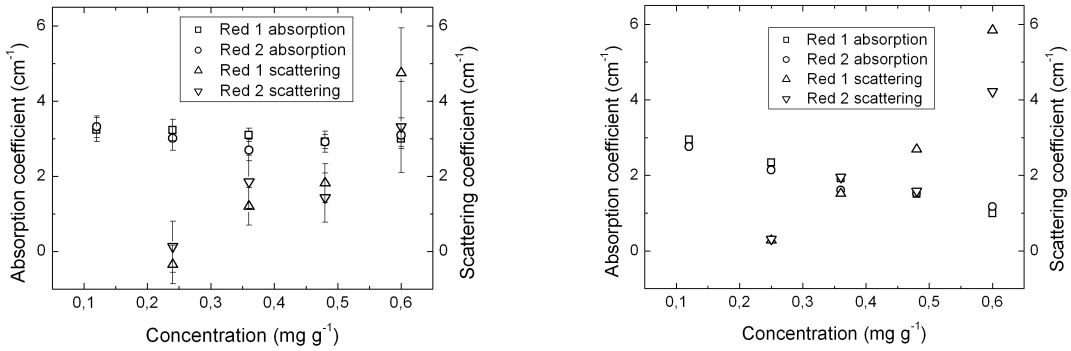

Figure III.20.: Absorption and scattering coefficient versus concentration for red 1 and red 2 at a) 550 nm and b) 620 nm.

rising with increasing concentration. The same trend for the scattering coefficient can be observed at 620 nm. The absorption coefficient at 620 nm is decreasing with increasing concentration. Both charges give similar results within the error range, which means, that the illumination by daylight has no obvious effect on the optical parameters for short time periods.

In the orange dye, particles and aggregates could be observed with the microscope as well. Figure III.21 shows the wavelength dependent absorption and scattering

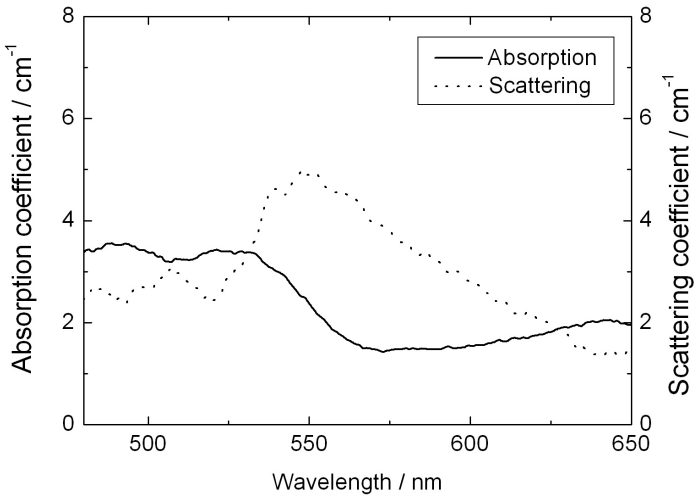

Figure III.21.: Wavelength dependent absorption and scattering coefficient for the orange dye (0.48 mg/g).

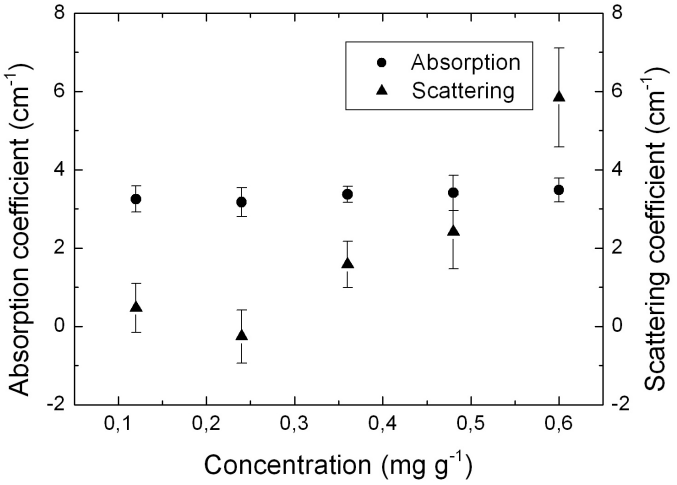

Figure III.22.: Absorption and scattering coefficient versus concentration for the orange dye at 520 nm.

coefficient for a concentration of 0.48 mg g^{-1}. The absorption is highest in a range from 480 nm to 530 nm. The maximum of the scattering coefficient is at 650 nm. The behavior of the absorption and scattering coefficient in dependence on the dye concentration for a fixed wavelength is similar to that of the red dye. It is illustrated in figure III.22 for 520 nm.

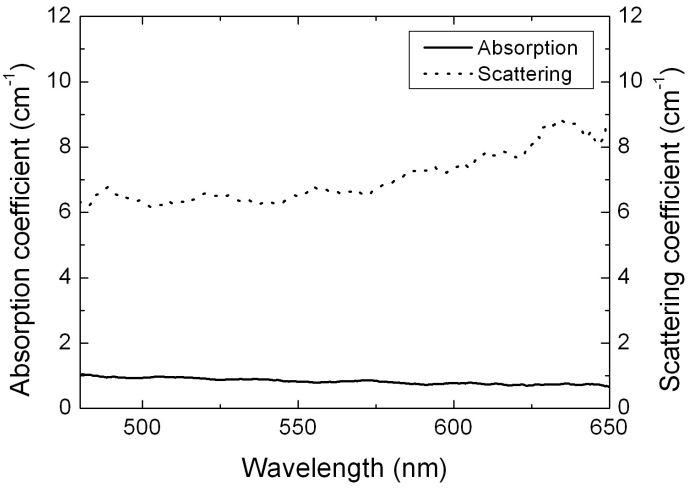

Figure III.23.: Wavelength dependent absorption and scattering coefficient for the white dye (0.48 mg/g).

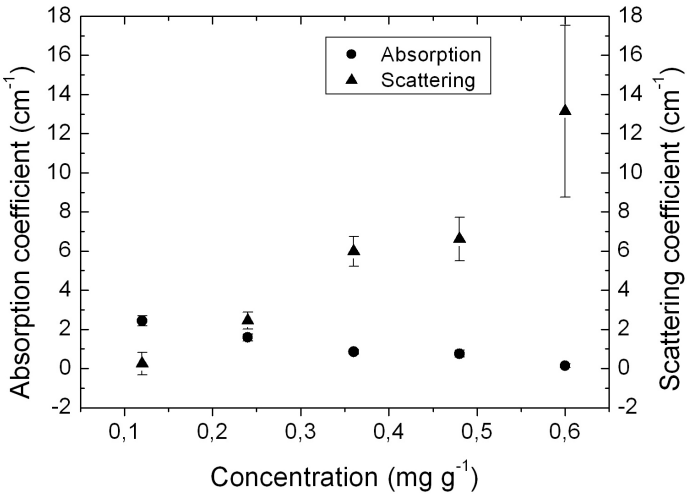

Figure III.24.: Absorption and scattering coefficient versus concentration for the white dye at 550 nm.

The white dye, consisting mainly of TiO_2, has a different behavior than the red and orange dye. The absorption coefficient is nearly constant over the measured wavelength range, while the scattering coefficient is increasing for higher wavelengths. The diagram for one exemplary concentration of 0.48 mg g^{-1} is presented in figure III.23. Looking at the concentration dependency of the coefficients at a wavelength of 550 nm (see figure III.24), the absorption coefficient shows a similar behavior as the red and orange dye. Mimicking the scattering coefficient of human breast tissue which is $\mu_s = 395$ cm^{-1} at 635 nm (see [133] with references therein) the absorption coefficient would become negligibly small for the corresponding concentration.

Results of the UV-Vis measurements

In addition to the integrating sphere measurements, the concentration series red 1 was also examined by UV-Vis spectroscopy to measure the attenuation coefficient. The spectra for the single concentrations are shown in figure III.25. These spectra support the results of the integrating sphere measurements. The absorption maxima are observable within the same wavelength range. A scattering behavior can also be observed by this method. If the dye only or mainly absorbs, the spectra would show an increase only in the absorption peak and not over the whole

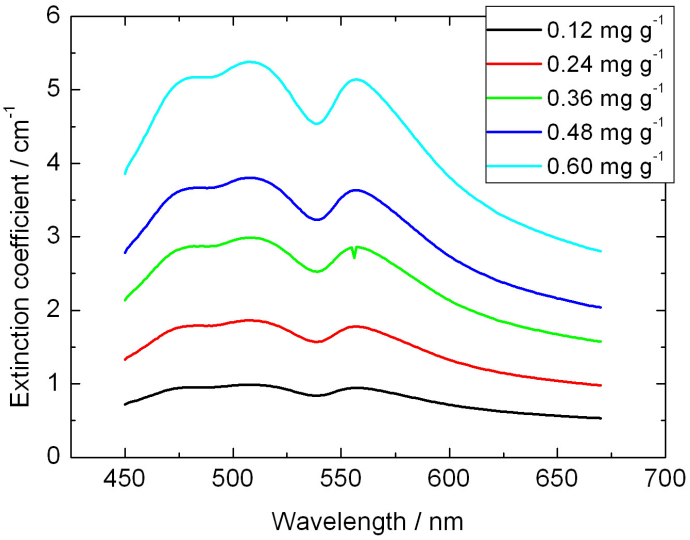

Figure III.25.: UV-Vis spectrum for the concentration series red 1.

measured wavelength range, which is the case with this dye. The absorption and scattering coefficient cannot be separated from these measurements. Hence, no statement can be made over the exact absorbing and scattering behavior of the dye, nor can it be proved, whether the absorption coefficient is really decreasing with increasing concentration or not.

Results of the photoacoustic measurements

Since it is unlikely, that the absorption coefficient is descending with increasing dye concentration, the way of determining the coefficient from the integrating sphere measurements has to be verified with respect to the suitability. Therefore, the absorption coefficient for the red dye was studied by photoacoustic measurements. The complete concentration series red 1 was tested at 532 nm. The coefficients has been calculated based on the reference measurements from Remazol Red. The resulting graph is illustrated in figure III.26. With these measurements it has been shown that the absorption coefficient as expected is increasing with increasing dye concentration. Accordingly, the integrating sphere measurement with the presented method determining the absorption coefficient is inappropriate.

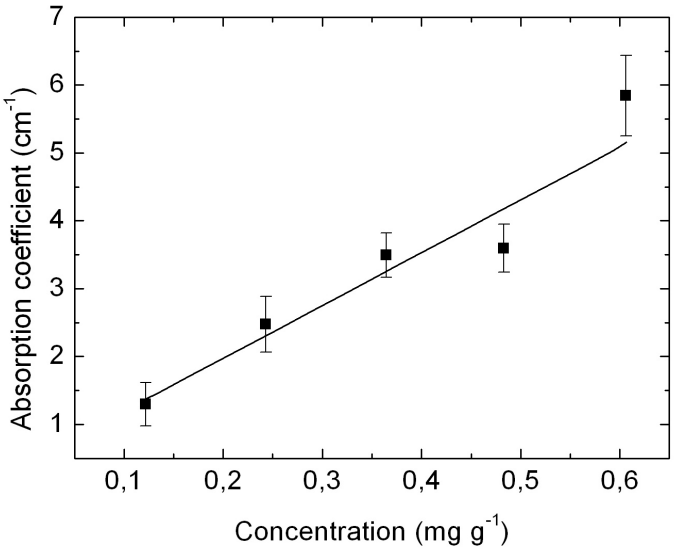

Figure III.26.: Photoacoustic measurement for red 1 at certain concentrations.

4. Discussion

The acoustic characterization shows that all investigated materials are suitable for tissue-mimicking phantoms under different conditions. The choice of the material depends mostly on the part of the human body to be simulated, on the frequency range of the ultrasound scanner and on the practical handling considerations. The part of the human body of interest in the present work is the breast.

PVA fits very well to simulate breast tissue regarding the acoustic properties especially up to 10 MHz. In particular, the sound velocity matches best. The scattering coefficient can be easily adjusted by a specific preparation method with a defined number of freezing-thawing cycles. PVA can be used with the water soluble dyes presented in the work. It has the disadvantage, that the preparation procedure is rather time-consuming. Furthermore, if the dyes are used without separating them from PVA by a barrier material, they diffuse into the PVA.

The acoustic properties of agar are satisfactory, but not stable over days and weeks, therefore, it is not suitable for repeated applications. But Agar is quick and easily fabricated, thus, there is no necessity for long-term stability. Agar also works with water soluble dyes, but with the same disadvantage as for PVA.

Although PAA is well suited with respect to its acoustic properties, it seems to be

less appropriate for phantom preparation, due to its potential toxicity, especially during preparation.

The main advantages of silicone are its long-term stability and robustness. Hence, it is a suitable material for stable phantoms, particularly for training, although its acoustical properties do not fit perfectly. Furthermore, the dyes do not diffuse into the material.

Compared to the phantom materials, the dyes are suitable to mimic the optical properties of tissue depending on the used laser wavelength of the equipment and their texture.

ICG is a water soluble fluorescence dye, that is able to mimic the absorption of blood within the wavelength working range of the OPUS system, since it possesses an absorption maximum in this range. Due to aging processes, it is necessary to produce fresh solutions before every experiment to gain reproducibility. Another problem lies in its fluorescence character. To correlate the photoacoustic signal with the corresponding part of the absorbed energy, it is necessary to know, which quantity of the absorbed energy is transformed into a photoacoustic pressure wave and how much is led into the disexcitation by fluorescence. Nevertheless, it is suitable for system tests.

Black ink is water dilutable and has the advantage of being absorbing over the whole tested wavelength range. However, it is a colloidal suspension, thus absorption and scattering coefficients cannot easily be determined, nor adjusted independently. Furthermore, it was observed, that the colloids sediment at surfaces which may falsify results. On the whole, it can be used for test purposes.

The remazol dyes are well suitable to adjust specific absorption coefficients. They are non-colloidal, water soluble, and available for several wavelength ranges. While the absorption spectrum of Remazol Turquois overlaps only by a small part with the wavelength range of the OPUS system, the red dye fits perfectly for the measurements with the wavelength 532 nm of a frequency doubled Nd:YAG laser. Using tunable OPO-laser systems, these dyes may also serve as reference dye to measure absorption coefficients by photoacoustic over broader wavelength ranges.

At last, the silicone dyes proved not to be useful for mimicking human tissue with the probable exception of the white dye. Since for the white dye the absorption is neglectable, it may be usable to adjust the scattering coefficient. But as the results of the integrating sphere measurements show, the determination of the scattering

coefficient has to be verified by another method. The red as well as the orange dye have their maximum close to the emission wavelength of the frequency doubled Nd:YAG laser (532 nm). Their disadvantage is their scattering behavior making it impossible to adjust the absorption and scattering coefficient independently. The photoacoustic measurements of the red dye demonstrate, that it is possible to determine the absorption coefficient separately. Furthermore, these measurements confirm the originally expected behavior of the absorption concentration correlation and therefore, indicate that the applied method especially the calculation procedure depicted in the section about integrating sphere measurements is not suitable to achieve absorption and scattering coefficients.

5. Conclusion

Summarized, the acoustical properties are adjustable [101] and the characterization of the materials shows that the optical properties of all materials can be adjusted to the desired parameters.

The final choice of the material and the absorber depends on the tissue to be mimicked and the wavelength of the laser. Since phantoms are used to simulate blood in human tissue or human breast tissue and to test the performance of the OPUS system, all materials except PAA are considered useful. PVA is the first choice to mimic the tissue, as it is easily producible with its scattering behavior and has appropriate acoustic properties. Therefor, all of them can be applied in the performance tests. The choice of dyes usable for the OPUS system is limited to ICG, black ink and to some extent to Remazol Turqois, due to its wavelength range from 690 nm to 870 nm. Although all these dyes have disadvantages, they can be employed for first quantitative measurements and performance tests. For further tests, other dyes should be characterized to verify if they are able to mimic the needed absorption in this wavelength range. Graphite or metal rods can be utilized as absorbers for simple non-quantitative performance tests.

Altogether, suitable phantom materials and absorbers, applicable with the OPUS system, have been identified.

IV. OPUS System

1. System overview and performance

The OPUS system is schematically depicted in figure IV.1. The main parts are an OPO-laser combination serving as light source and a commercial ultrasound system as detection unit. These components are synchronized by a trigger interface and coupled through an optoacoustic unit. The parts of the system and the different laser generations are described in more detail in the next paragraphs.

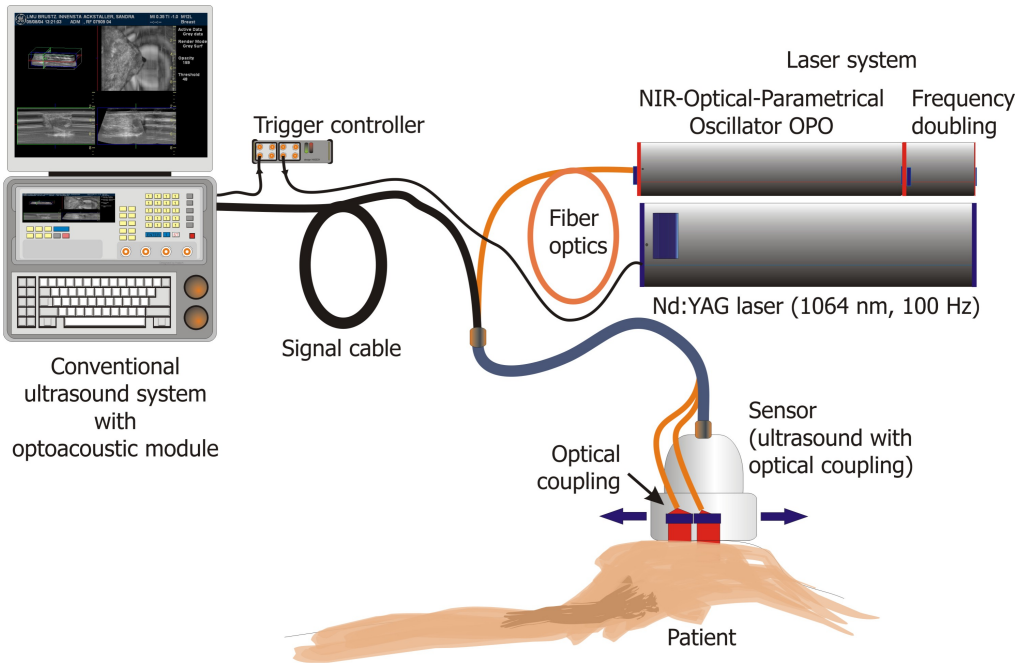

Figure IV.1.: Schematic of the OPUS setup.

1.1. Detection system and triggering

The commercial ultrasound scanner Logiq 9 with the transducer M12L, both GE - Global Research (Garching b. München, Germany) served as detection unit. The ultrasound scanner works at an imaging frame rate of 83 Hz. The ultrasound transducer with a center frequency of 8.8 MHz contains 192 channels performing 1D depth scans, the so-called A-scan. Since the channel readout is serial, the A-scan rate is 16 kHz. Each laser shot gives one photoacoustic A-scan (PA-line) record. Ultrasound scanner and laser are synchronized by a trigger interface. For practical reasons the ultrasound scanner serves as master trigger. With a laser repetition rate of 100 Hz and an ultrasound image frame rate of 83 Hz, one up to two PA-lines are produced during the record of one ultrasound image. The triggering scheme is shown in figure IV.2. Since the channels are alternating between ultrasound and photoacoustic signals (lines), it takes 88 lines for each method to build one image. This results in a photoacoustic image frame rate of approximately 1.1 Hz. Hence, using this recording scheme, it is possible to overlay the ultrasound and photoacoustic images online at the screen which enables the usage of the information of both methods at the same time. An overlay image of a photoacoustic image and an ultrasound image is presented in figure IV.3.

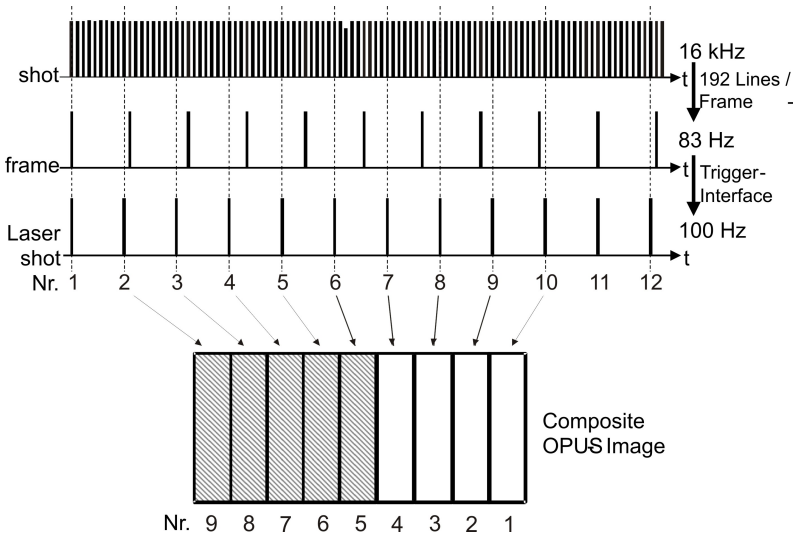

Figure IV.2.: Schematic of the triggering.

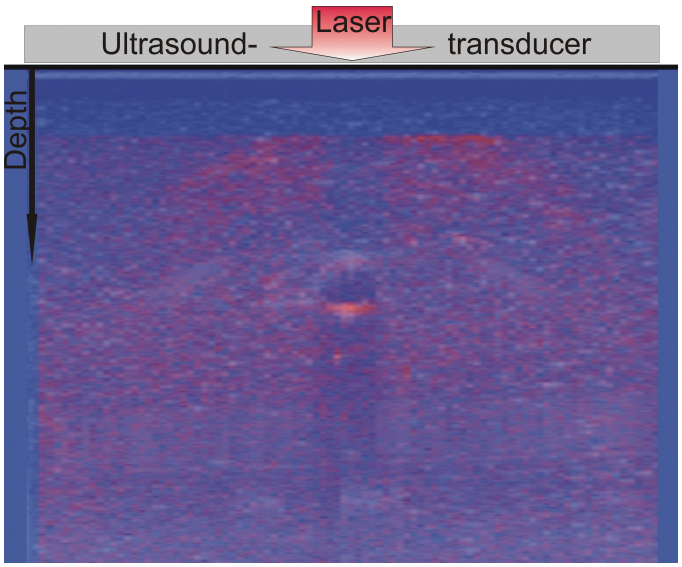

Figure IV.3.: Overlay photoacoustic and ultrasound image.

1.2. Light source

The optical excitation is forced by a pulsed frequency doubled Nd:YAG(@532 nm) laser pumping an OPO. The laser source operates with a repetition rate of 100 Hz and a pulse duration of approximately 10 ns. Three different Nd:YAG laser types (generations) have been developed by InnoLas (Krailling, Germany) to pump the OPO and are described below.

Laser generation I: flash lamp pumped

The first laser used is a frequency doubled SpitLight 600, which is flash lamp pumped. The special feature of this laser is the smallest water-water cooled power supply for a 100 Hz system world wide.

Laser generation II: diode pumped, flash lamp amplified

The second generation is a frequency doubled SpitLight Hybrid. The specialty of this hybrid laser is the combination of a diode pumped oscillator and a flash lamp pumped amplifier. In contrast to the broadband emission of a flash lamp, the diode emits in a small band which can be chosen near the excitation wavelength of the Nd:YAG (808 nm). With the small band emission, the pump efficiency is improved

and negative thermal side effects are strongly reduced.

Laser generation III: diode pumped, diode amplified

A frequency doubled SpitLight DPSS is the third laser generation. It is as well diode pumped as diode amplified. The diode pumped amplifier is less efficient than a flash lamp pumped, but the negative thermal side effects are stronger reduced. The energy is still sufficient to pump the OPO, and thereafter, sufficient for the application.

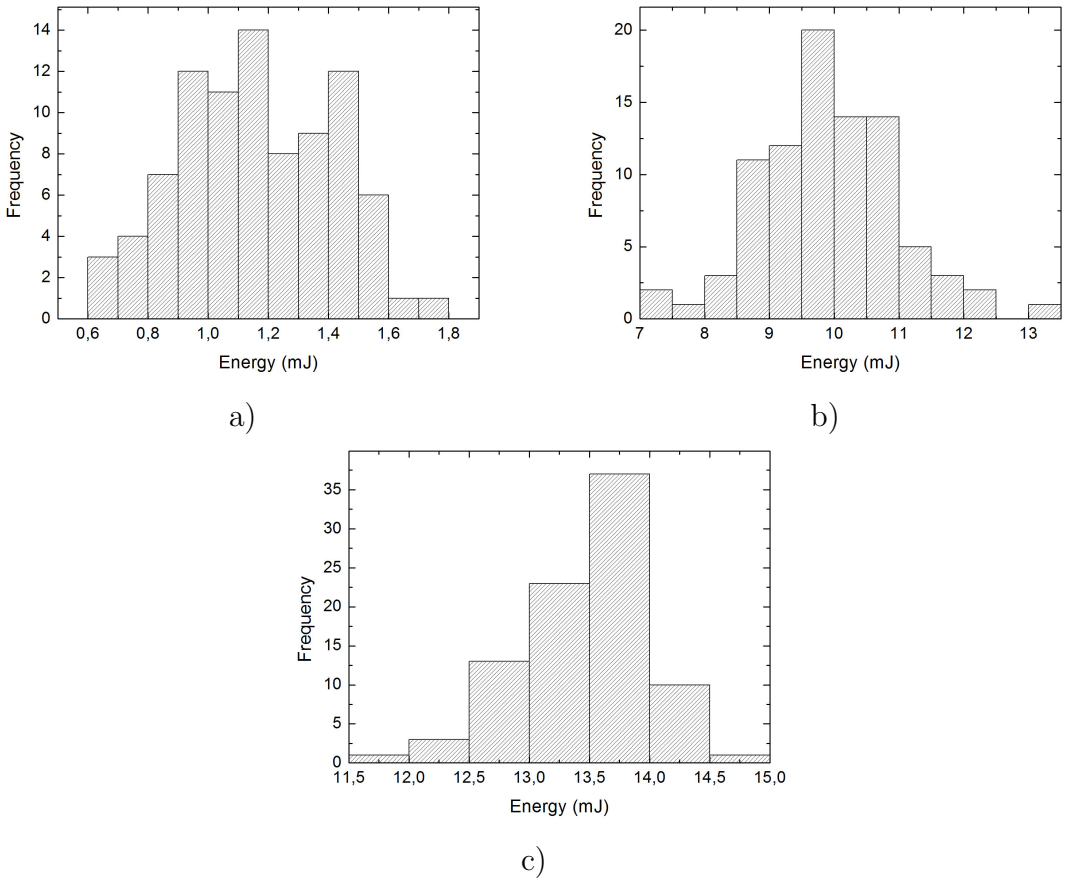

Figure IV.4.: Typical histograms of the pulse energies for a sequence of pulses equal to the number of pulses used to build one photoacoustic image for a) SpitLight 600, b) SpitLight Hybrid and c) SpitLight DPSS.

To enable wavelength dependent measurements, each laser was pumping a near-infrared OPO (Optical Parametrical Oscillator). The SpitLight 600 was pumping a OPO-S 532 (GWU, Erftstadt, Germany), while the SpitLight Hybrid and the SpitLight DPSS were both combined with a versaScan-L 532 (GWU, Erftstadt, Germany). Signal wavelengths in a range from 690 nm to 870 nm are used for the experiments.

Quantitative evaluations are performed from photoacoustic images. Since 88 laser shots are needed to build one photoacoustic image (frame) and the photoacoustic signal of each A-scan depends on the laser energy strong pulse-to-pulse fluctuations in this 88 shots would bastardize the resulting amplitude in the photoacoustic image. Moreover, images taken at different wavelengths cannot be quantitatively compared. Thus further development of the lasers is required.

Typical pulse energy statistics of the three laser generations are shown in figure IV.4 a)-c). For this purpose the energies of 88 pulses were recorded and evaluated. The SpitLight 600 has the broadest distribution, while the SpitLight DPSS has the smallest. This reflects the behavior, which was expected due to the improved pump efficiency with the diode.

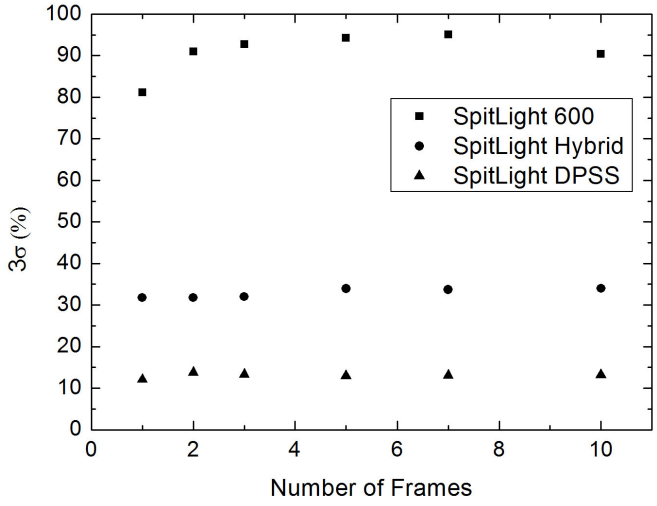

Figure IV.5.: Comparison of the 3σ statistics of SpitLight 600, SpitLight Hybrid and SpitLight DPSS for different number of frames.

Figure IV.5 compares the 3σ statistics of the three lasers. For statistical purposes, the data of five frames (photoacoustic images) are taken for calculations. The 3σ statistics are calculated for same number of frames. In this comparison, the Spit-

Light 600 has pulse-to-pulse fluctuations between 82% and 95%, while the SpitLight Hybrid obtained fluctuations of approximately $3\sigma = 32\%$ and the SpitLight DPSS of approximately 12%, respectively.

1.3. Optoacoustic unit

The basic idea of this setup is the usage of photoacoustic imaging as an add-on to conventional ultrasound to improve the acceptance of this method for medical applications. Hence, the optical excitation unit was not integrated into the ultrasound transducer, but that can be fixed to the transducer as a clip (see figure IV.6). The laser light is led fiber optically to a fiber connector at the clip. This fiber connector is movable over a curved bar to set different angles of incidence. The angles can be chosen between 20°, which is a nearly perpendicular incidence to the tissue surface, and 80°, which is flat incidence angle. The center of rotation is chosen to be the point of incidence. To form the laser beam to a long narrow beam along the side of the transducer, a cylinder lens is fixed in front of the connector. Since most parts along the side of the transducer shall be illuminated, a split fiber (y-fiber) coupled into two identical side-by-side connectors was used for some of the experiments. Both configurations, with the single fiber and with the y-fiber, are illustrated in figure IV.7. The beam illuminates a surface area of 12 mm × 3 mm for the single fiber and of 24 mm × 3 mm for the y-fiber. The legal limit (MZB) for laser radiation onto skin according to standard DIN EN 60825-1

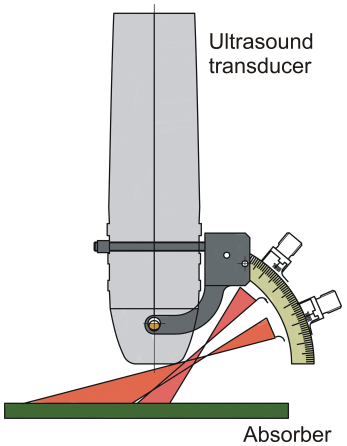

Figure IV.6.: Schematic side view of the optical unit coupled to the ultrasound transducer showing the changeable incident angles for the laser beam.

at 760 nm is 26.36 mJ cm^{-1}. For repetitive pulses, the limitation of the single pulse energy has to be corrected depending on the number of pulses applied. The strictest limitation is that of the continuous wave (cw) laser. For a 100-Hz repetition rate, the limit of the cw laser has to be applied. This limits the average power to 263.6 mW cm^{-1}. Resulting in a maximum pulse energy of 1.9 mJ for the illumination of the used area. The maximum energy that can be reached at the distal end of the fiber amounts to around 3 mJ depending on the laser output, but it can be down-regulated. For some of the experiments also higher energies have been used to test the system.

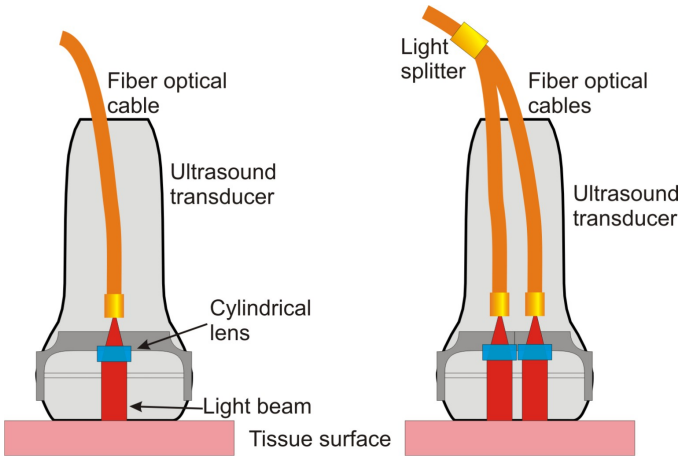

Figure IV.7.: Schematic of the coupling of the fiber optics to the ultrasound transducer with a single- and a y-fiber.

It is expected that the photoacoustic signal shows a dependency on the incidence angle of light in non-scattering media, given that the light is directed straight forward, and that the dependency is different at different depths. This fact was proven with a metal rod as absorber at different depths. The results are shown in figure IV.8 a). In non-scattering media, angles between 40° and 50° give highest intensities for depths from 10 cm to 25 cm. For lower depths large angles are needed. In scattering media, as expected the photoacoustic signal intensity is slightly dependent on the incidence angles, which is presented in figure IV.8 b). The scattering is usually not totally directed forward, but distributed broader, meaning that the light intensity reaching the absorber at a specific depth is lower than in non-scattering media. The light however can reach the absorber from a larger range of incidence angles, due to distribution.

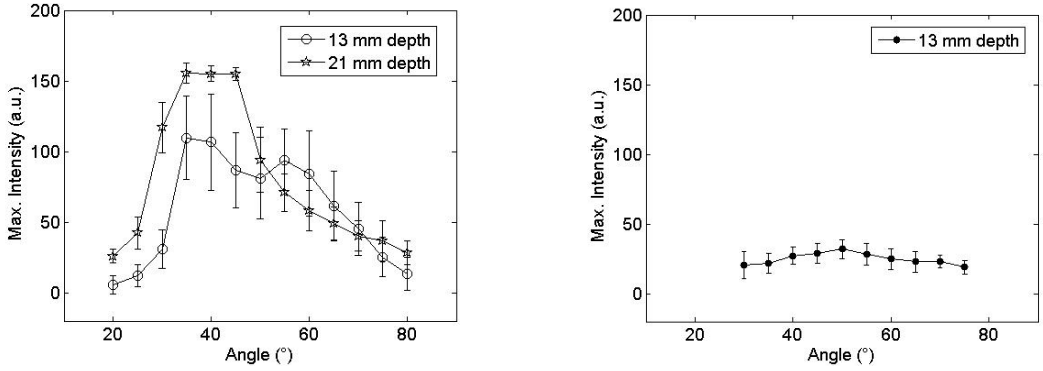

Figure IV.8.: Angular dependance of the photoacoustic signal of a metal rod in a) non-scattering media at depths of 13 mm and 21 mm and in b) scattering media at a depth of 13 mm.

2. Image reconstruction and evaluation

2.1. Image reconstruction algorithms

In recent years of photoacoustic research, proper image reconstruction algorithms have become a major focus. A circular backprojection [137, 138, 68, 82] is the standard approach. Its time-domain equivalent, the delay-and-sum algorithm is implemented as the standard reconstruction method in conventional ultrasound [139, 84]. Another approach, which allows very efficient reconstruction, is based on the Fourier transformation [86]. Improvements over these direct reconstruction approaches have been presented, such as iterative reconstruction [140, 141] and quantitative imaging [95]. Few data is available on the relative performance of these different reconstruction approaches.

Therefore, four methods will be compared in this work: 1) circular backprojection, 2) delay-and-sum, 3)Fourier transform and 4) Hough transform. The four methods and the used algorithms are presented in the following and have been described in more detail in [49].

Image Orientation

Figure IV.9 shows how the signal from a single point source is recorded and how it looks like in a raw data image. Since the wavefront from the single point source

is not planar, it reaches the detector elements at different times. Hence, the time delays result in a curved shape in the raw data image.

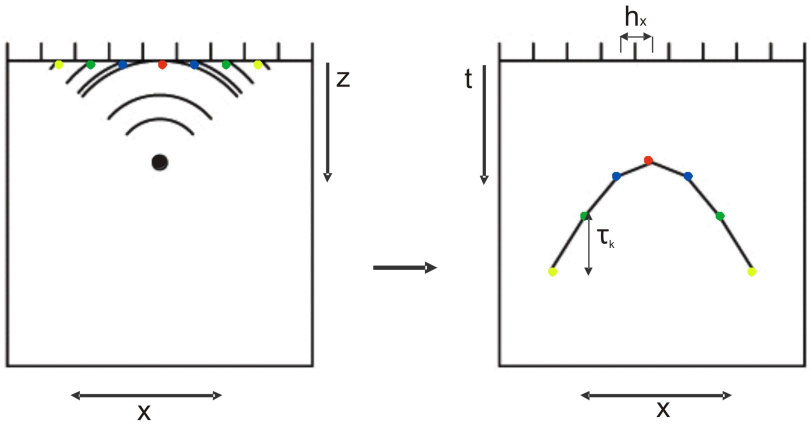

Figure IV.9.: Schematic of the generated sound waves by a point source and how they are detected and displayed in a raw data image.

Assuming that the linear transducer array acquires a 2D data set $s(x,t)$, which describes the surface pressure field along a lateral axis x and over the time t (see figure IV.9 right side). Such an array is composed of parallel aligned piezo elements with a fixed distance h_x. For each element, the data is stored digitally with a sample length h_t. Therewith, the data set is defined over the discrete domain

$$\Sigma = \{x_1, x_2, \ldots, x_N\} \times \{t_1, t_2, \ldots, t_M\},\ x_{l+1} = x_l + h_x,\ t_{k+1} = t_k + h_t. \quad \text{(IV.1)}$$

N denotes the number of elements and M the number of samples.
The pressure reconstruction is the transition from the signal domain Σ to the image domain

$$\Omega = \{x_1, x_2, \ldots, x_N\} \times \{z_1, z_2, \ldots, z_M\}, \quad z_{j+1} = z_j + h_z, \quad \text{(IV.2)}$$

where z is the depth, orthogonal to x. The objective is the computation of the pressure distribution $p(x_i, z_j)$ from the recorded signals $s(x_l, t_k)$ in consideration of an estimated speed of sound c_0.

Circular Backprojection (CBP)

In medical image reconstruction backprojection is a widely used technique[138, 68, 82]. Basically it projects each recorded signal onto all possible origins. Given a certain record sample $s(x_l, t_k)$, its origin lies somewhere on the circle

$$K^{l,k} = \left\{(x, z) \in \mathbb{R}^2, \quad (x - x_l)^2 + (z - c_0 t_k)^2 = r_k^2\right\}. \tag{IV.3}$$

with the radius $r_k = c_0^2 t_k^2 \in \mathbb{R}^+$. Figure IV.10 shows exemplarily the calculated origins of a photoacoustic signal in the time-domain. $K^{l,k}$ does not necessarily lie in Ω. Thus, the approximation is being defined by

$$K_h^{l,k} = \left\{(x_i, z_j) \in \Omega, \quad |x_i - x_l| \leq r_k,\, z_j \approx \sqrt{r_k^2 - (x_i - x_l)^2}\right\}. \tag{IV.4}$$

The next step is the superposition of the signal values $s(x_l, t_k)$ in the image domain Ω. The image

$$p(x_i, z_j) = 0 \quad \forall (x_i, z_j) \in \Omega \tag{IV.5}$$

is initialized and the signal amplitudes are added:

$$p(x_i, z_j) = p(x_i, z_j) + s(x_l, t_k) \quad \forall (x_i, z_j) \in K_h^{l,k}. \tag{IV.6}$$

The directional transducer receptivity depends on the angle of incidence of the pressure signal. This is regarded by weighting the single summands. The optimal weighting factors, specifically those, who maximize the signal-to-noise ratio (SNR), are exactly the directivity factors of the transducer [139]. The directivity function

$$d : \left[-\frac{\pi}{2}, \frac{\pi}{2}\right] \to [0, 1] \tag{IV.7}$$

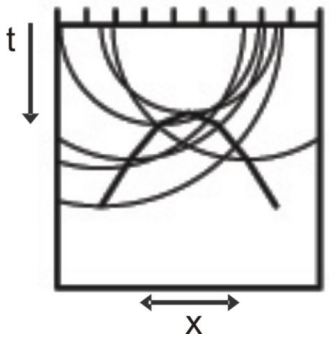

Figure IV.10.: Example for calculated origins of a PA signal in the time-domain.

returns these factors depending on the angle

$$\beta_{i,l,j} = \arctan\left(\frac{x_i - x_l}{z_j}\right). \tag{IV.8}$$

The number of superpositions varies over Ω. Points close to the borders (x_1, z_j) and (x_N, z_j), $j \in [1, M]$, are less allocated to circles $K_h^{l,k}$ than central points. Deeper points (large index j) are more often allocated, since the radii r_k are larger, and therefore, $K_h^{l,k}$ contains more elements. This results in varying pixel intensities $p(x_i, z_j)$ depending on the image region. This is regarded by a so-called *density compensation*: The number of superpositions are encountered for every point in Ω in a map

$$C : \Omega \to \mathbb{N}_0, \tag{IV.9}$$

and the image $p(x_i, z_j)$ is divided by C after the superposition step.

Algorithm 1: Circular backprojection (CBP)

Set $p(x_i, z_j) = 0$ *and* $C(x_i, z_j) = 0$ *for* $(x_i, z_j) \in \Omega$.

For $k = 1, \ldots, M$*:*

- *Compute radius* $r_k = c_0 t_k$.
- *For* $l = 1, \ldots, N$*:*
  1. *Compute* $K_h^{l,k}$ *according to (IV.4).*
  2. *For every* $(x_i, z_j) \in K_h^{l,k}$*:*
     a) *Superimpose the weighted signals:* $p(x_i, z_j) = p(x_i, z_j) + d(\beta_{i,l,j}) s(x_l, t_k)$.
     b) *Count superposition:* $C(x_i, z_j) = C(x_i, z_j) + 1$.

Apply density compensation: $p(x_i, z_j) = p(x_i, z_j)/C(x_i, z_j) \quad \forall (x_i, z_j) \in \Omega$.

Delay-and-Sum (DnS)

The DnS is a reconstruction method applied in the x-z-space, but in conventional US, the superposition for a certain focal depth is done in the x-t-space. This

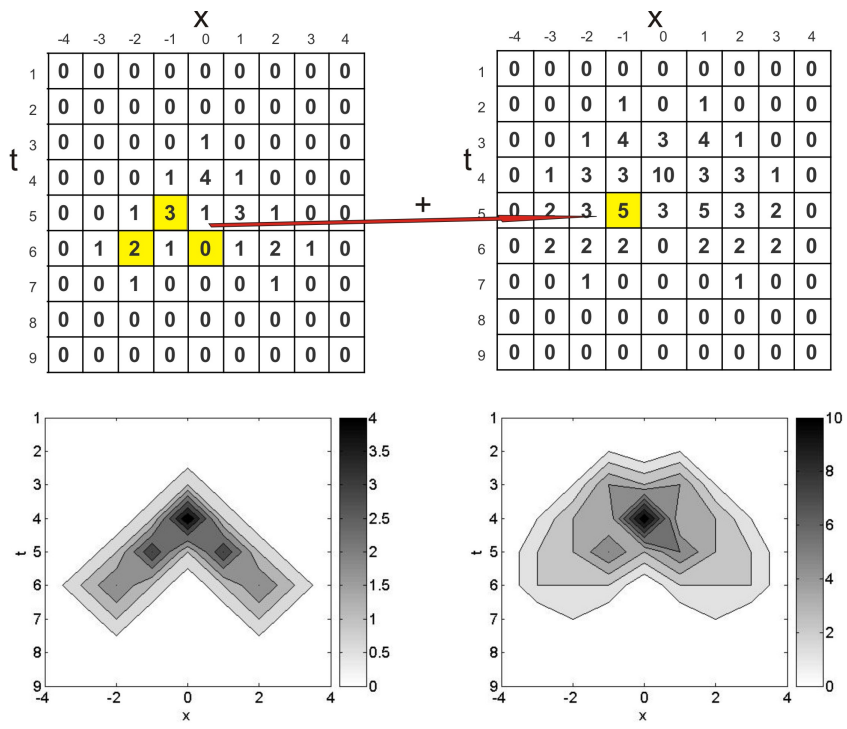

Figure IV.11.: A simple example for the Delay-and-Sum algorithm.

idea can be transferred to photoacoustic image reconstruction [139, 84]. For a signal sample at (x_l, t_k) the proper delay τ_k is a function of the number of channels between x_l and the neighbors $x_{l\pm m}$, $m \in \mathbb{N}$:

$$\tau_k : [1, N] \subset \mathbb{N}_0 \to \mathbb{R}^+, \quad \tau_k(m) = \sqrt{t_k^2 + m^2 h_x^2} - t_k. \tag{IV.10}$$

The obtained superimposed signal is

$$S(x_l, t_k) = \sum_{m=-N'}^{N'} s(x_{l+m}, t_k + \tau_k(m)). \tag{IV.11}$$

The number of regarded neighbors N' should be related to the transducer directivity d (see equation (IV.7)). Also directivity dependent weighting factors should be included. Thus, the angle of incidence is calculated by

$$\beta_{m,k} = \arctan\left(\frac{m h_x}{t_k c_0}\right), \tag{IV.12}$$

and determined N' with the threshold $a \in [0, 1]$:

$$N' = \max\{m \in [0, N], \quad d(\beta_{m,k}) \geq a\} \tag{IV.13}$$

It has to be ensured, that the summation is limited to the domain Σ. Therefore the lower and upper summation limit are set to

$$L = \max\{l - N', 1\}, \qquad U = \min\{l + N', N\}. \tag{IV.14}$$

A simple example for the DnS algorithm is shown in figure IV.11. It can be seen how the signal changes with summing the nearest neighbors.

Similar to the CBP, a density compensation has to be applied. Since the superpositions for a certain point (x_l, t_k) are realized in one step, it is not necessary to store a whole density map. The resulting signal sample can just be divided by the number of superimposed samples $L + U + 1$.

The resulting signal $S(x_l, t_k)$ is then converted to the pressure distribution $p(x_i, z_j)$ by identifying the x-coordinate and computing the z-coordinate by rescaling the step widths

$$h_z = h_t c_0. \tag{IV.15}$$

Algorithm 2: Delay-and-sum (DnS)

For $k = 1, \ldots, M$:

1. *Compute the number of the relevant neighbors N' from (IV.13).*
2. *Compute the delays $\tau_k(m)$ for $m \leq N'$ according to (IV.10).*
3. *Compute angles $\beta_{m,k}$ for $m \leq N'$ according to (IV.12).*
4. *For $l = 1, \ldots, N$:*
   - *Determine lower and upper summation limit L and U according to (IV.14).*
   - *Superimpose signals*
     $S(x_l, t_k) = \frac{1}{L+U+1} \sum_{m=L}^{U} s(x_{l+m}, t_k + \tau_k(m)) d(\beta_{m,k})$.

Rescale $S(x_l, t_k)$ according to (IV.15) to obtain $p(x_i, z_j)$.

Generalized Hough Transform Algorithm (HTA)

The Hough Transform is a tool for model based image segmentation, which allows the extraction of geometric shapes within a binary image $I : D \to \{0, 1\}$ [142]. By applying this tool, a new photoacoustic image reconstruction method is derived. A geometric shape can be described by the set

$$K_p = \{(x_l, t_k) \in D, g_p(x_l, t_k) = 0\} \tag{IV.16}$$

with the mapping $g_p : D \to \mathbb{R}$. The index p denotes the dependency on certain parameters, which can be written into a vector $p \in \mathbb{R}^d$, $d \in \mathbb{N}$. This motivates the introduction of the parameter space $P \subset \mathbb{R}^d$, that contains all possible parameter assignments. Every possible location of K_p in the image corresponds to a certain point p_0 in P.

All possible shapes through a fixed point (x_l, t_k) result in a curve

$$H_{l,k} = \{p \in P, h_{l,k}(p) = 0\} \tag{IV.17}$$

with the mapping $h_{l,k} : P \subset \mathbb{R}^d \to \mathbb{R}$. If two points (x_l, t_k) and (x_m, t_n) in D belong to the same shape, their parameter curves $H_{l,k}$ and $H_{m,n}$ intersect in exactly that point, that corresponds to the shape in the image. If the transformation to the parameter space is performed for every foreground pixel $(x_l, t_k) \in D$, $I(x_l, t_k) = 1$, clusters in P are obtained, which highlight the shape locations in D.

The applicability of the HTA on photoacoustic signals is based on the distance dependent arrival time of the waves. Photoacoustic point sources in Ω lead to hyperbolas in Σ. Those hyperbolas are described by

$$K_p = \{(x_l, t_k) \in \Sigma, \quad g_p(x_l, t_k) \approx 0\} \tag{IV.18}$$

$$g_p(x_l, t_k) = \frac{1}{c_0^2}(x_l - x_S)^2 - t_k^2 + t_S^2 \tag{IV.19}$$

and the apex coordinates (x_S, t_S). Since the speed of sound c_0 is assumed to be constant, x_S and t_S completely determine the shape and location of the hyperbola. Thus, they are identified as the shape parameters p. Hence, the parameter space

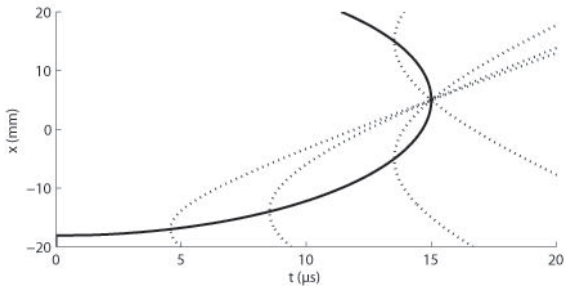

Figure IV.12.: Hyperbolas through the point $(x_l, t_k) = (5\text{ mm}, 15\text{ mm})$ and the resulting parameter curve (parabola) of the apex coordinates.

$P \subset \mathbb{R}^2$ is the set of all possible apex coordinates. Focusing on hyperbolas in the bounded space Σ, both domains can be identified:

$$P = \{(x_S, t_S) \in \mathbb{R}^2, \quad x_S \in \{x_1, \ldots, x_N\},\, t_S \in \{t_1, \ldots, t_M\}\} = \Sigma. \tag{IV.20}$$

The parameter curve $H_{l,k}$ describes a parabola in Σ (see figure IV.12) and can be written as the set

$$H_{l,k} = \left\{ (x_S, t_S) \in \Sigma, \quad |x_S - x_l| \leq c_0 t_k,\, t_S \approx \sqrt{t_k^2 - \frac{1}{c_0^2}(x_S - x_l)^2} \right\}. \tag{IV.21}$$

The extraction of the hyperbolas enables the reconstruction of the pressure distribution $p(x_i, z_j)$: An apex coordinate (x_S, t_S) is directly related to a pressure source $(x_S, z_S) = (x_S, c_0 t_S)$. Since the parameter space was identified with the signal domain, there is no need to apply an inverse transform to obtain the final image. In contrast to the original application, there are no binary images to deal with, but the superposition of all $H_{l,k}$ weighted with the amplitude $s(x_l, t_k)$ will gain the real source locations.

Like in the algorithms CBP and DnS, the superposition density varies within $s'(x_S, x_S)$. Therefore, a density map $C : \Sigma \to \mathbb{N}_0$ is defined (see equation IV.9) and the number of superpositions are counted. In the end, $s'(x_S, t_S)$ becomes normalized by $C(x_S, t_S)$.

An advantage of this approach is the ability to apply special weighting factors: If a sample at (x_l, t_k) is really part of a hyperbola with the parameters (x_S, t_S), both values $s(x_l, t_k)$ and $s(x_S, t_S)$ should show a high amplitude. Hence, the normalized

amplitude at the apex is chosen as a weighting factor

$$w : \Sigma \to [0,1], \quad w(x_S, t_S) = \frac{|s(x_S, t_S)|}{\max\{s(x_l, t_k),\ (x_l, t_k) \in \Sigma\}}. \tag{IV.22}$$

The weighting could consider more hyperbola elements than the apex itself. This may increase the reliability in the case of disturbed signals and instabilities of the laser energy. Like in the DnS, the resulting signal $s'(x_S, t_S)$ can be rescaled to the pressure distribution $p(x_i, z_j)$ (see equation IV.15).

Algorithm 3: Generalized Hough transform algorithm (HTA)

1. *Set* $s'(x_l, t_k) = 0$ *and* $C(x_l, t_k) = 0$ *for* $(x_l, t_k) \in \Sigma$.
2. *For* $(x_l, t_k) \in \Sigma$*:*
   - *Compute the parabola* $H_{l,k}$ *of the possible apex coordinates according to (IV.21).*
   - *For* $(x_S, t_S) \in H_{l,k}$*:*
     - *Compute weighting factor* $w(x_S, t_S)$ *according to (IV.22).*
     - *Superimpose signals* $s'(x_S, t_S) = s'(x_S, t_S) + w(x_S, t_S)s(x_l, t_k)$.
3. *Apply density compensation.*
4. *Rescale* $s'(x_l, t_k)$ *according to (IV.15) to obtain* $p(x_i, z_j)$.

Fourier Transform Algorithm (FTA)

The three up to now presented algorithms, CBP, DnS, and HTA, are all based on superposition. They try to gain the real pressure sources by overlaying high amplitude values resulting in typical superposition artifacts and blurred images. In contrast FTA as fourth algorithm tries to calculate an exact reconstruction of the pressure distribution by rescaling the temporal frequencies in the Fourier domain [86].

The propagation of the pressure waves complies with the 2D wave equation [143]

$$u_{tt} - c_0^2 \Delta u = 0. \tag{IV.23}$$

For the purpose of finding a solution $u(x,t)$, a general approach with a harmonic function is considered:

$$u = u_0 \exp(i(\omega t - \kappa_x x - \kappa_z z)) \tag{IV.24}$$

with the circular frequency ω and wave vector $\kappa = \kappa_x e_x + \kappa_z e_z$. The vectors e_x and e_z are the unity basic vectors in the x-z-coordinate system. The derivatives are

$$\begin{aligned} u_{tt} &= (i\omega)^2 u \\ \Delta u &= (i\kappa_x)^2 u + (i\kappa_z)^2 u. \end{aligned} \tag{IV.25}$$

If these formulas are substituted into the wave equation (IV.23), it is stated that a solution (IV.24) of the wave equation has to comply with

$$\omega^2 = c_0^2(\kappa_x^2 + \kappa_z^2) = c_0^2 \left|\kappa\right|. \tag{IV.26}$$

Equation (IV.26) is named *dispersion relation* and describes the relation between temporal and spatial frequencies of a wave. Thus, the spatial Fourier transform can be calculated from the temporal Fourier transform, which induces the following reconstruction algorithm:

Consider the signal $s(x,t)$, $(x,t) \in \mathbb{R} \times \mathbb{R}^+$. Since the domain is defined only for positive times $t \geq 0$, the continuation $s(x,-t) = s(x,t)$ will be defined. Therewith, $s : \mathbb{R}^2 \to \mathbb{R}$ describes an even function in time, and hence, its Fourier transform can be reduced to a cosine transformation:

$$\widehat{s}(\kappa_x, \omega) = \int_0^\infty \int_{-\infty}^\infty s(x,t) \exp(-i\kappa_x x) \cos(\omega t)\, dx\, dt. \tag{IV.27}$$

On the other hand, $p(x,z)$ should be calculated. Its 2D Fourier transform reads

$$\widehat{p}(\kappa_x, \kappa_z) = \int_{-\infty}^\infty \int_{-\infty}^\infty p(x,t) \exp(-i(\kappa_x x + \kappa_z z))\, dx\, dz. \tag{IV.28}$$

Applying the dispersion relation (IV.26):

$$\widehat{p}(\kappa_x, \kappa_z) = \widehat{p}\left(\kappa_x, \sqrt{\omega^2 - c_0^2\kappa_x^2}\right) = C(\omega, \kappa_x)\widehat{s}(\kappa_x, \omega). \tag{IV.29}$$

The factor $C(\omega, \kappa_x)$ in front of $\widehat{s}(\kappa_x, \omega)$ is the result of the conversion of the differentials $d\omega$ and $d\kappa_z$:

$$\frac{1}{C} = \frac{d\kappa_z}{d\omega} = \frac{d}{d\omega}\sqrt{\frac{\omega^2}{c_0^2} - \kappa_x^2} = \frac{\omega}{c_0\sqrt{\omega^2 - c_0^2\kappa_x^2}}. \tag{IV.30}$$

Consider the discrete setting. The discrete frequencies for the time t_k and depth z_k, respectively, read:

$$\omega_k = \frac{k}{h_t M}, \quad \kappa_{z,k} = \frac{k}{h_z M} = \omega_k \frac{h_t}{h_z}, \quad k = 1, \ldots, M. \tag{IV.31}$$

For κ_x, negative frequencies have to be taken into account as well, since also x might be defined in a negative range. There is

$$\kappa_{x,l} = \frac{l - N_1}{h_x N_2}, \quad l = 1, \ldots, N, \quad N_1 = \frac{x_1}{h_x}, \quad N_2 = \frac{\max\{|x_1|, |x_N|\}}{h_x}. \tag{IV.32}$$

Algorithm 4: Fourier transform algorithm (FTA)

1. *Define frequencies $\kappa_{x,l}$, ω_k, and $\kappa_{z,k}$ according to (IV.31) and (IV.32).*
2. *Compute the 2D discrete Fourier transform (DFT) of $s(x_l, t_k)$: $\widehat{s}(\kappa_{x,l}, \omega_k)$.*
3. *For $k = 1, \ldots, M$ and $l = 1, \ldots, N$:*
   - *According to the dispersion relation (IV.26) compute $\kappa_{z,k} \approx \sqrt{\frac{\omega_k^2}{c_0^2} - \kappa_{x,l}}$.*
   - *Assign values $\widehat{p}(\kappa_{x,l}, \kappa_{z,k}) = C(\omega_k, \kappa_{x,l}) \widehat{s}(\kappa_{x,l}, \omega_k)$.*
4. *Compute $p(x_i, z_j)$ as the inverse DFT of $\widehat{p}(\kappa_{x,l}, \kappa_{z,k})$.*

2.2. Image evaluation

In contrast to absorption measurements without spatial resolution, the extraction of quantitative information from image data is not straight forward and the proper choice of mathematical evaluation is pivotal in order not to lose relevant information [80].

In a first step, an average of five raw data images is taken to minimize the influence of the laser energy fluctuation on the recorded data. Afterwards, an average of five raw blank images is subtracted to eliminate measurement artifacts. The resulting images are then reconstructed by the algorithms described in the section above. These steps can be followed by the example of a point source depicted in figure IV.13.

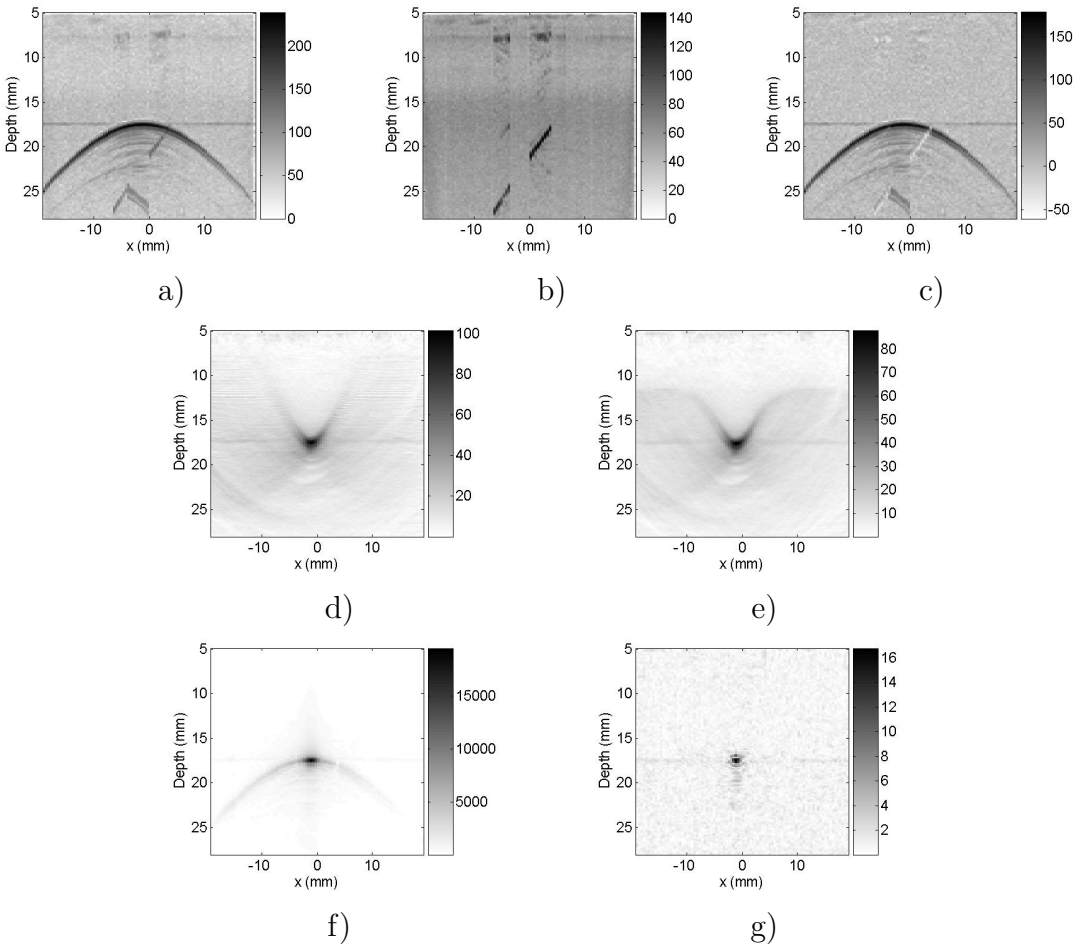

Figure IV.13.: a) Raw data image of a point source (graphite rod) with diameter 0.35 mm at 18 mm depth in a low scattering phantom (5 images averaged); b) raw data image of the blank (phantom without absorber, 5 images averaged); c) raw data image of the point source with the blank subtracted; reconstructed by d) CBP, e) DnS, f) HTA and g) FTA.

The next step is the separation of data points carrying significant information from those bearing only noise. Plotting the intensity distribution, as it is exemplarily shown in figure IV.14, the background level can be clearly identified by its normal distribution around the most frequent intensity. This approach for the identification of the background signal is even feasible for images of very structured samples. Assuming a normal distribution, the standard deviation of the background s_b is given by the full width at half maximum (FWHM) of the normal distribution. s_b is calculated from the distribution constructed by mirroring the distribution below

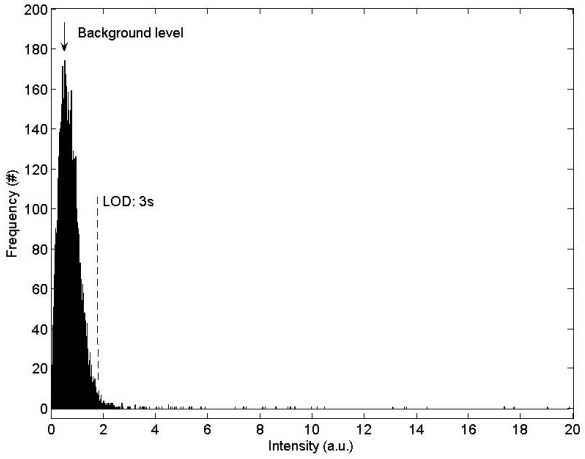

Figure IV.14.: Intensity distribution of a FTA reconstructed photoacoustic image of a point source.

the background level. By definition, the limit of detection (LOD) is 3 times the standard deviation s_b counted from the background level. The image values are shifted to the background level by subtracting the background value from all data points. All pixels with intensities larger than $3s_b$ are considered significant, while all pixel values below the LOD are regarded as bearing noise only and are set to zero consequently. Such a threshold image after FTA reconstruction is illustrated in figure IV.15.

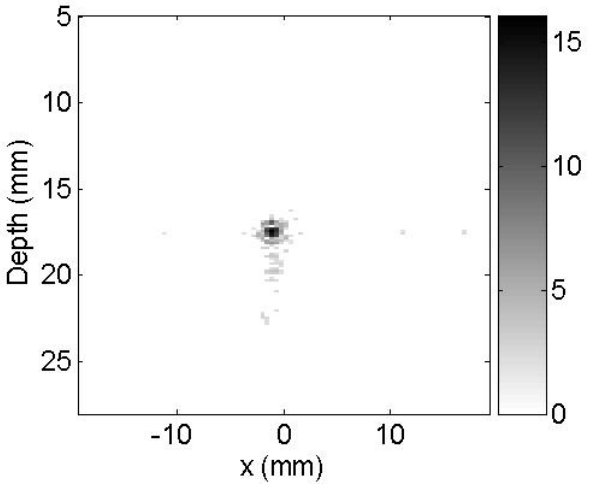

Figure IV.15.: FTA reconstructed image of the graphite rod point source after thresholding.

2.3. Results of the evaluation

The four reconstruction algorithms presented differ with respect to resolution, contrast, size reconstruction and computation time. Therefore, they were analyzed regarding their performance with data sets, acquired by the OPUS system (see figure IV.1), to show their suitability for the OPUS system. Graphite rods served as point sources and were embedded in an agar phantom (2%) with acoustic properties as described in chapter III. A similar evaluation was made with hydrophone measurements, the results are depicted in [49]. Therein, the algorithms are presented in more detail.

Reconstruction speed

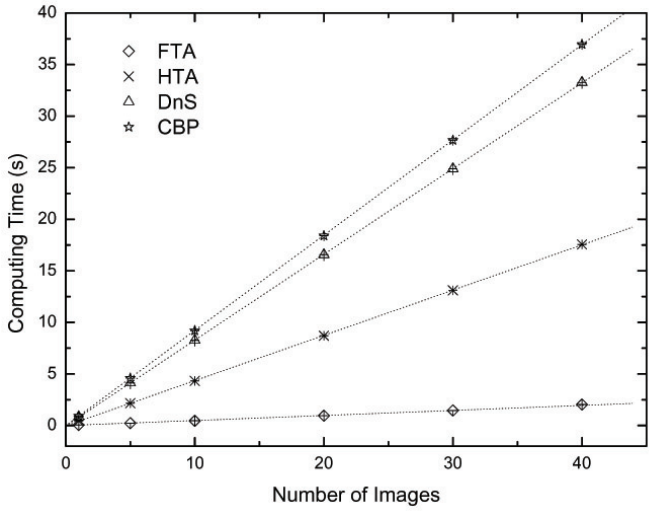

Figure IV.16.: Computing time depending on the number of 88×200 pixel images for FTA, HTA, DnS, CBP.

In medical imaging, fast recording is important to avoid movement artifacts, caused for example by respiration motions. It is sometimes beneficial to average a few recorded raw data images. When the reconstructed image should be visible immediately after recording a short computation time is required. Figure IV.16 presents the linear increase of computation time for an increasing image number of a specific size of 88×200 pixels. For computation, a computer equipped with a 3-GHz processor, 2 GB RAM, and MATLAB 7.0.4 (Mathworks) was used. The reconstruction time for the three superimposition algorithms strongly increases with larger num-

ber of images. This is caused by the fact that calculations are required for every depth. This is time consuming. The FTA turns out to be much faster than the other algorithms especially for large number of images. FTA allows reconstruction of around twenty photoacoustic images of 88×300 pixels while CBP, DnS, and HTA need significantly more computation time. The computation time depending on image size was shown in [49]. Only FTA allows real-time reconstruction, since the photoacoustic frame rate of the OPUS system lies at 1.1 Hz for the 88 A-scans.

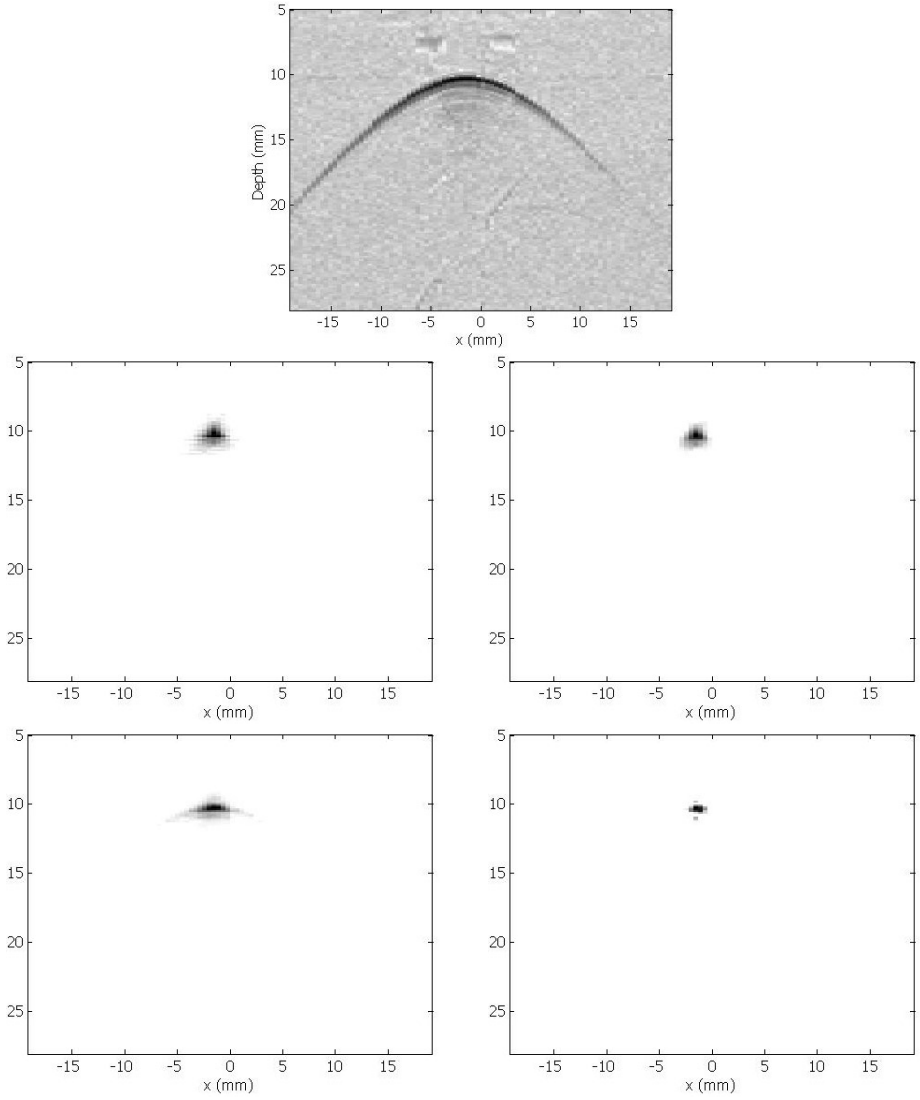

Figure IV.17.: From top to down right, the raw data image and the reconstructed images based on CPB, DnS, HTA, and FTA of a point source (graphite rod) with diameter 0.35 mm at 10 mm depth are illustrated.

Point source reconstruction

For photoacoustic medical imaging as for ultrasound imaging it is important to depict objects of a specific size without enlargement. All algorithms were tested in their quality to reconstruct a point source at different depths. Therefore, the FWHM had to be calculated from the threshold image. All pixels with intensities of less than half the maximum intensity were set to zero. The remaining intense pixels were counted in lateral and axial direction and multiplied by the width of the pixels, which is 0.44 mm in lateral and 0.15 mm in axial dimension. For a depth of 10 mm, the raw data image as well as the differently reconstructed images of a point source with diameter 0.35 mm are exemplarily shown in figure IV.17.

The lateral and axial FWHM at different depths for the four reconstruction algorithms are depicted in figure IV.18. The FTA shows the best results in lateral and axial directions. In the lateral profile, the FWHM has a minimum in the depth dependency for all algorithms which is affected by the focal zone of the ultrasound scanner which was set at a depth of 14 mm. Hence, the reconstruction algorithms perform best at this depth. The differences between the algorithms in reconstructing point sources, are larger in the lateral than in the axial direction.

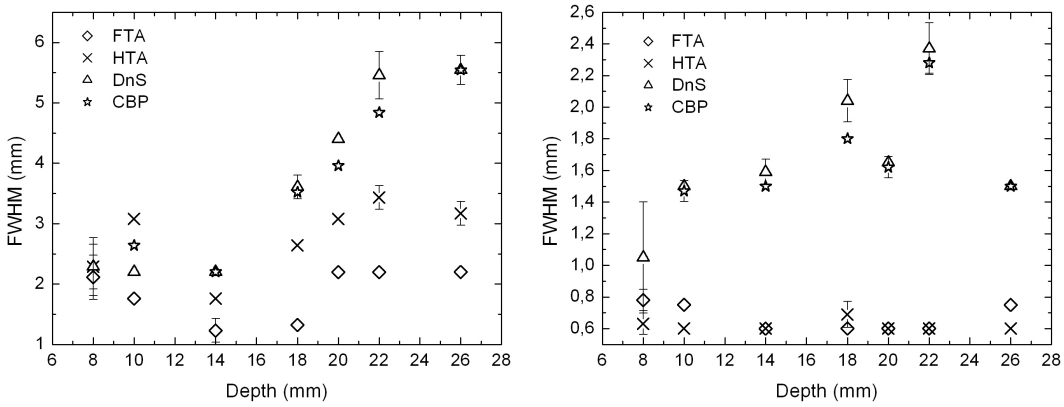

Figure IV.18.: Lateral (left) and axial (right) FWHM in mm of a reconstructed point source (graphite rod) with a diameter of 0.35 mm versus depth for FTA, HTA, DnS, and CBP.

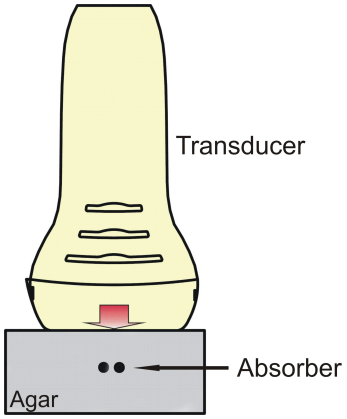

Figure IV.19.: Schematic setup with an agar phantom for resolution test with graphite rod as absorber.

Minimum lateral peak-to-peak distance

Another important aspect for quantitative evaluations of photoacoustic images is the capability of spatially separating the origins of two photoacoustic signals. The object size after reconstruction influences the minimum distance to distinguish between two sources. To obtain the minimum resolvable lateral peak-to-peak distance, two graphite rods, both of a diameter of 0.35 mm, as point sources were placed at different distances for the data acquisition (see figure IV.19). Exemplarily, one of the recorded images together with the FTA based reconstructed image and its corresponding lateral profile is illustrated in figure IV.20.

To resolve two sources, the intensity level between them must be lower than half the intensity of the maximum peaks. Hence, the number of pixels between the two sources fulfilling this condition were counted and multiplied with the lateral width

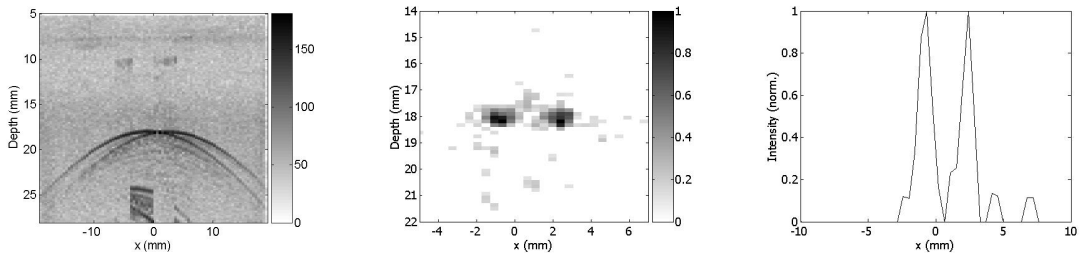

Figure IV.20.: From left to the right: recorded raw image, the FTA based reconstructed image and the corresponding lateral profile (x-direction) of two point sources (graphite rod with diameter 0.35 mm) at a distance of 3 mm.

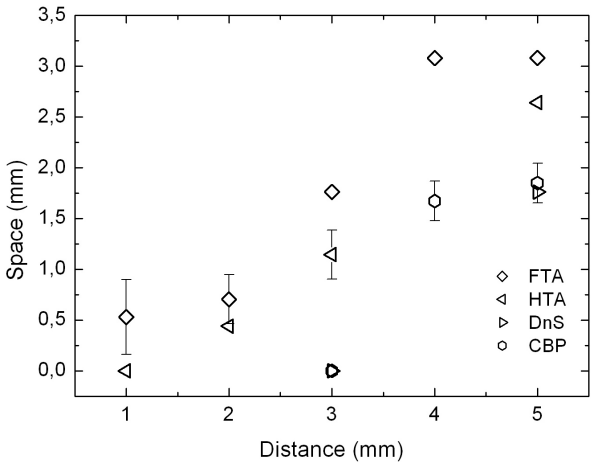

Figure IV.21.: Space between two peaks where the intensity is lower than half the maximum peak intensity for different peak-to-peak distances.

of the pixels (0.44 mm). The spaces obtained were plotted against the distance of the two point sources. The results are shown in figure IV.21. The FTA shows the best results with a minimum distance of 1 mm. The minimum space detected for HTA was 2 mm and it is 5 mm for DnS and 4 mm for CBP. Compared to the results presented in [49], the algorithms show lower detectability with real data of the OPUS system, which is effected by the large FWHM compared to the original size of the absorbers. It has also to be taken into account, that with a depth dependent FWHM the lateral resolution is also depth dependent. Which means, that for DnS and CBP a higher lateral resolution should be reached at a depth of 14 mm.

Signal-to-Noise ratio

The FWHM has been shown to be depth dependent, hence, the SNR was also expected to show a depth dependency. In order to obtain the SNR, the quotient of the signal amplitude after filtering and the standard deviation was determined using the identical data set as for the FWHM. Figure IV.22 presents the resulting SNR with regard to the depth.

The HTA shows the best SNR of all algorithms, while the SNR of FTA, DnS, and CBP is similar and about half of that of HTA. These results show a similar trend as seen with the hydrophone measurements presented in [49]. While for the CBP

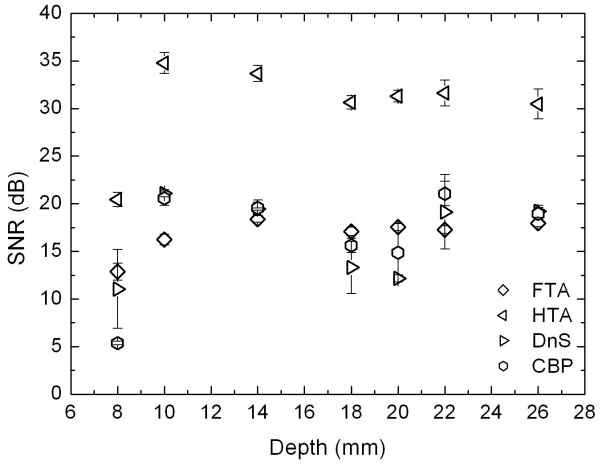

Figure IV.22.: Signal-to-noise ratio in dB versus depth for FTA, HTA, DnS, and CBP.

and DnS the SNR is reduced due to the broad superposition artifacts, the SNR of the HTA is even increased by the special weighting factors, with regard the pixel values at the possible apex coordinates.

Robustness

Since each laser pulse corresponds to one A-line in the image, instabilities of the laser energy lead to a variation of the signal amplitudes within the acquired signal during scans. Hence, the laser energy influences each A-line of each of those images. After reconstruction, the maximum amplitudes of DnS and CBP show a smaller standard deviation in a series of five image as the other methods, so that they seem less sensible to laser energy fluctuations as it can be seen in table IV.1.

Table IV.1.: Performance of the reconstruction algorithms with fluctuations of the laser energy: maximum amplitude at a depth of 10 mm with best SNR and standard deviation (STD) of the four reconstruction algorithms.

	FTA	HTA	DnS	CBP
Max. amplitude	13.27	11232	84.52	75.49
STD	0.19	278.12	0.75	0.74
STD (%)	1.4	2.5	0.9	1.0

3. First Results with the OPUS system and a PA sensor stick

For all measurements presented in this section the OPUS system with the first laser generation SpitLight 600 was used.

3.1. Pre-test

Before the characterization of the OPUS system and the quantitative measurements some preliminary tests have been performed.

One possible application considered for the OPUS system is breast imaging. The imaging depth shall be up to 3 cm. Since breast tissue consists mainly of fat it was tested whether the light is able to penetrate through a 15 mm thick layer of pig fat or not. The photoacoustic signal of the metal plate was clearly visible as seen in figure IV.23.

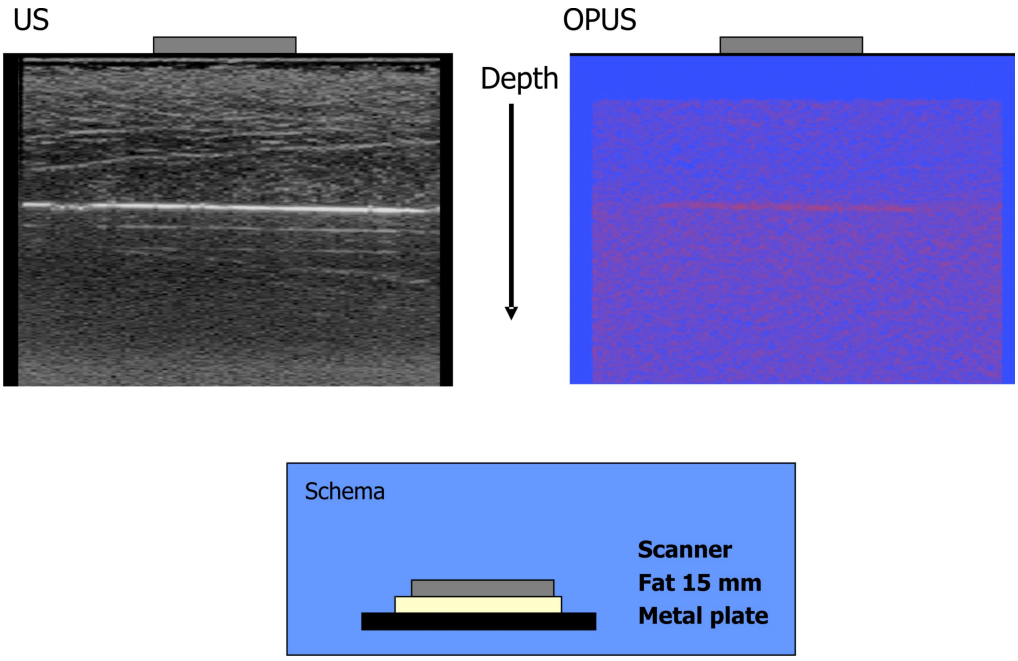

Figure IV.23.: Ultrasound (left) and photoacoustic (right) image of a metal plate below 15 mm pig fat layer.

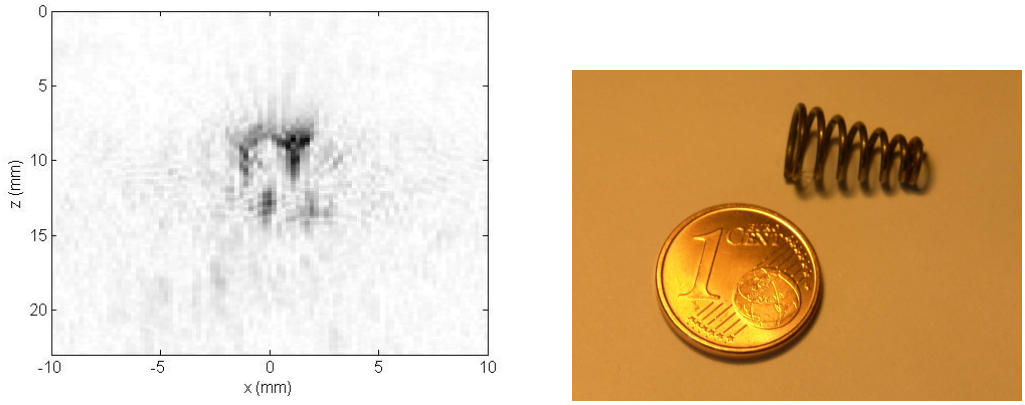

Figure IV.24.: FTA reconstructed PA image of a spring (on the right) embedded in an agar phantom under an incident angle of light of 35°. (The coin was not embedded.)

Additionally, some photoacoustic images of metal objects embedded in agar phantoms were taken. The first object was a spring depicted in figure IV.24. A grid, used as a second object, should give a first impression of the lateral resolution. The photoacoustic images illustrated in figure IV.25 show different sections with varying space. The different sized bars and spaces can be clearly seen and distinguished.

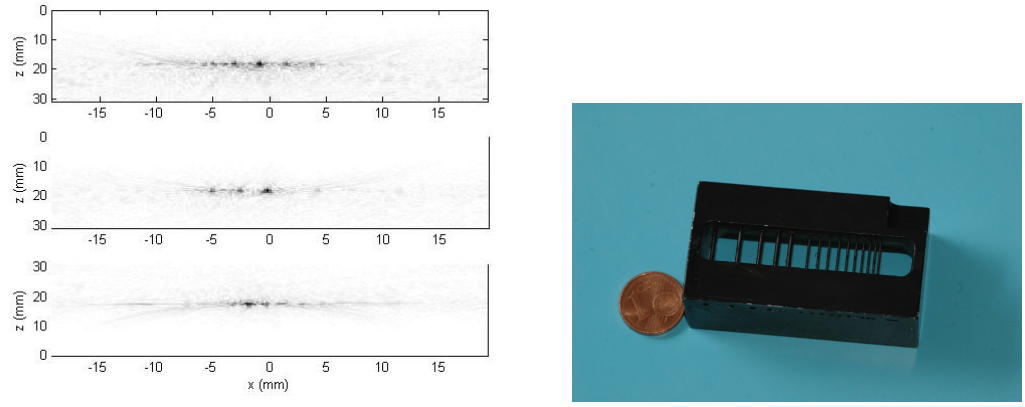

Figure IV.25.: FTA reconstructed PA images of a grid (depicted on the right) embedded in an agar phantom, larger spaces to small spaces from top to bottom measured under an incident angle of light of 50°. (The coin was not embedded.)

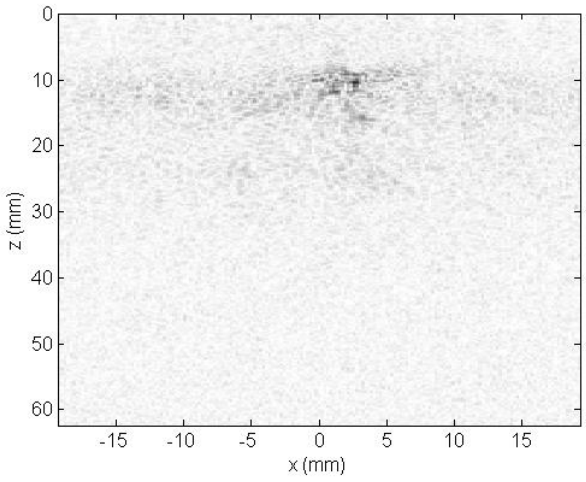

Figure IV.26.: PA image of a vein in a human forearm under an incident angle of light of 29° with a 12-mm agar layer as spacer.

3.2. Imaging of a human vein

As a first *in vivo* experiment, a vein in a human forearm was imaged. The vein is located closely under the skin. Since the laser beam cannot illuminate the tissue closely underneath the transducer, a 12-mm agar layer was placed as a spacer between the skin and the transducer to enable the illumination of the vein. The image was taken under an incident angle of light of 29°. The resulting image is illustrated in figure IV.26. The cross section of the vein is visible but with blurred outline.

3.3. Angular dependence

One of the characteristics of the OPUS system to be determined is the angular dependence. The angular dependency was tested with a PVA phantom depicted in figure IV.27 with channels (diameter 3 mm) implemented at different depths. The results with metal rods as absorbers at depths of 13 mm and 21 mm in non-scattering and scattering PVA was already shown in section 1.3. The same measurements were taken at depths 17 mm and 25 mm for ICG filled channels in non-scattering PVA.

One of the photoacoustic images of the ICG channels is shown in figure IV.28. The photoacoustic signal of the ICG and the bottom of the phantom were clearly visible

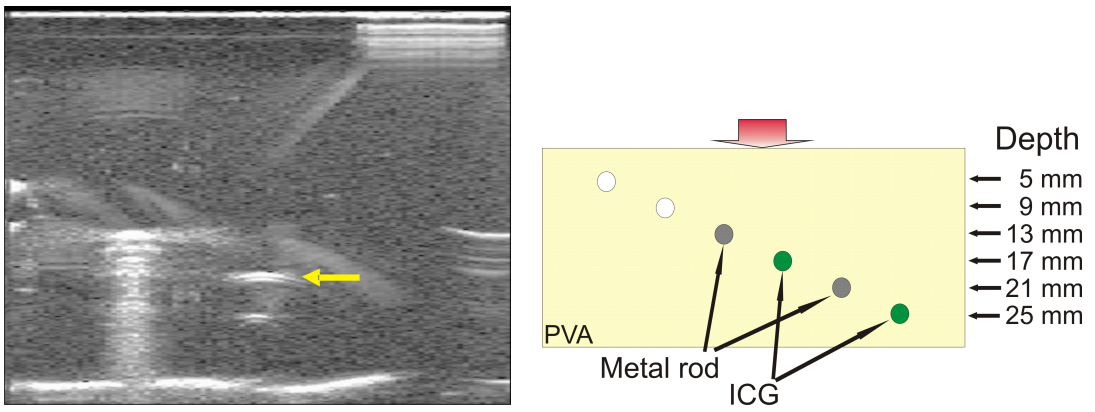

Figure IV.27.: Schematic of the phantom for the angular test with channels at different test filled with ICG or metal rods (right side). Ultrasound image of the phantom on the left side.

in the 2D image as well as in the signal measured by a single transducer element. The results for the angular dependence illustrated in figure IV.29 show closer peaks in contrast to the measurements with the metal rods. Furthermore, at 17 mm depth angles between 40° and 50° give highest intensities as well. For greater depths as 25 mm the highest intensity is reached at smaller angles, but would still be visible at 40°.

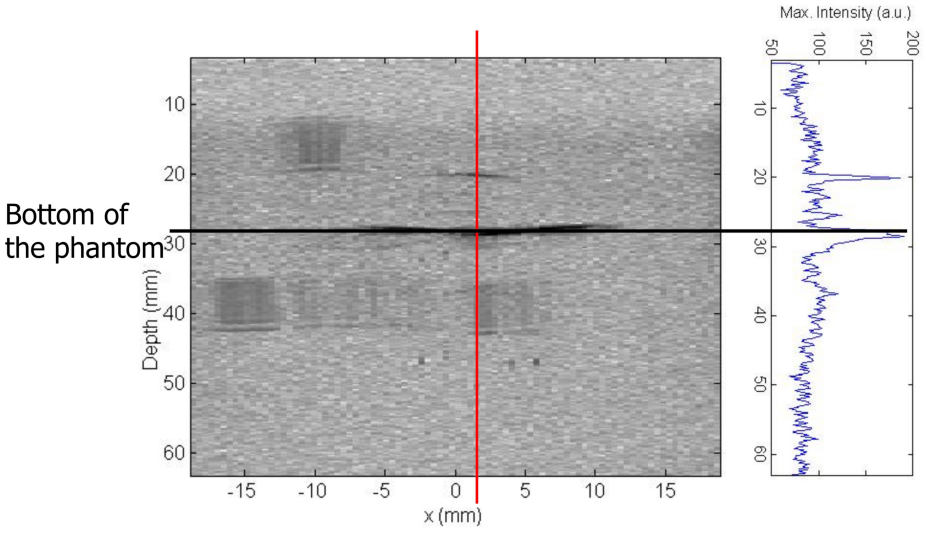

Figure IV.28.: Exemplarily photoacoustic image of ICG in a channel in an agar phantom and additionally, the photoacoustic signal measured by one single transducer element.

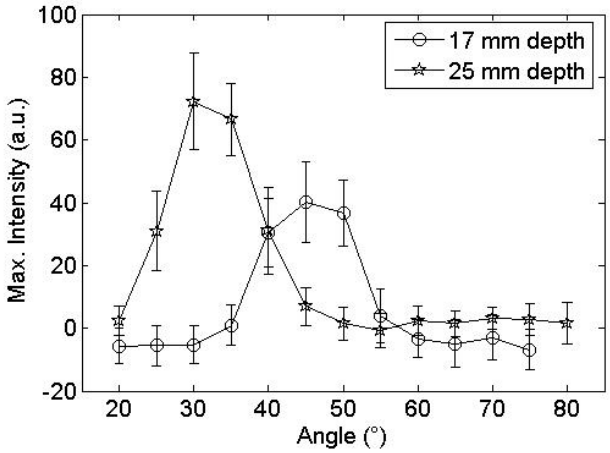

Figure IV.29.: Angular dependence of the photoacoustic signal of ICG in a non-scattering PVA phantom at depths of 17 mm and 25 mm.

4. Quantitative analysis

As discussed in section 3, the focus of photoacoustic tomography lies not mainly in the image generation but in the quantification of the tissue constituents, more precisely, the quantification of chromophore concentration and the determination

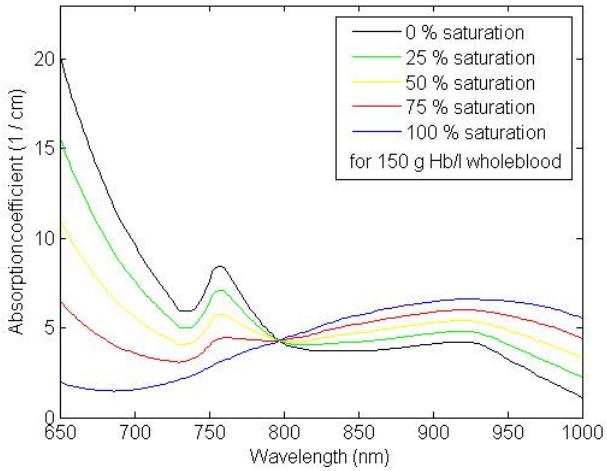

Figure IV.30.: Absorption spectra of hemoglobin at different oxygen saturation stats for 150 g Hb/l whole blood. (Data source: http://omlc.ogi.edu/spectra/hemoglobin/index.html, downloaded 19.November 2007)

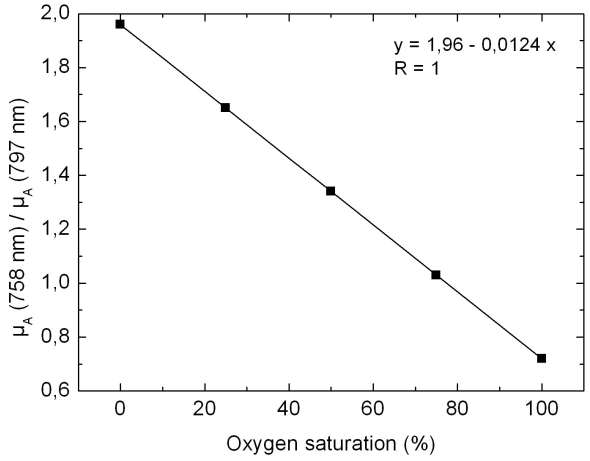

Figure IV.31.: Ratio of absorption coefficients at 758 nm and 797 nm versus oxygen saturation for 150 g Hb/l whole blood. (Data source: http://omlc.ogi.edu/spectra/hemoglobin/index.html, downloaded 19.November 2007)

of the oxygenation state of a certain chromophore, e.g., hemoglobin in whole blood. Since cancer may cause vascularization and higher oxygen consumption than in normal tissue [144], hemoglobin and its state of oxygenation in particular may give more detailed information about the constitution of a lump to reduce the number of biopsies. Hence, next to the photoacoustic imaging modality, this work deals with the capability of the OPUS system to quantify oxygen saturation states of blood.

Blood has a specific absorption spectrum for each level of oxygen saturation depending on the hemoglobin concentration. Figure IV.30 presents absorption spectra for a hemoglobin concentration of 150 g Hb/l for some oxygen saturation levels. (Data source: http://omlc.ogi.edu/spectra/hemoglobin/index.html, downloaded 19.November 2007).

One of the approaches for the quantification of blood oxygen saturation is the measurement at multiple wavelengths as already discussed in section 3. The ratio between two absorption coefficients at two different wavelengths is specific for each oxygen saturation level. Taking the ratio between two wavelengths for all saturations will lead to a regression line as it is shown for the ratio between 758 nm and 797 nm in figure IV.31. With the resulting linear equation an unknown saturation level can be determined by measuring the photoacoustic intensities at these two

wavelengths and calculating their ratio. Since the OPUS system is intended to be used for *in vivo* measurements, where the actual hemoglobin in the blood is probably not known, this approach may be promising and was therefore chosen to be tested, beginning with two wavelengths.

4.1. Sheep blood

Sheep blood was used for the first *in vitro* experiment with real blood. As phantom, a non-scattering PVA phantom, pierced with a channel of 3 mm diameter, was taken. Heparinized sheep blood with an oxygen saturation of 65 %± 10 % was pumped through the channel. The photoacoustic image as well as a schematic of the phantom can be seen in figure IV.32. The channel is visible although the contrast has been lower than with the dyes before, which may be caused by the rather high pulse-to-pulse energy fluctuations of the laser (SpitLight 600, laser generation I). Additionally, the image evaluation as described in this chapter was not yet developed at this point of the design.

The photoacoustic signal was determined at 760 nm, 800 nm, and 840 nm. The values obtained have been energy corrected. The results were compared with the absorption spectrum with an oxygen saturation of 65 % and presented in figure IV.33.

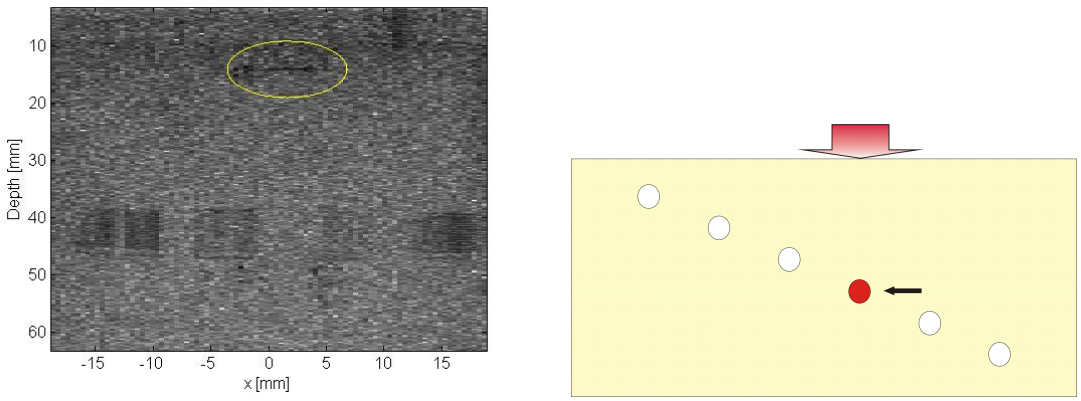

Figure IV.32.: Photoacoustic image of a channel (diameter 3 mm) pierced into a non-scattering PVA phantom and filled with heparinized sheep blood ($[O_2] = 65\% \pm 10\%$), measured at a wavelength of 769 nm under an incident angle of light of 45°. The right side shows a schematic of the PVA phantom.

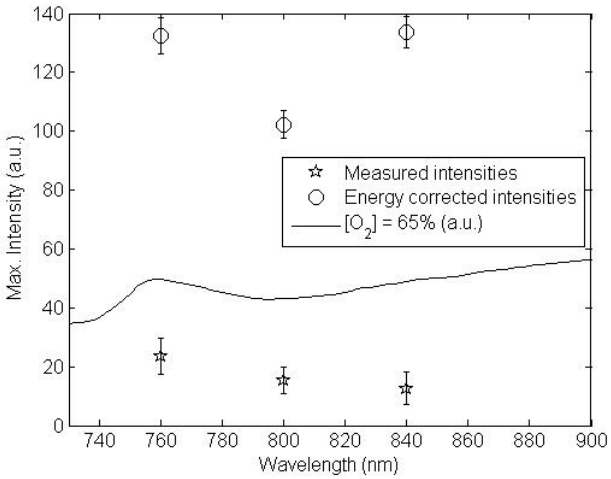

Figure IV.33.: Photoacoustic signals of sheep blood ($[O_2] = 65\% \pm 10\%$) measured at 760 nm, 800 nm, and 840 nm with and without energy correction as well as the absorption spectrum belonging to this saturation.

The corrected signals show a similar progression as the absorption spectrum. Calculating the ratio between the values at 760 nm and the isosbestic point at 800 nm results in an oxygen saturation of 54.4 %± 25.5 % which would fit with the origin saturation within the error range. The ratio between the values at 840 nm and at 800 nm gives a saturation of 115.3 %± 29.4 % which is physiologically impossible. This and the large errors may be caused by the high energy fluctuations, that are not monitored during the experiment. The photoacoustic values were corrected with energy mean values, that were typically meassured for this wavelengths.

4.2. Dye mixtures

With the second laser generation (SpitLight Hybrid), used for all of the following presented experiments, the energy fluctuation could be reduced from around 90 % to 32 %. Hence, the two wavelength measurements have been repeated with dye mixtures.

The absorption coefficients of ICG and Remazol Turquois have already been determined solitary and are presented in chapter III. For the measurements with the OPUS system, the dyes have been mixed in different ratios. While the con-

centration of ICG stayed the same, the concentration of Remazol Turquois has been varied. Afterwards, the ratio of the absorption at 711 nm to that of 780 nm was calculated from the single spectra and compared to the ratios determined by UV-Vis spectroscopy and by the OPUS system. The concentration ratios as well as the calculated and quantified results are presented in table IV.2. The ratios obtained by UV-Vis are slightly higher than the calculated ones but with the same trend with increasing turquois concentration. Between the calculated ratios and that determined photoacoustically no correlation could be found. Furthermore, the outputs of the photoacoustic experiments showed much lower ratios. One reason may be the fluorescence behavior of ICG, which is not totally known especially at this concentration and in combination with another dye. Another reason is, that the ICG diffuses into the channel walls of the phantom, which was observed at the end of the experiment and presumably bastardized the results.

Table IV.2.: Ratio of the intensities at 711 nm to those at 780 nm of dye mixtures from ICG and Remazol Turquois. From left to right: ratios of concentration, calculated ratios of the solitary data, ratios out of UV-Vis data and ratio out of photoacoustic data.

Dye mixture ICG/Turquois (mg L^{-1}) / (mg L^{-1})	Calculated values ICG/Turquois (a.u.)	UV-Vis ratio ICG/Turquois (a.u.)	PA ratio ICG/Turquois (a.u.)
30/100	0.531	0.562 ± 0.006	0.069 ± 0.045
30/300	0.637	0.694 ± 0.009	0.147 ± 0.106
30/350	0.663	0.683 ± 0.004	0.204 ± 0.077
30/370	0.673	0.697 ± 0.012	0.092 ± 0.062
30/390	0.684	0.721 ± 0.009	0.250 ± 0.117
30/400	0.689	0.722 ± 0.005	0.135 ± 0.059
0/100	9.786	-	0.512 ± 0.153
0/400	9.862	-	0.429 ± 0.396
30/0	0.478	-	0.224 ± 0.125

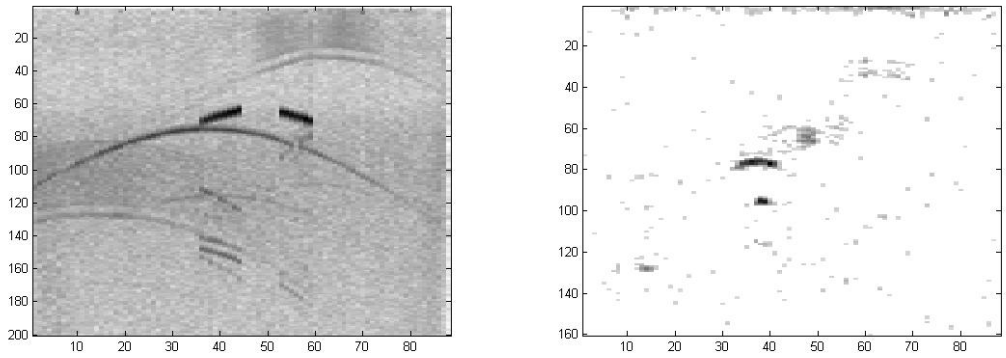

Figure IV.34.: Non-scattering PVA phantom with a channel (diameter 3mm) pierced at a depth of 13 mm and filled with a 50 mg L^{-1} ICG solution; photoacoustic raw data image (left) and reconstructed image (right).

4.3. ICG

Since the measurements with dye mixtures delivered no satisfying results, single dyes have been quantified, beginning with ICG.

For the experiments with ICG, a non-scattering PVA phantom was prepared with a channel of 3 mm diameter at a depth of 13 mm. The incidence angle of light was set to 50°. The ICG solution has been pumped through the channel with a volume rate of 2.25 ml s^{-1}. For this purpose, a thin-walled tube was pierced through the channel. For the energy correction, the energy of a reflex produced by the lens focusing the light on to the fiber was monitored during the experiment. Thus, both ends of the y-fiber were used for the illumination. A photoacoustic image of the ICG filled channel as well as the corresponding reconstructed image are illustrated in figure IV.34.

In a first experiment, a concentration series of ICG solutions between 5 mg L^{-1} and 50 mg L^{-1} has been measured at 780 nm and is depicted in figure IV.35 with the concentrations already translated into the corresponding absorption coefficients. The obtained and energy corrected intensities do not exhibit the expected linearity as it is known from UV-Vis, and have also large errors. The reason for the broad scattering around the regression line lies on one hand in air bubbles in the tubing crossing the experimental region. On the other hand, the energy correction cannot be executed exactly by allocating each photoacoustic A-line to its corresponding laser energy value. Hence, the energy was corrected by a mean value of the 88

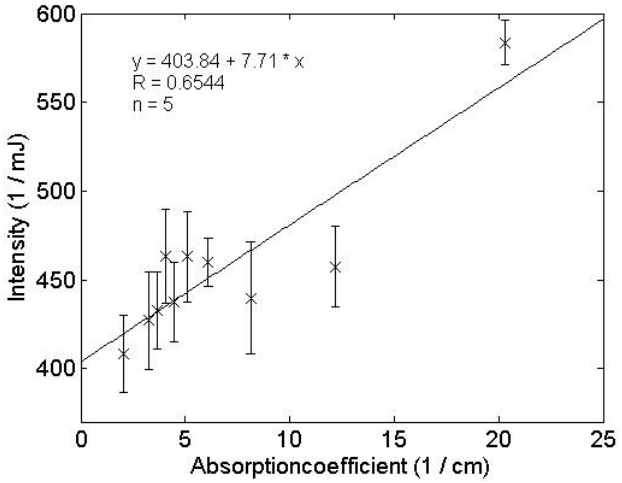

Figure IV.35.: Concentration series of a ICG solution photoacoustically measured in a non-scattering PVA phantom at 780 nm wavelength and 13 mm depth (50° incident angle of light).

laser shot energies needed for one image. However, comparing the corrected with the non-corrected energy data shows that this energy correction has only a slight influence on the spreading.

Additionally, the spectrum of a 50-mg-L^{-1} ICG solution was determined between 690 nm and 880 nm. The results presented in figure IV.36 show a similar trend as

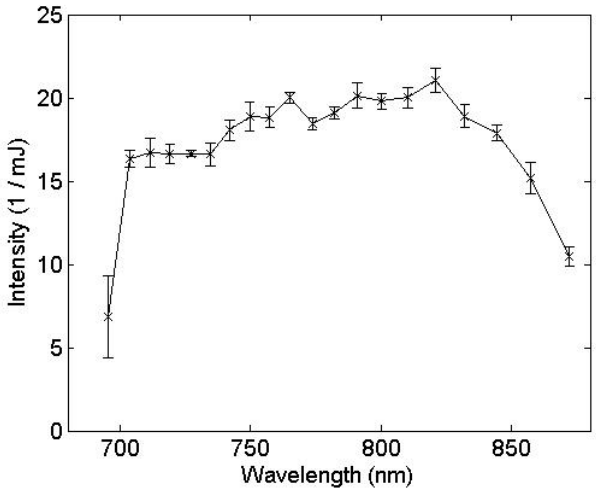

Figure IV.36.: Spectrum of a 50 mg L^{-1} ICG solution photoacoustically measured in a non-scattering PVA phantom at 13 mm depth (50° incident angle of light).

the spectrum measured by UV-Vis (see figure III.9), but the second maximum at 760 nm is not strongly pronounced. This may also deduced from the air bubbles in the tubing.

4.4. Black ink

Next to ICG, black ink was used for calibration measurements. The dye was pumped through flow channels (diameter 5 mm) pierced into non-scattering and scattering PVA phantoms to determine the dependency of the photoacoustic signal on the local extinction coefficient. The concentrations of the ink were chosen

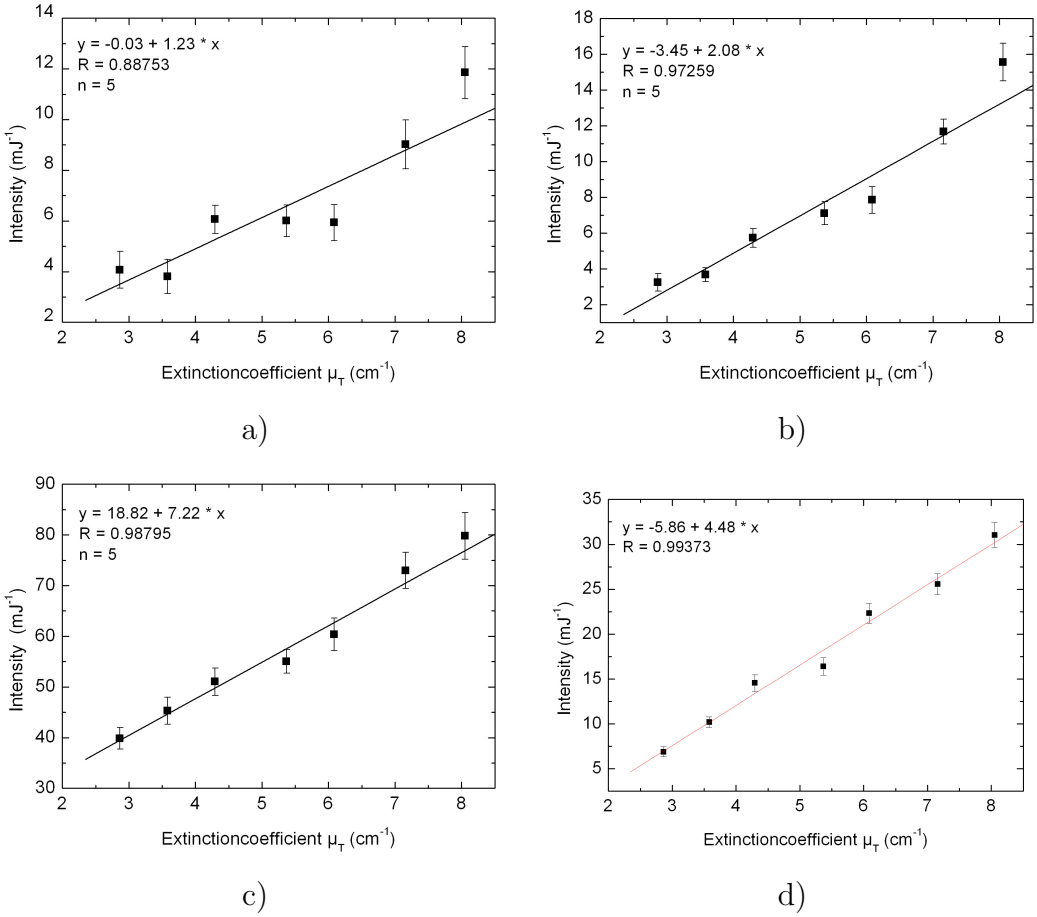

Figure IV.37.: Correlation between local extinction and photoacoustic signal, generated by different black ink concentrations in a channel in a PVA phantom a) 10 mm depth in scattering media, b) 15 mm depth in scattering media, c) 10 mm depth in non-scattering media, and d) 20 mm depth in non-scattering media.

Table IV.3.: Calibration measurements at different depths with black ink as absorber in scattering and non-scattering PVA.

Depth of absorber (mm)	Background scattering coefficient (cm^{-1})	Calibration slope (cm)	Distinguishable relative blood oxygenation (%)
10	0	7.22	8
10	61.1	1.23	14
20	0	4.48	8
15	61.1	2.08	9.5

corresponding to the range of blood absorptions at the measuring wavelength of 760 nm, where blood absorption is dependent on the oxygen saturation. The channel depths have been chosen at 10 mm in scattering and non-scattering phantom with an incident angle of light of 67° and for an angle of 45° at 15 mm in scattering and at 20 mm in non-scattering phantom.

The obtained data presented in figure IV.37 all show linear behavior. The corresponding slopes are listed in table IV.3. As to be expected, the slope is reduced for measurements in greater depth as well as in the scattering phantom. Since the intention is to distinguish between different states of oxygen saturation, to use the blood oxygenation as an indicator of metabolic activity, the measurements were taken at values corresponding to the blood absorption values at physiologically relevant blood oxygenations. The standard deviations of the measurements are a measure of the precision, that could be reached with the OPUS system when measuring blood oxygenation. The precision of the established instruments for this application is in the range of 3 % or better [145]. The evaluation of the data recorded by the OPUS system shows that a corresponding resolution of blood oxygenation of 8 % can be reached even at a depth of 20 mm, while the resolution is greatly reduced in the scattering samples (see table IV.3). The standard deviation is dependent on the energy fluctuations. For these measurements, the energy for the corrections was a mean value of eight values measured at one of the y-fiber ends during the experiment. Hence, the phantom was illuminated by one fiber end only and the energy fluctuation may still have a substancial influence on the standard deviation, and thereby, on the resolution.

5. Discussion

Since breast tumors may be located in depths of more than 5 mm, deep imaging is pivotal in breast cancer detection. Although photoacoustic imaging of tissue structures in human and animal experiments provided promising results [146, 147, 79, 148], imaging of structures deep in the tissue is still a challenge. For imaging large and thick tissues the backward imaging mode is used, leading to the question on the illumination geometry. M. Frenz describes in [149], that apart from noise, also reconstruction artifacts, backscattered photoacoustic transients, and random bulk tissue absorption are significant sources of image background in OA images. While the noise can be strongly reduced by averaging signals, the other sources are dependent on the illumination geometry, particularly on the distance between the linear transducer and the location of irradiation. Frenz demonstrated with simulations and experiments, that the optimum location of irradiation for deep photoacoustic imaging is not directly below, but beside the transducer aperture.

For the OPUS system an illumination along the side of the transducer was chosen. As reported in [149], point sources deeper in phantoms could be imaged using this illumination geometry. Furthermore, the OPUS system could even visualize depths up to 25 mm with variable incidence angle of light. These are greater depths as reported in [149].

A high SNR is required for quantitative analysis to distinguish between pixels carrying information and those that do not. With the averaging of five images the noise was reduced. On the other hand, the signal amplitude depends on the absorbed energy. Strong pulse-to-pulse fluctuations of a couple of tens percent cause significant variations in the signal amplitude. Hence, a reduction in the pulse-to-pulse fluctuations as well as the energy monitoring were aspired. For the first laser generations, an energy monitoring was performed to correct or rather to weight the amplitudes with the corresponding energy. In the process the single pulse monitoring turned out to be challenging. Since for low pulse-to-pulse fluctuations of a few percent the single pulse monitoring plays a decreasingly role the reduction of the laser energy fluctuation was placed into focus. The third laser generation was delivered in a late phase of this work. The energy characterization of the laser with the OPO could already be carried out and showed promising results. Although no further experiments could be performed using this laser, a further improvement of the SNR is to be expected. It could then be sufficient to correct the amplitudes by

known wavelength-energy correlations.

Another important aspect in imaging and visualizing a point source is the choice of the proper image reconstruction. All four methods presented in this work showed the ability of reconstructing point sources, but with different qualities especially with regard to depth. DnS and CBP give quite similar results, since they superimpose the same values, but in different order and with different limits. Compared to the other methods, the FWHM and the lateral resolution were worse, but maybe tolerable for some clinical applications. Their SNR are weak, but they are quite robust with respect to disturbances of the amplitude of single-lines. They suffer in computation speed, what makes them hard to implement in online controls.

HTA offers an adequate lateral resolution and SNR. As DnS and CBP, it shows a depth dependent FWHM accompanied by superposition artifacts. In some aspects as axial FWHM and lateral resolution, it presents similar results to FTA. But the long computation time does not allow real-time imaging either.

FTA reveals the best overall performance with the best SNR and an excellent, nearly depth independent FWHM. It computes fast for large images as well as for large numbers of images. FTA achieved an adequate peak-to-peak separation for shorter distances. No superposition artifacts were obtained. The only observed disadvantage is that the FTA seems to be more sensible to energy fluctuations. For strong fluctuations, this may lead to significant errors in quantitative analysis.

All four approaches show inferior results with real data acquired with the OPUS system than with high-resolution hydrophone measurements or simulations, that where presented in [49]. Although all methods would be in some way applicable for the OPUS system, FTA was found to be the best fitting photoacoustic pressure reconstruction method for the OPUS system. Since the implementation of a FTA algorithm would need grave changes in the user interface, it will be preliminary used for offline reconstruction. DnS was already satisfactorily tested for implementation, but was not useful for quantitative evaluations of the acquired data. The presented results are not absolute. They have to be interpreted in the context of the used setup.

Already the use of the first laser generation with the OPUS system and the FTA delivered promising results in imaging point sources, structures, veins, and liquids. The imaging of smaller structures is limited, based on the limited acoustical bandwidth of the transducers employed in commercial US systems. A center frequency

of 8.8 MHz, like the one in the OPUS system, neglects information encoded on the higher frequencies representing small-scale structures below about 200 μm. As a result of the limited transmission of these higher frequencies in tissue, this effect becomes relevant mostly for absorbing structures close to the surface. Strong damping of these high frequencies restricts the detection of fine-structured absorbers to a certain maximum depth, independent of the detector bandwidth.

In medical breast imaging, superficial structures are of less interest as the blood oxygen saturation. The first quantification at multiple wavelengths with real blood and dye mixtures delivered no satisfying results. The measurements with single dyes showed that a quantitative evaluation of absorption in media with unknown scattering and absorption are possible using the presented image evaluation and thresholding procedure. But the obtained results for the scattering phantoms are hardly sufficient for medical applications.

6. Conclusion

The aim of the presented work was to test the applicability of a combined ultrasound/photoacoustic (OPUS) system regarding its ability to reveal quantitative absorption information. This combination shall be a new tool for imaging, which provides additional imaging qualities beyond the pure ultrasound imaging. The photoacoustic imaging mode principally allows the extraction of quantitative optical absorption values from the image data. A linear relation between local optical absorption and photoacoustic signal was found for absorbers at different depths in scattering and non-scattering media employing suitable image reconstruction algorithms and quantification procedures. A chromophore concentration embedded in a matrix with unknown absorption and scattering properties cannot be determined by single wavelength measurements, but requires dual or multi-wavelength. The limited acoustical bandwidth of the US transducer employed in this study limits the spatial resolution of the system.

The OPUS system presents a promising new tool for medical imaging and quantitative analysis with the SpitLight Hybrid, and may be more effective with the all diode pumped laser system, due to its reduced energy fluctuations. The system shows similar or superior spatial resolution to other medical photoacoustic imaging systems, e.g., the Twente Photoacoustic Mammoscope [62]. A working depth of

about 2 cm is sufficient for most possible applications like breast cancer detection, which is the primary intended use of the OPUS system. The limited precision, regarding the sensitivity for blood oxygenation analysis, in the range of 10% is not sufficient for reliable measurements and medical applications. Optimized photoacoustic systems are able to measure with a precision of 3% or better [150]. The detection of sentinel lymph nodes labeled with commonly used dyes could be a promising application of an improved OPUS system. A common used practice to assess lymphatic metastasis is the examination of the first tumor-draining (sentinel) lymph node. In this case, a precise quantification is less relevant, and the general suitability of photoacoustic imaging for this application was proven by L. V. Wangs group [151]. They also employed tailor-made gold nanoparticles as high-absorption tracers [152], which could be very suitable for application with the OPUS system.

A limitation of the OPUS system is the relatively high pulse-to-pulse fluctuation of the employed tuneable laser systems of the generation I and II. The third laser generation SpitLight DPSS, a diode-pumped and diode-amplified laser system, offers a high stability, which was designed to improve the system performance. The first stability measurements showed promising results providing a way to improve the sensitivity for blood oxygen analysis. Additionally, employing a US system and US transducer, which allows the simultaneous readout of several or even all US channels, the SNR could be reduced significantly. Such a system would allow photoacoustic image generation with a much higher frame rate, thus, allowing averaging of many images in a reasonable exposure time to improve quantitative analytical application as well.

V. Summary

The tasks of the presented work were the development of the optoacoustic coupling between laser and ultrasound scanner, the designing and testing of phantoms for photoacoustic application, and the evaluation of the system.

Several phantom materials and absorbers have been tested with respect to their ability to mimic breast tissue. The phantom base materials Agar and PVA showed best mimicking abilities. While it was easy to find dyes with defined absorption for 532 nm wavelength, dyes absorbing in the working wavelength range of the OPUS system are difficult to quantify due to competitive processes as there are scattering (in ink) and fluorescence (in ICG). Nevertheless, black ink, ICG, and Remazol Turquois (which is weakly absorbing at these wavelengths) found their application in the first quantitative measurements.

The design for the coupling was chosen to enable deep imaging up to 2 cm, which was proven by resolution and depth tests. In this context, four reconstruction algorithms have been tried out regarding their ability to proper reconstruct point sources. The Fourier-Transformed-Algorithm turned out to have best overall performance in combination with the OPUS system. While the OPUS system demonstrates similar or superior spatial resolution to other medical photoacoustic imaging systems, its sensitivity for blood oxygen analysis, determined to be in the range of 10 %, is not yet sufficient for medical applications. A limitation is given by the high pulse-to-pulse fluctuations of the employed laser system, which can be overcome by a new design high-stability diode laser system.

A. Abbreviations

APS	Ammonium peroxodisulfate
BSE	Breast self-examination
CBE	Clinical breast examination
CBP	Circular backprojection
CT	Computer-tomography
cw	Continuous wave
DMSO	Dimethylsulfoxide
DnS	Delay-and-Sum
DFT	Discrete Fourier transform
FTA	Fourier transform algorithm
FWHM	Full width at half maximum
GPIB	General purpose interface bus
HTA	Generalized Hough transform algorithm
ICG	Indocyanine green
LOD	Limit of detection
LOIS	Laser optoacoustic imaging system
MRI	Magnetic resonance imaging
MZB	Maximum legal radiation
OA	Optoacoustic synonymous photoacoustic
OPO	Optical parametrical oscillator
OPUS	Optoacoutic Plus UltraSound
PA	Photoacoustic synonymous optoacoustic
PAA	Polyacrylamide
PAM	Photoacoustic Mammoscope
PET	Positron-emission-tomography

PVA	Polyvinyl alcohol
PVCP	Polyvinyl chloride-plastisol
PVDF	Polyvinylidene fluoride
RAL	Name of the RAL-color system
SNR	Signal-to-noise ratio
STD	Standard deviation
TEMED	Tetramethylethylendiamine
US	Ultrasound
UV	Ultraviolet
UV-Vis	Ultraviolet and visual spectrum

B. Symbols

A	Absorbance
A_{KM}	Kubelka-Munk absorption coefficient
α_s	Acoustic attenuation coefficient
β	Volume expansion coefficient
c	Velocity
c_0	Speed of sound
C_{p0}	Thermal capacity under constant pressure
c_L	Speed of light in vacuum
C_p	Specific heat at constant pressure
E	Energy
E_0	Excitation energy
E_a	Absorbed energy
E_t	Transmitted energy
E_{th}	Thermal energy
ϵ	Decadal molar extinction coefficient
F_S	Illuminated surface
g	Anisotropy factor
h	Planck constant
I	Reduced light intensity
I_0	Incident light intensity
λ	Wavelength
μ_a	Absorption coefficient
μ_s	Scattering coefficient
$\mu_s^{'}$	Reduced scattering coefficient
μ_t	Extinction coefficient

p	Pressure
Δp	Pressure change
ρ	Density
R	Reflection
R_a	Reflection coefficient
R_d	Diffuse reflection
S_{KM}	Kubelka-Munk scattering coefficient
T	Transmission
t_a	Acoustic relaxation time
T_a	Transmission coefficient
T_c	Collimated transmission
T_d	Diffuse transmission
T_t	Total transmission
t_χ	Duration that thermal energy needs to leave the probe element by diffusion
τ_L	Laser pulse duration
ΔT	Temperature change
V	Volume
V_0	Volume at equilibrium condition
ΔV	Volume expansion
χ	Thermal diffusivity
z	Depth
Z	Acoustic impedance
Δ	Laplace-Operator

Bibliography

[1] L.A.G. Ries, D. Harkins, and M. Krapcho. SEER cancer statistics review, 1975-2003. *National Cancer Institute*, 2006.

[2] C. Smigal, R. Siegel, and A. Jemal. Breast cancer facts and figures 2005-2006. *Amercian Cancer Society*, pages 1–30, 2006.

[3] C.H. Jones. Methods of breast imaging. *Phys Med Biol*, 27:463–499, 1982.

[4] R.E. Bird, T.W. Wallace, and B.C. Yankaskas. Analysis of cancers missed at screening mammography. *Radiology*, 184:613–617, 1992.

[5] V.P. Jackson, R.E. Hendricks, S.A. Feig, and D.B. Kopans. Imaging of the radiographically dense breast. *Radiology*, 188:297–301, 1993.

[6] L. Tabar and P.B. Dean. Mammographic parenchymal patterns: risk indicator for breast cancer. *J. Am. Med. Ass.*, 247:185–189, 1982.

[7] UNSCEAR (United Nations Scientific Committee on the Effects of Atomic Radiation). Sources and effects of ionizing radiation. 1994. (New York: United Nations).

[8] BEIR (Committee on the Biological Effects of Ionizing Radiations). *Health effects of exposure to low levels of ionizing radiation (BEIR V)*. National Academy Press, Washington, DC, 1990.

[9] J.J. Wild and D. Neal. Use of high-frequency ultrasonic waves for detecting changes of texture in living tissues. *The Lancet*, pages 655–657, 1951.

[10] J.C. Bamber and M. Tristam. *The principles of medical imaging: diagnostic ultrasound*. Hilger, Bristol, 1988.

[11] H. Kuttruff. *Physik und Technik des Ultraschalls*. S.Hirzel Verlag, Stuttgart, 1988.

[12] V.P. Jackson. The role of US in breast imaging. *Radiology*, 177:305–311, 1990.

[13] L.W. Bassett and C. Kimme-Smith. Breast sonography. *Am J Roentgenol*,

156.

[14] L.W. Bassett, C. Kimme-Smith, L.K. Sutherland, R.H. Gold, D. Sarti, and W. King. Automated and hand-held breast ultrasound: effect on patient management. *Radiology*, 165:103–108, 1987.

[15] M.O. Leach. *The principles of medical imaging: spacially localiced nuclear magnetic resonance*. Hilger, Bristol, 1988.

[16] J.H. Bernhardt. Non-ionizing radiation safety: radiofrequency radiation, electric and magnetic. *Phys Med Biol*, 37.

[17] R. Damadian. Tumor detection by nuclear magnetic resonance. *Science*, 171:1151–1153, 1971.

[18] S.J. El Yousef, D.M. O'Connell, R.H. Duchesneau, M.J. Smith, C.A. Hubay, and S.P. Guyton. Benign and malignant breast disease: magnetic resonance and radiofrequency pulse sequences. *Am J Roentgenol*, 145:1–8, 1985.

[19] S. Greenstein Orel and R.H. Troupin. Nonmammographic imaging of the breast: current issues and future prospects. *Semin Roentgenol*, XXVII.

[20] H. Wright, J. Listinsky, A. Rim, M. Chellman-Jeffers, R. Patrick, L. Rybicki, J. Kim, and J. Crowe. Magnetic resonance imaging as a diagnostic tool for breast cancer in premenopausal women. *Am J Surg*, 190:572–575, 2005.

[21] M. Saebel and H. Aichinger. Recent developments in breast imaging. *Phys Med Biol*, 41.

[22] E.C. Fear, S.C. Hagness, P.M. Meaney, M. Okoniewski, and M.A. Stuchly. Enhancing breast tumor detection with near-field imaging. *IEEE Microwave Magazine*, pages 48–56, 2002.

[23] B.W. Pogue, S.P. Poplack, T.O. McBride, W.A. Wells, K.S. Osterman, U.L. Osterberg, and K.D. Paulsen. Quantitative hemoglobin tomography with diffuse near-infrared spectroscopy: Pilot results in the breast. *Radiology*, 218.

[24] A.E. Cerussi, A.J. Berger, F. Bevilacqua, N. Shah, D. Jakubowski, J. Butler, R.F. Holcombe, and B.J. Tromberg. Sources of absorption and scattering contrast for near-infrared optical mammography. *Acad Radiol*, 8.

[25] N. Shah, A. Cerussi, C. Eker, J. Espinoza, J. Butler, J. Fishkin, R. Hornung, and B. Tromberg. Noninvasive functional optical spectroscopy of human breast tissue. *P Natl Acad Sci USA*, 98.

[26] S.B. Colak, M.B. van der Mark, G.W. Hooft, J.H. Hoogenraad, E.S. van der

Linden, and F.A. Kuijpers. Clinical optical tomography and NIR spectroscopy for breast cancer detection. *IEEE J Sel Top Quant*, 5.

[27] S.A. Ermilov, A. Stein, A. Conjusteau, R. Gharieb, R. Lacewell, T. Miller, S. Thompson, P. Otto, B. McCorvey, T. Khamapirad, M. Leonard, and A.A. Oraevsky. Detection and noninvasive diagnostics of breast cancer with two-color laser optoacoustic imaging system. *Proc. of SPIE*, 6437:643703–1–643703–11, 2007.

[28] S.A. Ermilov, R. Gharieb, A. Conjusteau, T. Miller, K. Mehta, and A.A. Oraevsky. Data processing and quasi-3d optoacoustic imaging of tumors in the breast using a linear arc-shaped array of ultrasonic transducers. *Proc. of SPIE*, 6856:685603/1–685603/10, 2008.

[29] S. Manohar, A. Kharine, C.G. van Hespen Johan, W. Steenbergen, and G. van Leeuwen Ton. Photoacoustic mammography laboratory prototype: imaging of breast tissue phantoms. *J Biomed Opt*, 9.

[30] S.E. Vaartjes, J.C.G. Van Hespen, J.M. Klaase, F.M. Van den Engh, A.K.H. Thé, T.G. Van Leeuwen, and S. Manohar. First clinical trials of the twente photoacoustic mammoscope (pam). *Proc. of SPIE*, 6629:662917/1–662917/12, 2007.

[31] A.G. Bell. The photophone. *Science*, 1.

[32] A.G. Bell. On the production and reproduction of sound by light. *Am J Sci*, 20:305–324, 1880.

[33] A.G. Bell. Upon a modification of weatstone's microphone, and its adaptability to radiophonic researchers. *Science*, 2:314–315, 1881.

[34] A.G. Bell. The production of sound by radiant energy. *Science*, 2.

[35] J. Tyndall. Actions of an intermittent beam of radiant heat upon gasous matter. *Proc. Roy. Soc. London*, 31:307–317, 1881.

[36] W.C. Röntgen. On tones produced by the intermittent irradiation of a gas. *Philos. Mag.*, 11:308–311, 1881.

[37] A. Rosencwaig. Potential clinical applications of photoacoustics. *Clin Chem*, 28.

[38] T.H. Maugh. Photoacoustic spectroscopy: New uses for an old technique. *Science*, 188.

[39] J.F. McClelland. Photoacoustic spectroscopy. *Anal Chem*, 55.

[40] D. McLean, H. Sauren, L.R. Walker, and J.K.S. Wan. A portable piezoelectric detector for pulsed laser optoacoustic studies of free radicals. *Sensor Actuat B*, 17:149–156, 1994.

[41] A. Miklos, P. Hess, and Z. Bozoki. Application of acoustic resonators in photoacoustic trace gas analysis and metrology. *Rev Sci Instrum*, 72.

[42] A. Rosencwaig. Photoacoustic spectroscopy of biological materials. *Science*, 181.

[43] T.D. Khokhlova, I.M. Pelivanov, and A.A. Karabutov. Optoacoustic tomography utilizing focused transducers: the resolution study. *Appl Phys Lett*, 92, 2008.

[44] P.C. Beard and T.N. Mills. An optical detection system for biomedical photoacoustic imaging. *Proc. of SPIE*, 3916:100–109, 2000.

[45] P.C. Beard and T.N. Mills. A 2D optical ultrasound array using a polymer film sensing interferometer. *IEEE Ultrasonics Symposium*, pages 1183–1186, 2000.

[46] E. Zhang, J. Laufer, and P. Beard. Backward-mode multiwavelength photoacoustic scanner using a planar fabry-perot polymer film ultrasound sensor for high-resolution three-dimensional imaging of biological tissues. *Appl Opt*, 47.

[47] A. Elia, P.M. Lugarà, C.D. Franco, and V. Spagnolo. Photoacoustic techniques for trace gas sensing based on semiconductor laser sources. *Sensors*, 9:9616–9628, 2009.

[48] C. Haisch, H. Beck, and R. Niessner. Photoacoustic sensor system for the quantification of soot aerosols. *Rev Sci Instrum*, 74.

[49] J.I. Sperl, K. Zell, P. Menzenbach, C. Haisch, S. Ketzer, M. Marquart, H. Koenig, and M.W. Vogel. Photoacoustic image reconstruction: A quantitative analysis. *Proc. of SPIE*, 6631:663103, 2007.

[50] Safety of laser products - part1: Equipment classification, requirements and user's guide, October 2003.

[51] Medical electrical equipment - part 2: Particular requirements for the safety of diagnostic and therapeutic laser equipment, December 1996.

[52] C. Haisch, L. Hoffmann, and R. Niessner. Design and characterization of a highly directional photoacoustic sensor probe. *Proc. SPIE*, 6086:60860E/1–E/10, 2006.

[53] E. Hecht. *Optik*. Oldenburg Verlag, 2005.

[54] S.A. Prahl, M. Keijzer, S.L. Jacques, and A.J. Welch. A monte carlo model of light propagation in tissue. *SPIE Institute Series*, IS 5:102–111, 1989.

[55] A.A. Karabutov, N.B. Podymova, and V.S. Letokhov. Time-resolved laser optoacoustic tomography of inhomogenenous media. *Appl Phys B*, 63:545–563, 1996.

[56] C.K.N. Patel and A.C. Tam. Pulsed optoacoustic spectroscopy of condensed matter. *Rev Mod Phys*, 53.

[57] H. Kuchling. *Taschenbuch der Physik*. Fachbuchverlag, Leipzig, Koeln, 1995.

[58] V.E. Gusev and A.A. Karabutov. *Laser optoacoustics*. AIP Press, New York, 1993.

[59] J.J. Niederhauser, M. Jaeger, R. Lemor, P. Weber, and M. Frenz. Combined ultrasound and optoacoustic system for real-time high-contrast vascular imaging in vivo. *IEEE T Med Imaging*, 24.

[60] L. Jankovic, K. Shahzad, Y. Wang, M. Burcher, F.-D. Scholle, P. Hauff, S. Mofina, and M. Skobe. A modified commercial ultrasound scanner used for in vivo photoacoustic imaging of nude mice injected with non-targeted contrast agents. *Proc. of SPIE*, 6856:68560O/1–68560O/9, 2008.

[61] L. Jankovic, K. Shahzad, Y. Wang, M. Burcher, F.-D. Scholle, P. Hauff, S. Mofina, and M. Skobe. In vivo photoacoustic imaging of nude mice vasculature using a photoacoustic imaging system based on a commercial ultrasound scanner. *Proc. of SPIE*, 6856:68560N/1–68560N/12, 2008.

[62] S. Manohar, A. Kharine, C.G. van Hespen Johan, W. Steenbergen, and G. van Leeuwen Ton. The Twente photoacoustic mammoscope: System overview and performance. *Phys Med Biol*, 50.

[63] V.G. Andreev, A.A. Karabutov, S.V. Solomatin, E.V. Savateeva, V. Aleynikov, Y.V. Zhulina, and A.A. Oraevsky. Opto-acoustic tomography of breast cancer with an arc-array-transducer. *Proc. of SPIE*, 3916:36–47, 2000.

[64] A.A. Oraevsky, A.A. Karabutov, S.V. Solomatin, E.V. Savateeva, V.G. Andreev, Z. Gatalica, H. Singh, and R.D. Fleming. Laser optoacoustic imaging of breast cancer in vivo. *Proc. of SPIE*, 4256:6–15, 2001.

[65] A.A. Oraevsky, E.V. Savateeva, S.V. Solomatin, A.A. Karabutov, V.G. An-

dreev, Z. Gatalica, T. Khamapirad, and P.M. Henrichs. Optoacoustic imaging of blood, for visualization and diagnostics of breast cancer. *Proc. of SPIE*, 4618:81–94, 2002.

[66] G.M. Spirou, I.A. Vitkin, B.C. Wilson, W.M. Whelan, P.M. Henrichs, K. Metha, T. Miller, A. Yee, J. Meador, and A.A. Oraevsky. Development and testing of an optoacoustic imaging system for monitoring and guiding prostate cancer therapies. *Proc. of SPIE*, 5320:44–56, 2004.

[67] S.A. Ermilov, A. Conjusteau, K. Mehta, R. Lacewell, P.M. Henrichs, and A.A. Oraevsky. 128-channel laser optoacoustic imaging system (lois-128) for breast cancer diagnostics. *Proc. of SPIE*, 6086:608609/1–608609/12, 2006.

[68] P.C. Beard. Photoacoustic imaging of blood vessel equivalent phantoms. *Proc. of SPIE*, 4618:54–62, 2002.

[69] P.C. Beard, E.Z. Zhang, and B.T. Cox. Transparent Fabry Perot polymer film using ultrasound array for backward-mode photoacoustic imaging. *Proc. SPIE*, 5320:230–237, 2004.

[70] E.Z. Zhang and P. Beard. 2D backward-mode photoacoustic imaging system for nir (650-1200nm) spectroscopic biomedical applications. *Proc. of SPIE*, 6086:60860H/1–60860H/8, 2006.

[71] E.Z. Zhang and P. Beard. Broadband ultrasound field mapping system using a wavelength tuned, optically scanned focused laser beam to address a fabry perot polymer film sensor. *IEEE Translations on Ultrasonics, Ferroelectrics, and Frequency Control*, 53.

[72] E.Z. Zhang, J. Laufer, R.B. Pedley, and P. Beard. 3D photoacoustic imaging system for in vivo studies of small animal models. *Proc. of SPIE*, 6856:68560P/1–68560P/8, 2008.

[73] J. Laufer, P. Johnson, E. Zhang, B. Treeby, B. Cox, B. Pedley, and P. Beard. In vivo longitudinal photoacoustic imaging of subcutaneous tumours in mice. *Proc. of SPIE*, 7899:789915–1–789915–6, 2011.

[74] X. Yang and L.V. Wang. Photoacoustic tomography of a rat cerebral cortex with a ring-based ultrasonic virtual point detector. *J Biomed Opt*, 12.

[75] J. Gamelin, A. Aguirre, A. Maurudis, F. Huang, D. Castillo, L.V. Wang, and Q. Zhu. Small animal imaging using a curved array photoacoustic tomography system. *Proc. of SPIE*, 6856:68560Q/1–68560Q/10, 2008.

[76] K.H. Song, G. Stoica, and L.V. Wang. Three-dimensional in vivo near-infrared photoacoustic tomography of whole small animal head. *Proc. of SPIE*, 6086:60860Q/1–60860Q/7, 2006.

[77] G. Ku, X.D. Wang, G. Stoica, and L.H.V. Wang. Multiple-bandwidth photoacoustic tomography. *Phys Med Biol*, 49.

[78] K. Maslov and L.V. Wang. Photoacoustic imaging of biological tissue with intensity-modulated continuous-wave laser. *J Biomed Opt*, 13.

[79] X.D. Wang, X.Y. Xie, G.N. Ku, and L.H.V. Wang. Noninvasive imaging of hemoglobin concentration and oxygenation in the rat brain using high-resolution photoacoustic tomography. *J Biomed Opt*, 11.

[80] C. Haisch. Quantitative analysis in medicine using photoacoustic tomography. *Anal Bioanal Chem*, 393:473–479, 2009.

[81] M. Jaeger, M. Frenz, and D. Schweizer. Iterative reconstruction algorithm for reduction of echo background in optoacoustic images. *Proc. of SPIE*, 6856:68561C/1–68561C/15, 2008.

[82] M.H. Xu and L.H.V. Wang. Pulsed-microwave-induced thermoacoustic tomography: filtered backprojection in a circular measurement configuration. *Med Phys*, 29.

[83] X. Wang, Y. Xu, M. Xu, S. Yokoo, E.S. Fry, and L.V. Wang. Photoacoustic tomography of biological tissues with high cross-section resolution: reconstruction and experiment. *Med Phys*, 29.

[84] B.Z. Yin, D. Xing, Y. Wang, Y.G. Zeng, Y.G. Zeng, Y. Tan, and Q. Chen. Fast photoacoustic imaging system based on 320-element linear transducer array. *Phys Med Biol*, 49.

[85] M.A. Anastasion, J. Zhang, D. Modgil, and P.J. La Rivière. Application of inverse source concepts to photoacoustic tomography. *Inverse Probl*, 23:S21–S35, 2007.

[86] K.P. Koestli and P.C. Beard. Two-dimensional photoacoustic imaging by use of fourier-transform image reconstruction and a detector with an anisotropic response. *Appl Opt*, 42.

[87] M.H. Xu and L.H.V. Wang. Photoacoustic imaging in biomedicine. *Rev Sci Instrum*, 77.

[88] M. Sivaramakrishnan, K. Maslov, H.F. Zhang, G. Stoica, and L.V. Wang.

Limitations of quantitative photoacoustic measurements of blood oxygenation in small vessels. *Phys Med Biol*, 52.

[89] R.O. Esenaliev, I.V. Larina, K.V. Larin, D.J. Deyo, M. Motamedi, and D.S. Prough. Optoacoustic technique for noninvasive monitoring of blood oxygenation: A feasibility study. *Appl Opt*, 41.

[90] H.P. Brecht, D.S. Prough, Y.Y. Petrov, I. Patrikeev, I.Y. Petrova, D.J. Deyo, I. Cicenaite, and R.O. Esenaliev. In vivo monitoring of blood oxygenation in large veins with a triple-wavelength optoacoustic system. *Optics Express*, 15.

[91] K. Maslov, M. Sivaramakrishnan, H.F. Zhang, G. Stoica, and L.V. Wang. Technical considerations in quantitative blood oxygenation measurement using photoacoustic microscopy in vivo. *Proc. of SPIE*, 6086:60860R/1–60860R/11, 2006.

[92] R.J. Zemp, L. Li, and L.V. Wang. Fundamental considerations for multiwavelength photoacoustic molecular imaging. *Proc. of SPIE*, 6086:60861L/1–60861L/9, 2006.

[93] B.T. Cox, S.R. Arridge, and P.C. Beard. Quantitative photoacoustic image reconstruction for molecular imaging. *Proc. of SPIE*, 6086:60861M/1–60861M/9, 2006.

[94] L.H. Wang, S.L. Jacques, and L.Q. Zheng. MCML - Monte carlo modeling of light transport in multilayered tissues. *Comput Meth Prog Bio*, 47.

[95] B.T. Cox, S.R. Arridge, K.P. Koestli, and P.C. Beard. Two-dimensional quantitative photoacoustic image reconstruction of absorption distributions in scattering media by use of a simple iterative method. *Appl Opt*, 45.

[96] W. Cong, H. Shen, A. Cong, Y. Wang, and G. Wang. Modeling photon propagation in biological tissues using a generalized delta-eddington phase function. *Phys Rev E*, 76.

[97] J. Laufer, C. Elwell, D. Delphy, and P.C. Beard. Absolut measurement of local chromophore concentrations using pulsed photoacoustic spectroscopy. *Proc. of SPIE*, 6086:60861J/1–60861J/8, 2006.

[98] J. Laufer, D. Delpy, C. Elwell, and P. Beard. Quantitative spatially resolved measurement of tissue chromophore concentrations using photoacoustic spectroscopy: application to the measurement of blood oxygenation and haemoglobin concentration. *Phys Med Biol*, 52:141–168, 2007.

[99] B.T. Cox, S. Kara, S.R. Arridge, and P.C. Beard. k-space propagation models for acoustically heterogeneous media: Application to biomedical photoacoustics. *J Acoust Soc Am*, 121.

[100] S. Manohar, R.G.H. Willemink, F. van der Heijden, C.H. Slump, and T.G. van Leeuwen. Concomitant speed-of-sound tomography in photoacoustic imaging. *Appl Phys Lett*, 91.

[101] E.L. Madsen, G.R. Frank, and F. Dong. Liquid or solid ultrasonically tissue-mimicking materials with very low scatter. *Ultrasound Med Bio*, 24.

[102] M.M. Doyley, J.C. Bamber, F. Fuechsel, and N.L. Bush. A freehand elastographic imaging approach for clinical breast imaging: system development and performance evaluation. *Ultrasound Med Bio*, 27.

[103] E.L. Madsen, M.A. Hobson, G.R. Frank, H. Shi, J. Jiang, T.J. Hall, T. Varghese, M.M. Doyley, and J.B. Weaver. Anthropomorphic breast phantoms for testing elastograhy systems. *Ultrasound Med Bio*, 32.

[104] J.A. Viator and S.A. Prahl. Photoacoustic imaging of gelatin phantoms using matched field processing. *Proc. SPIE*, 3601:276–283, 1999.

[105] H.J. Van Staveren, C.J.M. Moes, J. Van Marle, S.A. Prahl, and M.J.C. Van Gemert. Light scattering in intralipid-10% in the wavelength range of 400-1100 nm. *Appl Opt*, 30.

[106] N. Ghosh, H.S. Patel, and P.K. Gupta. Depolarization of light in tissue phantoms - effect of a distribution in the size of scatterers. *Optics Express*, 11.

[107] T. Xu, C. Zhang, X. Wang, L. Zhang, and J. Tian. Measurement and analysis of light distribution in intralipid-10% at 650 nm. *Appl Opt*, 42.

[108] R.J. Hunter, M.S. Patterson, T.J. Farrell, and J.E. Hayward. Haemoglobin oxygenation of a two-layer tissue-simulating phantom from time-resolved reflectance: effect of top layer thickness. *Phys Med Biol*, 47.

[109] C.J.M. Moes, M.J.C. Van Gemert, W.M. Star, J.P.A. Marijnissen, and S.A. Prahl. Measurements and calculations of the energy fluence rate in a scattering and absorbing phantom at 633 nm. *Appl Opt*, 28.

[110] J.J. Rownd, E.L. Madsen, J.A. Zagzebski, G.R. Frank, and F. Dong. Phantoms and automated system for testing the resolution of ultrasound scanners. *Ultrasound Med Bio*, 23.

[111] R. Cubeddu, A. Pifferi, P. Taroni, A. Torricelli, and G. Valentini. Time-resolved imaging on a realistic tissue phantom: ms* and ma images versus time-integrated images. *Appl Opt*, 35.

[112] R. Cubeddu, A. Pifferi, P. Taroni, A. Torricelli, and G. Valentini. A solid tissue phantom for photon migration studies. *Phys Med Biol*, 42:1971–1979, 1997.

[113] S. Tanosaki, H. Taniguchi, K. Tsujita, B. Devaraj, and H. Inaba. Highly scattering intralipid-10% assisted lasing from microdroplets with acridine orange dye. *Appl Opt*, 37.

[114] K. Takegami, Y. Kaneko, T. Watanabe, T. Maruyama, Y. Matsumoto, and H. Nagawa. Polyacrylamide gel containing egg white as new model for irradiation experiments using focused ultrasound. *Ultrasound Med Bio*, 30.

[115] S. Howard, J. Yuen, P. Wegner, and C.I. Zanelli. Characterization and FEA simulation for a HIFU phantom material. *IEEE Ultrasonics Symposium*, pages 1270–1273, 2003.

[116] C. Lafon, V. Zderic, L. Noble Misty, C. Yuen Jonathan, J. Kaczkowski Peter, A. Sapozhnikov Oleg, F. Chavrier, A. Crum Lawrence, and S. Vaezy. Gel phantom for use in high-intensity focused ultrasound dosimetry. *Ultrasound Med Bio*, 31.

[117] A. Kharine, S. Manohar, R. Seeton, G.M. Kolkman Roy, A. Bolt Rene, W. Steenbergen, and F.M. de Mul Frits. Poly(vinyl alcohol) gels for use as tissue phantoms in photoacoustic mammography. *Phys Med Biol*, 48.

[118] C.U. Devi, R.M. Vasu, and A.K. Sood. Design, fabrication, and characterization of a tissue-equivalent phantom for optical elastography. *J Biomed Opt*, 10.

[119] K.J.M. Surry, H.J.B. Austin, A. Fenster, and T.M. Peters. Poly(vinyl alcohol) cryogel phantoms for use in ultrasound and mr imaging. *Phys Med Biol*, 49.

[120] M. Firbank and D.T. Delpy. A design for a stable and reproducible phantom for use in near infra-red imaging and spectroscopy. *Phys Med Biol*, 38:847–853, 1993.

[121] M. Firbank, M. Oda, and D.T. Delpy. An improved design for a stable and reproducible phantom material for use in near-infrared spectroscopy and imaging. *Phys Med Biol*, 40:955–961, 1995.

[122] J.C. Hebden, D.J. Hall, M. Firbank, and D.T. Delpy. Time-resolved optical imaging of a solid tissue-equivalent phantom. *Appl Opt*, 34.

[123] R. Srinivasan, D. Kumar, and M. Singh. Optical tissue-equivalent phantoms for medical imaging. *Trends Biomater. Artif. Organs*, 15.

[124] G.M. Spirou, A.A. Oraevsky, I.A. Vitkin, and W.M. Whelan. Optical and acoustic properties at 1064 nm of polyvinyl chloride-plastisol for use as a tissue phantom in biomedical optoacoustics. *Phys Med Biol*, 50:N141–N153, 2005.

[125] S.H. Hyon, W.I. Cha, and Y. Ikada. Preparation of transparent poly(vinyl-alcohol) hydrogel. *Polym Bull*, 22.

[126] M. Friedman. Chemistry, biochemistry, and safety of acrylamide: A review. *J Agr Food Chem*, 51.

[127] J.C. Bamber, editor. *Acoustical characterisation of biological media encyclopedia of acoustics*. Wiley, New York.

[128] H.K. Park, D. Kim, C.P. Grigoropoulos, and A.C. Tam. Pressure generation and measurement in the rapid vaporization of water on a pulsed-laser-heated surface. *J Appl Phys*, 80.

[129] J.J. Markham, R.T. Beyer, and R.B. Lindsay. Absorption of sound in fluids. *Rev Mod Phys*, 23:353–411, 1951.

[130] F.A. Duck. *Physical properties of tissue: A comprehensive reference book*. Academic, London, 1990.

[131] J.E. Browne, K.V. Ramnarine, A.J. Watson, and P.R. Hoskins. Assessment of the acoustic properties of common tissue-mimicking test phantoms. *Ultrasound Med Bio*, 29.

[132] A.F. Prokop, S. Vaezy, M.L. Noble, P.J. Kaczkowski, R.W. Martin, and L.A. Crum. Polyacrylamide gel as an acoustic coupling medium for focused ultrasound therapy. *Ultrasound Med Bio*, 29.

[133] W.-F. Cheong, S.A. Prahl, and A.J. Welch. A review of the optical properties of biological tissues. *IEEE Journal of Quantum Elektronics*, 26.

[134] W.M. Star, J.P. Marijnissen, and M.J. van Gemert. Light dosimetry in optical phantoms and in tissues: I. multiple flux and transport theory. *Phys Med Biol*, 33.

[135] R. Winter and F. Noll. *Methoden der Biophysikalischen Chemie*. Teubner

Studienbücher, Stuttgart, 1998.

[136] T. Schmid, C. Helmbrecht, U. Panne, C. Haisch, and R. Niessner. Process analysis of biofilms by photoacoustic spectroscopy. *Anal Bioanal Chem*, 375.

[137] C.G.A. Hoelen, F.F.M. de Mul, R. Pongers, and A. Dekker. Three-dimensional photoacoustic imaging of blood vessels in tissue. *Opt Lett*, 23.

[138] R.A. Kruger, K.D. Miller, H.E. Reynolds, W.L. Kiser, D.R. Reinecke, and G.A. Kruger. Breast cancer in vivo: contrast enhancement with thermoacoustic ct at 434 mhz - feasibility study. *Radiology*, 216.

[139] C.G.A. Hoelen and F.F.M. de Mul. Image reconstruction for photoacoustic scanning of tissue structures. *Appl Opt*, 39.

[140] G. Paltauf, J. Viator, S. Prahl, and S. Jaques. Iterative reconstruction method for three-dimensional optoacoustic imaging. *Proc. of SPIE*, 4256:138–146, 2001.

[141] M. Anastasion and J. Zhang. Image reconstruction in thermoacoustic tomography with compensation for acoustic heterogeneities. *Proc. of SPIE*, 5750:298–304, 2005.

[142] R. Duda and P. Hart. Use of the hough transformation to detect lines and curves in pictures. *Communications of the ACM*, 15:11–15, 1972.

[143] B.T. Cox, J. Laufer, K. Koestli, and P.C. Beard. Experimental validation of photoacoustic k-space propagation models. *Proc. of SPIE*, 5320:238–248, 2004.

[144] X. Cheng, J. Mao, R. Bush, D.B. Kopans, R.H. Moore, and M. Chorlton. Breast cancer detection by mapping hemoglobin concentration and oxygen saturation. *Appl Opt*, 42.

[145] A. van de Louw, C. Cracco, C. Cerf, A. Harf, P. Duvaldestin, F. Lemaire, and L. Brochard. Accuracy of pulse oximetry in the intensive care unit. *Intensive Care Med*, 27:1606–1613, 2001.

[146] R.I. Siphanto, K.K. Thumma, R.G.M. Kolkman, T.G. van Leeuwen, F.F.M. de Mul, J.W. van Neck, L.N.A. van Adrichem, and W. Steenbergen. Serial noninvasive photoacoustic imaging of neovascularization in tumor angiogenesis. *Optics Express*, 13.

[147] X. Wang, Y. Pang, G. Ku, G. Stoica, and L.V. Wang. Three-dimensional laser-induced photoacoustic tomography of mouse brain with the skin and

skull intact. *Opt Lett*, 28:1739–1741, 2003.

[148] Y.W. Wang, X.Y. Xie, X.D. Wang, G. Ku, K.L. Gill, D.P. O'Neal, G. Stoica, and L.V. Wang. Photoacoustic tomography of a nanoshell contrast agent in the in vivo rat brain. *Nano Lett*, 4.

[149] M. Frenz and M. Jaeger. Optimization of tissue irradiation in optoacoustic imaging using a linear transducer: theory and experiments. *Proc. of SPIE*, 6856:68561Y/1–68561Y/13, 2008.

[150] J. Laufer, C. Elwell, D. Delpy, and P. Beard. In vitro measurements of absolute blood oxygen saturation using pulsed near-infrared photoacoustic spectroscopy: Accuracy and resolution. *Phys Med Biol*, 50.

[151] L. Song, C. Kim, K. Maslov, K.K. Shung, and L.V. Wang. High-speed dynamic 3d photoacoustic imaging of sentinel lymph node in a murine model using an ultrasound array. *Med Phys*, 36:3724–3729, 2009.

[152] K.H. Song, H.C. Kim, M.C. Cobley, N.Y. Xia, and L.V. Wang. Near-infrared gold nanocages as a new class of tracers for photoacoustic sentinel lymph node mapping on a rat model. *Nano Lett*, 9:183–188, 2009.